KARAGANDA
BUKETOV
UNIVERSITY

# EURASIAN PHYSICAL TECHNICAL JOURNAL

phtj.buketov.edu.kz

**Eurasian Physical Technical Journal, 2023, Vol. 20, No. 1(43)**

# CONTENTS

**Dear authors and readers!**

**Dear Colleagues!**

As usual, we inform you about the achievements of the peer-reviewed scientific journal Eurasian Physical Technical Journal, which is indexed in the Scopus database. The main page of the site provides information about the dynamics of the CiteScoreTracker indicator, which is gradually increasing. As of March 5, 2023, this indicator is 1.1 (https://phtj.buketov.edu.kz/index.php/EPTJ/index).

At the beginning of the year, a long-term plan for the development of the journal for the coming year was drawn up. All planned activities are aimed at strengthening the positions achieved and further expanding the prevalence of published materials in international databases. We will regularly inform you about all stages of implementation.

In the first issue of 2023, in the Materials Science section, readers are offered articles on the results of studying the properties of a wide variety of materials at the micro and nano levels. As a result of studies carried out on the basis of the Institute of Nuclear Physics (Almaty, Kazakhstan), an assessment was made of the influence of the processes of "formation of radiation damage in the form of point defects and their accumulation in the near-surface layer during irradiation with Xe22+ heavy ions on the change in the thermophysical properties of ceramics." Features of "phase and structural transformations in lithium-titanium ferrites depending on time, heating and cooling rates", as well as the temperature of liquid-phase sintering during thermal and radiation-thermal heating, were studied by Russian scientists from Tomsk.

Important practical results are presented in the joint work of Kazakh authors and a researcher from Kazan on the study of "the effect of molybdenum disulfide nanoparticles on the electron transport layer of zinc oxide of a polymer solar cell." Ukrainian researchers found that "boriding and boron cementation of the surface of steel 45 leads to the absence of adhesion with the surfaces of steels of some grades under certain conditions of normal pressure." It was also found that "with the transition to contact through a grease lubricant, there is an ambiguous nature of the manifestation of the rate of change of the piezoelectric coefficient." Authors from Eastern Kazakhstan presented the results of experiments on obtaining calcium-phosphate coatings on substrates made of titanium grade VT1-0 by plasma electrolytic oxidation. It has been shown that the addition of titanium oxide nanoparticles to the electrolyte can affect the structure, as well as the strength of the resulting coatings.

Articles from the Energy section are devoted to solving problems of the efficiency of thermal installations. For example, in a joint paper by authors from Kazakhstan, Russia, and Iraq, the effective efficiency of a dryer was considered using the effect in conjunction with the use of a heat flux source. The work of our university authors also studies the problems of analysis efficiency based on modeling the dynamics of heat and mass transfer processes under impulsive actions using the method of group consideration of arguments.

The first article in the Engineering section is devoted to predicting the heat-shielding and mechanical properties of composite materials based on porous fillers. On the basis of numerical calculations, the authors showed the feasibility of using multilayer composite materials based on porous fillers in load-bearing and enclosing structures of shell and plate types. The second article of the section considers an algorithm for approximating and searching for the maximum power generated on board a spacecraft for fast charging of secondary sources of electrical energy in cases of shading of solar panels or failure of photocells/elements.

The work of Almaty authors presents the results of studies aimed at studying the nature of cosmic rays, in particular, "Extensive Atmospheric Showers". Based on the results of studies of the biological protection of the high-flux research reactor PIK at the Kurchatov Institute, the authors propose a variant of modifying the protection of the hadron calorimeter to protect it from the influence of fast neutrons arising outside its working volume.

We hope that the presented research results will be of interest and will be useful for scientists, teachers, researchers, doctoral students and undergraduates.

Since 2023, Professor Svetlana Kushpil, Leading Researcher for the Heavy Ion Group, Institute of Nuclear Physics of the Czech Academy of Sciences, Rzhesh, Czech Republic, has been invited to work as a member of the editorial board of the Eurasian Physical Technical Journal. Professor Svetlana Kushpil is a graduate of the Joint Institute for Nuclear Research: Dubna, Russia. There she has almost 10 years of experience and Moscow State University, Moscow. Now she is leading researcher at the aforementioned large European research center. The significance of scientific research and the scientometric indicators of Professor S. Kushpil are impressive. According to the Scopus database she has Hirsch index 80. We hope that the work of professor Svetlana Kushpil will contribute to the expansion of scientific ties, which will undoubtedly improve the quality of published materials and a wider readership.

We will be glad to see you among our readers and authors of the next issues, where articles on topical and priority areas of modern physics and technology will be published.

Best wishes,
editor-in-chief, professor Sakipova S.E.
March 2023

# STUDY OF THE INFLUENCE OF RADIATION-INDUCED DAMAGE ACCUMULATION DURING THE INTERACTION OF HEAVY Xe$^{22+}$ IONS ON CHANGES IN THE THERMOPHYSICAL PARAMETERS OF ZIRCONIA CERAMICS

**Kozlovskiy A.L.**[1,2]

[1]Institute of Nuclear Physics, Almaty, Kazakhstan
[2]NPJSC L.N. Gumilyov Eurasian National University, Astana, Kazakhstan, kozlovskiy.a@inp.kz

*The aim of this paper is to evaluate the influence of the processes of radiation-induced damage formation in the form of point defects, dislocations and vacancies, as well as their accumulation and the formation of locally disordered regions in the near-surface layer of zirconia ceramics under irradiation with heavy Xe$^{22+}$ ions with an energy of 230 MeV, on the change in the thermophysical properties of ceramics. The choice of the ion type for irradiation is due to the possibilities of modeling radiation damage processes comparable to the impact of uranium nuclei fission fragments during nuclear reactions in nuclear fuel. The choice of materials for irradiation in the form of ZrO$_2$ ceramics is due to the prospects for their use as the main material for inert matrices of dispersed nuclear fuel for new generation reactors. This choice is due to the physicochemical, thermophysical and strength properties of ZrO$_2$ ceramics, which are more resistant than other types of oxide ceramics. During research, it was found that the formation of isolated locally heterogeneous regions at low irradiation fluences does not lead to significant changes in the thermophysical properties of the damaged ceramic layer. However, polymorphic transformations of the t-ZrO$_2$ → c-ZrO$_2$ type, which occur at irradiation fluences above $10^{12}$ ion/cm$^2$, lead to a decrease in thermal conductivity and the appearance of heat losses associated with the disruption of the phonon heat transfer mechanisms in the damaged layer.*

**Keywords:** zirconia ceramics, radiation defects, thermophysical properties, radiation damage, heavy ions, dispersed nuclear fuel

## Introduction

One of the important areas of research in modern materials science is the study of the resistance of ceramic materials to various types of radiation exposure [1-3]. Interest in this area of research consists in the need to expand the database, as well as gain new knowledge about the processes of formation, further interaction and accumulation of radiation damage in ceramics - one of the promising materials for nuclear energy. It should be noted that in ceramic materials, in contrast to metals and alloys, the processes of accumulation and further evolution of radiation damage have significant differences, as well as a pronounced relationship with the dielectric nature of ceramics [4,5]. These differences primarily consist in the processes of accumulation of radiation-induced damage and defects, which, due to the dielectric nature of ceramics, are limited in the damaged volume of the material and have low mobility. Such a difference in comparison with metals and alloys leads to the likelihood of the formation of so-called latent tracks or amorphous regions in some types of ceramics, and can also lead to the initialization of polymorphic or phase transformations [6-8]. These types of structural changes in the case of prolonged irradiation, and as a result, the accumulation of defects, can have a significant negative effect on the strength and thermal parameters. At the same time, if in the case of strength properties, small changes in the damaged volume can be ignored, since they have an insignificant effect on the stability of ceramics, then in the case of thermophysical parameters, everything is more serious. Any loss of thermal conductivity of materials must be taken into account, since a decrease in heat removal from the system will not allow all the generated heat to be removed, which can lead to the appearance of areas of local overheating of the reactor core. In the case of dispersed nuclear fuel, which is based on the technology of placing fissile material in an inert matrix based on ceramics, these effects are the most dangerous. The appearance of local areas of overheating in a dispersed fuel can lead to an acceleration of its destruction processes, which will lead to negative consequences, and for some types of oxide ceramics, the appearance of such areas can lead to an acceleration of structural disorder processes [9-11].

One of the promising materials in this direction is zirconium dioxide, the combination of properties of which makes it one of the promising materials for use as a basis for inert matrices of dispersed nuclear fuel. However, despite all the prospects, these ceramics have a number of disadvantages, primarily associated with the processes of polymorphic transformations, which can be initiated either as a result of mechanical impacts or during the accumulation of radiation damage [7,12-14]. In this regard, during evaluation of the applicability of these ceramics as materials for inert matrices of dispersed nuclear fuel, it is necessary to take into account the probability of occurrence of polymorphic transformation processes that can lead to a change in the properties of ceramics. Based on this, the main goal of this work is to study the effect of irradiation with heavy ions, and the processes of polymorphic transformations caused by them, on the change in the heat-conducting properties of ceramics, as well as to determine the dynamics of changes in the value of heat losses.

## 1. Experimental part

Polycrystalline two-phase ceramics based on zirconium dioxide ($ZrO_2$) with the dominant tetragonal phase of the P42/nmc(137) spatial syngony were chosen as the objects of study. The content of this phase is more than 80 %. The samples were irradiated at a DC – 60 heavy ion accelerator (Institute of Nuclear Physics, Astana, Kazakhstan). Heavy $Xe^{22+}$ ions with a total ion energy of 230 MeV (1.75 MeV/nucleon) were chosen as projectile ions. Irradiation was carried out at room temperature, which was maintained by placing the target on a special water-cooled target holder. Irradiation fluences were chosen from $10^{10}$ to $10^{15}$ ion/cm$^2$, while the range of $10^{11} – 10^{13}$ ion/cm$^2$ was performed with a small step to determine most accurately the stage of formation of overlapping regions of locally disordered regions in the structure of the damaged layer, the appearance of which has a significant effect on the processes of structural disorder and polymorphic transformations of the t-$ZrO_2 \rightarrow$ c-$ZrO_2$ type. The polymorphic transformation processes of the t-$ZrO_2 \rightarrow$ c- $ZrO_2$ type, accompanied by rearrangement of the crystal structure and displacement of the tetragonal phase with subsequent dominance of the cubic phase, according to the data of [7,13,14], occur in the fluence range of $10^{12}–10^{13}$ ion/cm$^2$ and are accompanied by structural changes.

To determine the thermophysical parameters, a standard method for measuring the longitudinal heat flux was used, which makes it possible to determine the change in the thermal conductivity coefficient and the amount of heat loss that occurs when the properties of the material subjected to irradiation change. For the measurement, a KIT-800 thermal conductivity device (Teplofon, Moscow, Russia) was used, which makes it possible to determine changes in the thermal conductivity coefficient in the range from 100 to 800°C. For measurements, samples were used before and after irradiation, with geometric dimensions of 8 x 8 mm and a thickness of 50 μm. Based on the measured values of the thermal conductivity coefficient, the value of heat losses was calculated, reflecting changes in thermophysical parameters in samples subjected to irradiation.

## 2. Results and discussion

As shown in several works [7,12-14], irradiation of ceramics with irradiation fluences above $10^{12} – 10^{13}$ ion/cm$^2$ with heavy $ZrO_2$ ions leads to the initialization of polymorphic transformations of the t-$ZrO_2 \rightarrow$ c-$ZrO_2$ type, which consist in a change in the phase composition and subsequent deformation of the crystal lattice, as well as the accumulation of radiation-induced damage. In this case, as is known, the polymorphic transformation processes are associated with a destructive change in volume as a result of the transformation of a tetragonal structure into a cubic one, accompanied by a change in volume and density. A change in density during the action of deformation distortions leads to the appearance of porous inclusions, which have a negative impact not only on the structural properties, but also on the thermophysical parameters. So, for example, as was shown in [15], the change in the thermophysical properties of ceramics is greatly influenced by the grain size and porosity, which can change both under varying conditions and the choice of the method for obtaining ceramics, and in the case of external influences. At the same time, the occurrence of heterogeneities in the composition of ceramics also plays a very important role in the change in thermal conductivity, as well as the occurrence of heat losses in ceramics [15].

According to the assessment of the phase composition of $ZrO_2$ ceramics in the initial state, these ceramics are a mixture of two phases: the dominant tetragonal $ZrO_2$ phase with the P42/nmc(137) spatial system and the cubic $ZrO_2$ phase with the Fm-3m(225) spatial system. The ratio of tetragonal (t-$ZrO_2$) and cubic (c-$ZrO_2$) phases is close to 4:1 (80%:20%). At the same time, the structural ordering degree in the

initial state of ceramics is more than 97 %, which indicates a low content of amorphous or disordered inclusions, the presence of which is due to the ceramics manufacturing technology.

According to the data on changes in the phase composition depending on the irradiation fluence, the following was established. In the range of irradiation fluences of $10^{10} – 10^{12}$ ion/cm$^2$, no changes in the ratio of the t-ZrO$_2$ and c-ZrO$_2$ phases were observed, which indicates that the polymorphic transformation processes do not occur at these fluences. This absence of polymorphic transformations in this range of irradiation fluences can be explained as follows. At irradiation fluences below $10^{12}$ ion/cm$^2$, the interaction of incident ions with the ceramic structure occurs in local isolated regions along the ion motion trajectory in the material. Moreover, the diameter of these areas, according to the calculated estimates, is no more than 5 – 10 nm, which, at low irradiation fluences, indicates a low probability of the formation of overlapping of these damaged areas from two incident ions or the hit of two ions in one place sequentially. In this case, structural changes occur in locally isolated regions, and the accumulation of defective inclusions occurs very slowly in view of the fact that most of the defects formed in these regions annihilate among themselves in very short time intervals. During analysis of the structural changes and swelling of the crystal lattice volume depending on the irradiation fluence presented in Figure 1, it can be seen that at given irradiation fluences ($10^{10} – 10^{12}$ ion/cm$^2$), the main changes occur when the fluence increases above $5 \times 10^{11}$ ion/cm$^2$, for which the probability of overlapping local defective regions approaches 1, and the average distance between isolated regions becomes less than 50 – 100 nm.
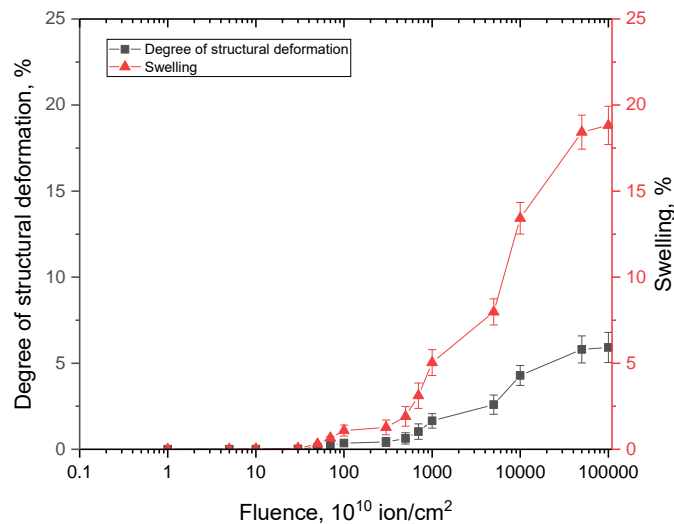


**Fig.1.** Results of deformation contributions in the damaged layer in ZrO$_2$ ceramics under heavy ion irradiation

As can be seen from the data presented, the main changes in the crystal structure deformation occur at fluences above $10^{12}$ ion/cm$^2$, for which, according to the phase analysis, the initialization of the polymorphic transformation processes of the t-ZrO$_2$ → c-ZrO$_2$ type is observed, which ends with the complete displacement of the tetragonal phase and the dominance of the cubic phase. At the same time, according to the assessment of deformation contributions, polymorphic transformations of t-ZrO$_2$ → c-ZrO$_2$ lead to a sharp increase in volumetric swelling, which is due to destructive changes associated with phase transformations. It should also be noted that at fluences above $10^{14}$ ion/cm$^2$, there is a noticeable decrease in the rate of swelling and destructive deformation of the crystal structure in the damaged layer, which may be due to the effects of saturation of the damaged layer with defects at high irradiation fluences.

As is known, deformation distortions and changes in the crystal lattice volume led to a change in the density and an increase in the porosity of ceramics. At the same time, according to the data presented in Figure 1, the processes of polymorphic transformations lead to a sharp increase in volumetric swelling associated with destructive distortion of the crystal lattice during the transformation of the tetragonal phase into a cubic one. Figure 2 shows the dependences of changes in the density and porosity of ceramics, calculated on the basis of volumetric changes in the crystal lattice with increasing fluence. The general view of the presented results in Figure 2 characterizes the change in the damaged layer associated with its deformation, change in density and the formation of porous inclusions. At the same time, according to the

data presented, the main changes in density and, as a consequence, the formation of porous inclusions, occur during the initialization of the polymorphic transformation processes, accompanied by the transformation of the tetragonal phase into a cubic one, followed by a destructive increase in the crystal lattice volume. At the same time, it should be noted that at high irradiation fluences of $10^{13} - 10^{14}$ ions/cm$^2$, a decrease in changes in density destruction is observed, which indicates the effect of accumulation of radiation distortions and their influence on structural changes, which was also noted when interpreting the data on changes in deformation contributions.

A change in the density and porosity of ceramics, as well as its deformation, should affect the change in thermophysical parameters, the change of which is very important in assessing the applicability of these ceramics as structural materials for the nuclear industry. At the same time, volumetric changes in the damaged layer can have a different effect on the mechanism of heat transfer, since, unlike metals, for dielectric ceramics, the main mechanisms of heat transfer are phonon mechanisms. Figure 3 shows the dependence of the change in the thermal conductivity coefficient ($K_{eff}$) on the irradiation fluence, which characterizes the change in the thermophysical properties of ceramics exposed to irradiation with heavy ions.
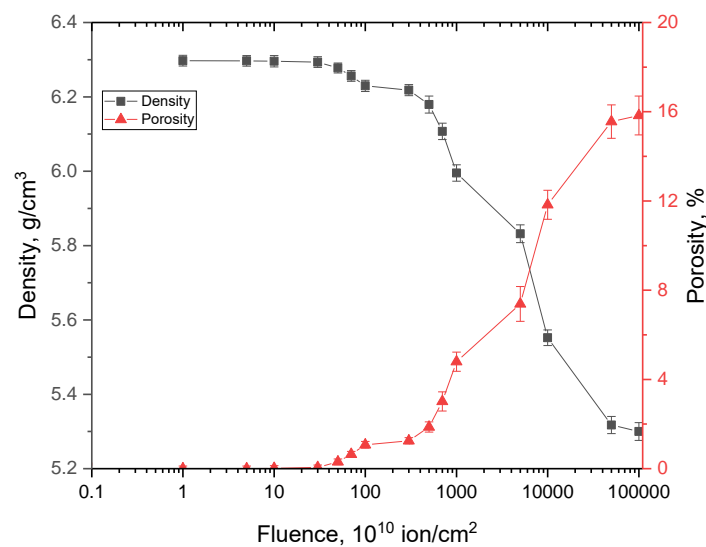


**Fig.2.** Results of changes in the density and porosity of ZrO$_2$ ceramics depending on the irradiation fluence
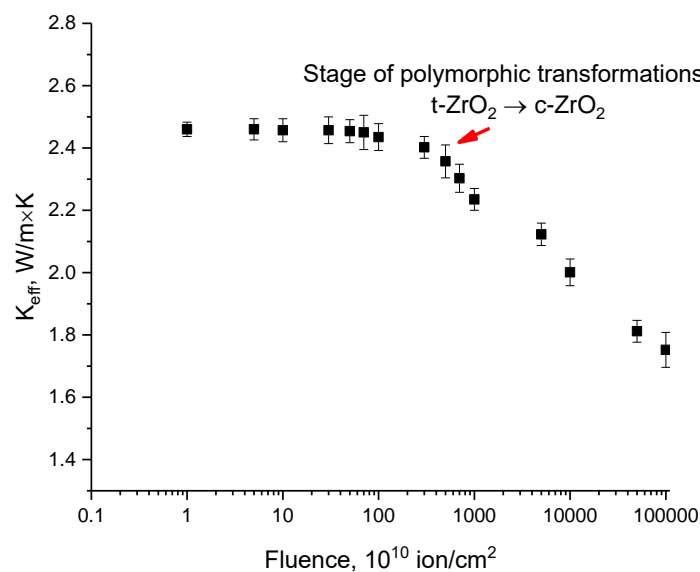


**Fig.3.** Results of the change in the thermal conductivity coefficient from the irradiation fluence

The general view of the presented changes in the thermal conductivity coefficient has several distinct areas that depend on the irradiation fluence and structural changes associated with the accumulation of radiation damage. At low irradiation fluences (below $10^{12}$ ion/cm$^2$), practically no changes in $K_{eff}$ are observed, which indicates that structural distortions resulting from the formation of locally isolated regions of structural damage along the ion trajectory in the surface layer do not affect the heat transfer mechanisms associated with phonon heat transfer. At the same time, an increase in deformation distortions at fluences above $5 \times 10^{11}$ ion/cm$^2$ leads to a slight decrease in the thermal conductivity coefficient, fitting into the measurement error, which indicates that deformation distortions resulting from the occurrence of areas of overlap of local defective fractions create obstacles to heat transfer in the form of highly disordered inclusions.

The polymorphic transformation processes of the t-ZrO$_2$ → c-ZrO$_2$ type, which occur at fluences above $10^{12}$ ion/cm$^2$, lead to a sharp drop in thermal conductivity, which indicates a change in the heat transfer mechanisms, as well as a decrease in thermophysical parameters. A further increase in the irradiation fluence, which leads to a destructive change in the volume of the crystal lattice and the density of ceramics, leads to a decrease in thermal conductivity, as well as an increase in heat losses. Figure 4 shows dependences of the change in the value of heat losses on the porosity of ceramics, which increases as a result of polymorphic transformations and destructive changes in structural parameters.
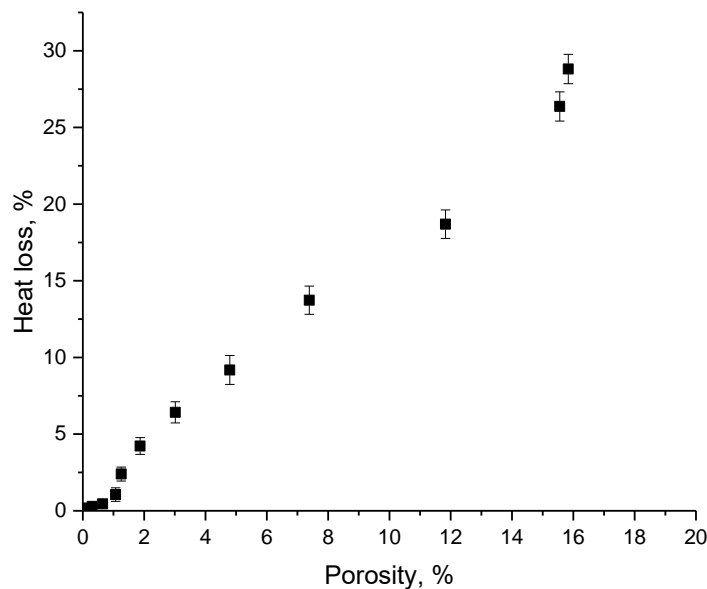


**Fig.4.** Results of a comparative analysis of changes in the value of heat losses from the porosity of ceramics subjected to irradiation

As can be seen from the data presented, an increase in the porosity of ceramics above 2% leads to an increase in heat losses, while the change in the value of heat losses due to porosity is not linear and has a pronounced increase at maximum irradiation fluences. Such a change in the value of heat losses at maximum irradiation fluences ($5 \times 10^{13} - 10^{14}$ ion/cm$^2$) can be due to the fact that, at these fluences, highly defective regions with a highly disordered structure and amorphous-like inclusions are formed, the appearance of which has a negative effect on the heat transfer mechanisms. Figure 5 shows the dependences of the change in the thermal conductivity and thermal diffusivity on the density of ceramics, which changes as a result of the damaged layer destruction.

As can be seen from the data presented, a decrease in the density of ceramics associated with processes of destructive volume change, as well as processes of polymorphic transformations, leads to a loss of thermal conductivity and a decrease in thermal diffusivity, which affects the thermophysical properties of ceramics. At the same time, the maximum decrease in values is more than 25 % of the initial value, which indicates the destructive effect radiation exposure on the mechanisms of heat transfer and heat transfer.
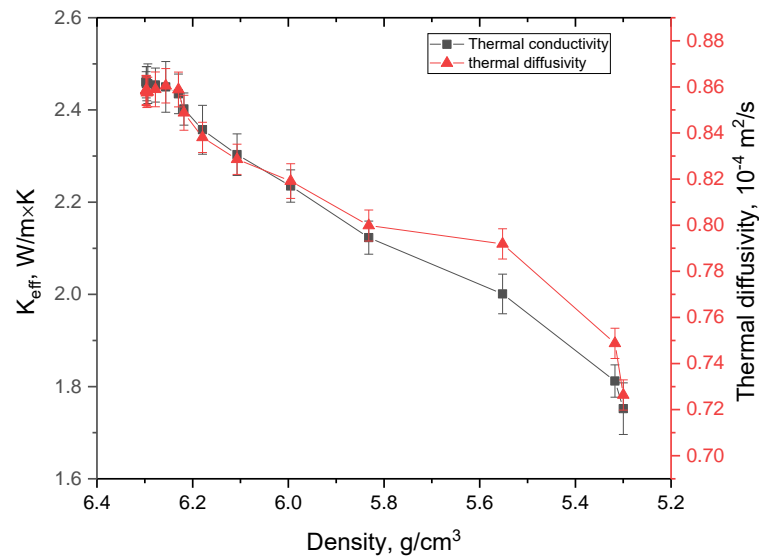
**Fig.5.** Dependence of changes in thermophysical parameters on the density of ceramics

## Conclusion

The paper presents the results of estimating the change in thermophysical parameters in $ZrO_2$ ceramics subjected to irradiation with heavy $Xe^{22+}$ ions in the range of irradiation fluences corresponding to the formation of single local defect regions and the overlapping of locally heterogeneous regions causing polymorphic transformation processes of the $t\text{-}ZrO_2 \rightarrow c\text{-}ZrO_2$ type. During the studies, it was found that the main contribution to the structural disorder of the damaged layer of ceramics at fluences above $10^{12}$ ion/cm$^2$ is made by volumetric swelling associated with a destructive change in the structure during polymorphic transformations. According to the assessment of changes in thermophysical parameters, it was found that the main changes associated with an increase in heat losses occur during the initialization of polymorphic transformation processes. At the same time, deformation processes at low irradiation fluences do not have a significant effect on the decrease in thermal conductivity. An analysis of the change in thermophysical parameters depending on the change in structural properties and porosity showed that the main contribution to the decrease in thermal conductivity and thermal diffusivity is made by a decrease in the density of ceramics, and the associated change in porosity.

## REFERENCES

1 Liu Y., et al. Irradiation response of $Al_2O_3$-$ZrO_2$ ceramic composite under He ion irradiation. *Journal of the European Ceramic Society*. 2021, Vol. 41, No.4, pp. 2883 – 2891. doi:10.1016/j.jeurceramsoc.2020.11.042

2 Shukla P.P., Lawrence J. Characterization and compositional study of a $ZrO_2$ engineering ceramic irradiated with a fibre laser beam. *Optics & Laser Technology*. 2011, Vol. 43, No.7, pp. 1292 – 1300. doi:10.1016/j.optlastec.2011.03.026

3 Liu J., et al. In-situ TEM study of irradiation-induced damage mechanisms in monoclinic-$ZrO_2$. *Acta Materialia*. 2020, Vol. 199, pp. 429 – 442. doi:10.1016/j.actamat.2020.08.064

4 Khrustov V.R., et al. Behavior of ceramics based on $Al_2O_3$ and $ZrO_2$ nanopowders under gamma-ray irradiation. *Inorganic Materials: Applied Research*. 2014, Vol. 5, No.5, pp. 482 – 487. doi:10.1134/S2075113314050098

5 Wang Z.G., et al. Enhanced nucleation undercooling and surface self-nanocrystallization of $Al_2O_3$-$ZrO_2$ ($Y_2O_3$) eutectic ceramics. *Journal of the European Ceramic Society*. 2019, Vol. 39, No. 4.       P. 1707-1711. doi:10.1016/j.jeurceramsoc.2018.12.011

6 Yang M., et al. Ablation behavior of SiC whisker and ZrB2 particle-filled ZrO2 sol-gel composite coating under high-intensity continuous laser irradiation.   *Ceramics International*. 2021, Vol. 47, No.18, pp. 26327-26334. doi:10.1016/j.ceramint.2021.06.043

7 Ghyngazov S.A., et al. Swift heavy ion induced phase transformations in partially stabilized ZrO2. *Radiation Physics and Chemistry*. 2022, Vol. 192, pp. 109917. doi:10.1016/j.radphyschem.2021.109917

8 Van Vuuren A.J., et al. Microstructural effects of Al doping on $Si_3N_4$ irradiated with swift heavy ions. *Acta Phys. Pol. A*. 2019, Vol. 136, pp. 241 – 244. doi:10.12693/APhysPolA.136.241

9 Costantini J.M. et al. Raman spectroscopy study of damage in swift heavy ion-irradiated ceramics. *Journal of Raman Spectroscopy*. 2022, Vol. 53, No.9, pp. 1614 - 1624. doi:10.1002/jrs.6414

10 Chauhan V., Kumar R. Phase transformation and modifications in high-k ZrO2 nanocrystalline thin films by low energy Kr5+ ion beam irradiation. *Materials Chemistry and Physics*. 2020, Vol. 240, pp. 122127. doi:10.1016/j.matchemphys.2019.122127

11 Ciszak C., et al. Raman spectra analysis of ZrO2 thermally grown on Zircaloy substrates irradiated with heavy ion: Effects of oxygen isotopic substitution. *Journal of Raman Spectroscopy*. 2019, Vol. 50, No.3, pp. 425 – 435. doi:10.1002/jrs.5513

12 Ghyngazov S., et al. Surface modification of ZrO2-3Y2O3 ceramics with continuous Ar+ ion beams. *Surface and Coatings Technology*. 2020, Vol. 388, pp. 125598. doi:10.1016/j.surfcoat.2020.125598

13 Alin M., et al. Comprehensive study of changes in the optical, structural and strength properties of ZrO2 ceramics as a result of phase transformations caused by irradiation with heavy ions . *Journal of Materials Science: Materials in Electronics*. 2021, Vol. 32, No.13, pp. 17810 – 17821. doi:10.1007/s10854-021-06317-3

14 Alin M., et al. Study of the mechanisms of the t-ZrO2→ c-ZrO2 type polymorphic transformations in ceramics as a result of irradiation with heavy Xe22+ ions. *Solid State Sciences*. 2022, Vol. 123, pp. 106791. doi:10.1016/j.solidstatesciences.2021.106791

15 Deng Z.Y., et al. Microstructure and thermal conductivity of porous ZrO2 ceramics. *Acta materialia*. 2007, Vol. 55, No. 11, pp. 3663 – 3669. doi:10.1016/j.actamat.2007.02.014

.

# STUDY OF THE INITIAL MAGNETIC PERMEABILITY OF LiTiZnMn FERRITES OBTAINED BY LIQUID-PHASE SINTERING UNDER RADIATION-THERMAL AND THERMAL CONDITIONS

**Surzhikov A.P., Lysenko E.N., Malyshev A.V.**

Tomsk Polytechnic University, Tomsk, Russia, malyshev@tpu.ru

*The measuring the temperature dependence of the initial permeability was used to study the features of phase and structural transformations in lithium-titanium ferrites as a function of time, heating and cooling rates, and the temperature of liquid-phase sintering under thermal and radiation-thermal heating. Ferrite was synthesized from powder mixture by solid-phase synthesis. A low-melting additive bismuth dioxide was used to obtain the ferrite ceramics by liquid-phase sintering. RT sintering was carried out by heating the samples with a pulsed (1.5–2.0) MeV electron beam. It was established that the additive leads to a less defective state of sintered ferrites, while the action of radiation enhances this effect in the early stages of sintering. The regularities of the influence of the heating and cooling rates of compacted samples on the change in the initial magnetic permeability of sintered ferrites are established.*

**Keywords:** lithium ferrite, liquid-phase sintering, electron beam, high temperature, heating and cooling rates, initial magnetic permeability.

### Introduction

The fundamental requirements for ferrite materials production are their good electromagnetic characteristics, which depend on the chemical composition of the reagents and ferrite technology. The main operation of the ferrites production by ceramics technology is the extremely long sintering of compacted samples molded from synthesized powders.

The operations used to activate the sintering of ferrites, including the two-stage introduction of various components, the addition of ferrite powders of the same composition to the samples, the presence of a liquid phase, forced sintering, the application of ultrasound to the sintering process [1–4], are accompanied by an increased probability of impurity phases entering the product composition, worsening the chemical and structural homogeneity of the material and, accordingly, the electromagnetic properties. At the same time, it is not always possible to reduce the content of impurity phases by selecting the sintering temperature regime, especially in the case of thermally unstable compounds, such as lithium ferrispinels.

In recent years, the impact of ionizing radiation fluxes has been developed in the production and modification of materials. In this case, the fundamental phenomenon of a multiple increase in the process of synthesis of multicomponent powder materials [5–13] and sintering [14–24] under radiation-thermal (RT) conditions was discovered. The processes of lithium-titanium ferrites sintering have been most fully studied under such specific conditions of the combined action of high temperatures and intense electron flows [25–29]. Here, the regularities in compaction of ferrites have been established and a multiple increase in the rate of lithium-titanium ferrites sintering has been shown in [30, 31].

The ultimate goal of any technology for the ferrites production is to achieve a given level of operational properties, including the main functional magnetic characteristics. Therefore, the influence of various factors on the formation of the ferrites magnetic characteristics under RT sintering is of particular interest.

From this point of view, data on phase transformations in ferrites during RT sintering are important. In the case of obtaining lithium ferrites, the complexity of the X-ray phase analysis is due to the overlap of the main reflections from the $LiFe_5O_8$, $LiFeO_2$, $Fe_3O_4$ phases, which can form during synthesis or sintering. Therefore, the method of measuring the temperature dependence of the initial permeability is promising for studying the features of phase transformations in lithium ferrite ceramics.

For this purpose, in [32], the radiation contribution to the ferrite electromagnetic parameters formation was established from a comparison of the temperature dependences of the initial permeability ($\mu_i$) of lithium

ferrites obtained by RT and thermal (T) solid-phase sintering. Since the technology of liquid-phase sintering is widely used in ferrites production, the next stage of our work is to study the same patterns in the presence of a liquid-phase component in ferrites under the same RT and T conditions. In addition, in order to establish the effects of low-melting additive, the obtained data on liquid-phase sintering of lithium ferrites were compared with the data obtained during solid-phase sintering. Since, before the pressing stage, a solution of polyvinyl alcohol (PVA) and a low-melting additive of bismuth oxide ($Bi_2O_3$) were introduced into the composition of ferrite powders, the influence of cooling and heating modes of ferrites during sintering on the temperature dependence of $\mu_i$ of samples was studied.

## 1. Experimental part

### 1.1 Materials

In this work, experimental samples of lithium-titanium ferrite were prepared according to the following proven technological stages. Ferrites are synthesized from a mechanical mixture of oxides and carbonates containing (in wt %): $Fe_2O_3$ – 59.8; $Li_2CO_3$ – 11.2; $TiO_2$ – 18.7; ZnO – 7.6; $MnCO_3$ – 2.7. After weighing the above components, they were ground together and wet mixed by a vibrating mill for 1 hour using distilled water, which was added to the powder in a weight ratio of 1:2. The milled mixture was dried at 80 °C for 24 h and then passed through a 0.7 sieve. The distilled water was introduced into the resulting powder in an amount of 10 wt% of the powder, and it was briquetted. The briquettes were heated in thermal furnaces at a rate of 200 °C/h to 900 °C, kept at this temperature for 6 hours, and cooled to room temperature. After that, they were crushed, sieved through a 0.9 sieve and mixed by a vibrating mill for 45 min. A low-melting additive in the form of a suspension based on $Bi_2O_3$ (0.22 wt %) dissolved in concentrated nitric acid was added to the powder and homogenized by milling in a ball mill for 4 h. Then, a 10% solution of polyvinyl alcohol (PVA) was added to the synthesized ferrite in an amount of 12 wt. % of the ferrite powder, and the thus prepared powder was alternately rubbed through 0.7 and 0.45 sieves. Press samples were made by cold one-sided pressing in the toroidal form with an outer diameter of 18 mm, an inner diameter of 14 mm, and a height of 2 mm. The pressing pressure is selected, as a rule, experimentally for each specific ferrite composition according to the established dependence of the bulk density $\rho$ of the samples on the pressing pressure. In this work, a pressing pressure of 130 MPa and a holding time of the samples under this pressure of 1 min were used.

### 1.2 Characterization techniques

RT-sintering was carried out by heating the samples with a pulsed (1.5–2.0) MeV electron beam using an ILU-6 accelerator. The beam current in the pulse was (0.5–0.9) A, the duration of the irradiation pulse was 500 µs, the pulse repetition rate was (5–50) Hz, and the heating rate of the samples was 1000 °C/min. The samples were placed in a cell, which was a box made of lightweight chamotte with a bottom wall thickness of 15 mm. From the side of the electron beam, the cell was covered with a radiation-transparent protector with a mass thickness of 0.1 g/cm. The temperature was measured using a thermocouple located in a control sample that was placed in close proximity to the sintered ferrite samples.

Thermal sintering of the samples was carried out using a chamber electric furnace. For this, the samples were placed in a preheated furnace, which ensured a heating rate comparable to that of an electron beam. The cell design and temperature control technique are similar to those used in RT sintering. Both modes of sintering were carried out in air. Based on the analysis of literature data on methods for measuring the initial magnetic permeability ($\mu_i$), a method based on measuring the inductance of ring cores in an alternating magnetic field was used [33]. On samples sintered in different modes, a single-layer winding was evenly distributed around the perimeter of the core. The measurement of $\mu_i$ was carried out using a standard inductance meter at a frequency of 1 MHz when the sample cooled down from a temperature obviously higher than the Curie temperature (about 350 °C). From the temperature dependence of the inductance, the temperature dependence of $\mu_i$ was determined by the equation [32, 33].

## 2. Results and discussion

Figure 1 shows the temperature dependences of $\mu_i$ for the samples sintered at 1373 K under thermal and radiation-thermal conditions. Qualitatively, these dependences are identical to similar ones for solid-phase sintered (that is, without $Bi_2O_3$) samples presented in [32], since they are based on the same magnetization

processes. It can be seen from Fig. 1 that the values of $\mu_i$ at the maxima of the curves exceed the corresponding values of $\mu_i$ in the samples sintered without the addition of $Bi_2O_3$. This is especially evident during sintering in the T mode, as well as in the early stages of sintering in the RT mode.
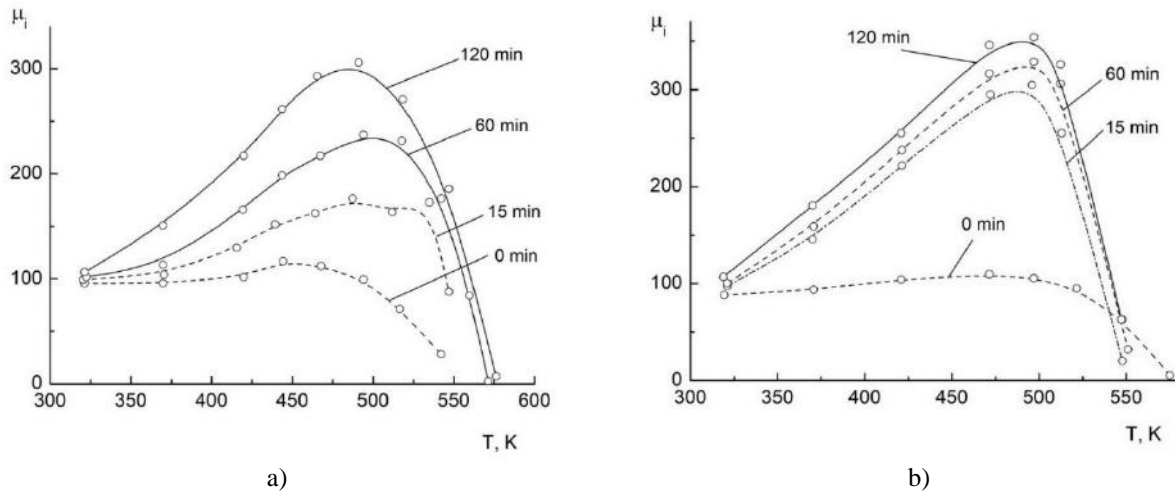


**Fig.1.** Temperature dependence of initial permeability of the ferrite samples sintered at 1373 K
for different times by T (a) and RT (b) method

The dependences of the maximum value (from the temperature dependence) of the initial permeability, $\mu_{i\,max}$, of ferrite on the duration of sintering are shown in Figure 2. When sintering in the RT mode, the rate of increase in $\mu_{i\,max}$ at the beginning of sintering significantly exceeds the growth rate $\mu_{i\,max}$ for samples sintered in the T mode. When the sintering time is more than 20 min, the growth rates $\mu_{i\,max}$ are equalized for both types of sintering. Since the value of $\mu_{i\,max}$ is inversely proportional to the integral defectiveness of ferrite samples, it can be concluded that the sintering of samples with the addition of $Bi_2O_3$ leads to a more defect-free state in ferrite. In this case, the action of radiation at RT heating enhances this effect in the early stages of sintering.
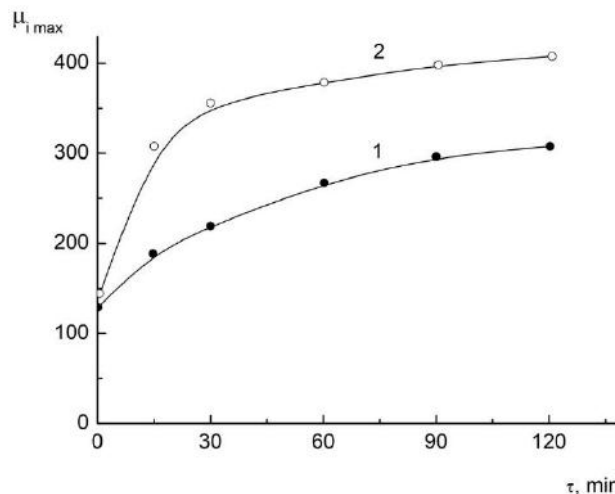


**Fig.2.** Dependence of the maximum value of the initial permeability of ferrite (from the temperature dependence) on the duration of sintering at 1373 K via T (curve 1) и RT (curve 2) modes

Considering that the early stages of liquid-phase sintering are caused by such processes as the dissolution of a solid in the contact zone, the dissolution of protrusions and irregularities of particles, and the rearrangement of particles [34], it should be assumed that under radiation heating, these processes are intensified. This conclusion is consistent with the results obtained from the study of the kinetics of liquid-phase compaction of powder materials under the action of an electron beam and presented in [35].

Figure 3 shows the differential temperature dependences of $\mu_i$ near the Curie temperature for samples containing $Bi_2O_3$. These samples contain two magnetic phases, which correspond to the maxima of the decay

rate $d\mu_i/dT$ at temperatures of 537 K and 548 K. In the early stages of sintering (up to 15 min), the low-temperature magnetic phase dominates in the T mode, and the high-temperature one dominates in the RT mode. At a sintering time of $\tau = 30$ min, the phase ratio is equalized for both sintering modes, and at $\tau \geq 60$ min, the high-temperature phase predominates regardless of the mode.
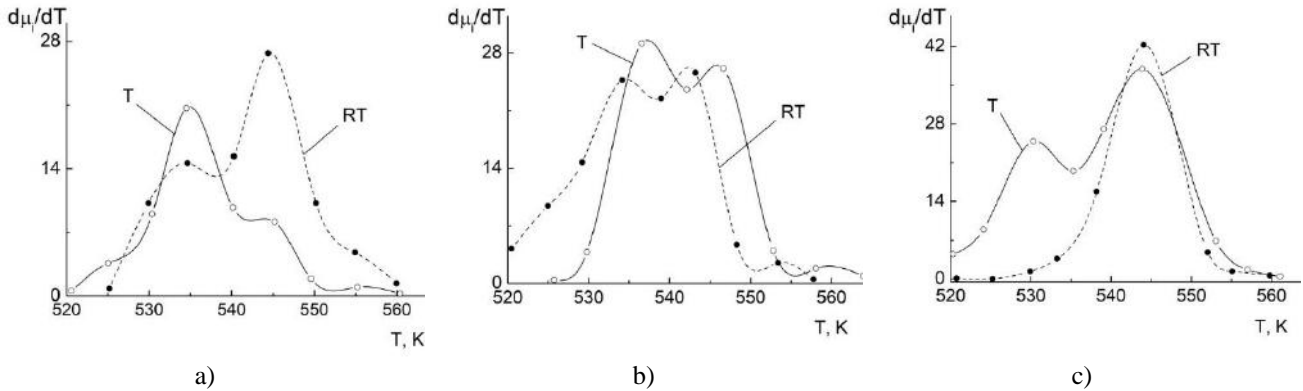


**Fig.3.** Differential temperature dependence of the initial permeability near the Curie temperature for samples sintered at 1373 K for 15 (a), 30 (b) and 60 (c) min via T and RT modes

From these results, the peculiarity of homogenization of LiTiZnMn ferrite in the presence of $Bi_2O_3$ is concluded: the rate of chemical homogenization is higher compared to RT homogenization, and at $\tau > 60$ min, the phase compositions are equalized. At the nonisothermal stage of sintering and in the isothermal mode up to $\tau \sim 15$ min, the rate of RT homogenization remains high. To increase the sintering rate and intensify phase transformations in ceramic technology, elevated firing temperatures are used. But, as noted above, this method is not suitable for lithium ferrites because of their low thermal stability. In order to verify this position, the temperature dependences of $\mu_i$ and $d\mu_i/dT$ were measured for the samples sintered at a temperature of 1473 K. Figure 4 and Figure 5 show these dependencies.
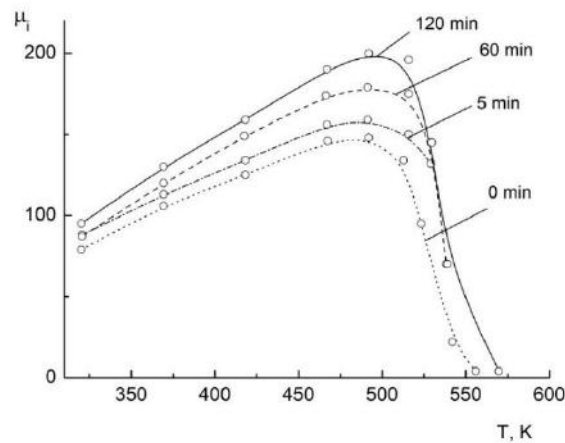


**Fig.4.** Temperature dependence of the initial permeability of the ferrite sintered at 1473 K for different sintering times

It is clearly recorded that the temperature dependences of $\mu_i$ become flatter, with poorly pronounced temperature maxima. In addition, the maximum values of $\mu_{i\,max}$ sharply decrease in comparison with the curves in Fig. 3. In this case, the degree of relative decrease in $\mu_{i\,max}$ increases with increasing duration of isothermal sintering. This behavior of the curves indicates an increased defectiveness of the samples sintered at 1473 K and competing processes of healing microstructure defects (pores, phase inclusions, etc.) as well as the formation of new defects due to the decomposition of ferrite. That is, as sintering progresses, the resulting defectiveness decreases (since $\mu_{i\,max}$ increases), but due to deferritization, the rate of its decrease is reduced, despite the higher temperature. At the beginning of isothermal exposure, when the degree of decomposition is low, and the rate of void healing is high, there is a sharp decrease in the total defectiveness and, accordingly, a sharp increase in $\mu_{i\,max}$ to a level characteristic of sintering at 1373 K.

Simultaneously with these processes, homogenization of the magnetic phases occurs. It can be seen from Figure 5 that by the beginning of the isothermal stage of sintering, two phases are present in the sample. Then the transition width narrows ($\tau \sim$ 5 min) and after 15 min only the high-temperature phase remains, which remains until the limiting ($\tau$ = 120 min) sintering time. Considering that phase homogenization is associated with diffusion transitions of atoms, the observed increase in the rate of this process with increasing temperature should be recognized as natural. A feature of the crystal chemistry of lithium-containing ferrites is the ordered arrangement of $Li^+$ and $Fe^{3+}$ ions in octahedral positions in the (110) direction. Upon slow cooling to a temperature of 750 °C, the structure is ordered. Such a state of ferrite is characterized by a lattice parameter $a$ = 8.329 Å (in disordered ferrite $a$ = 8.332 Å).
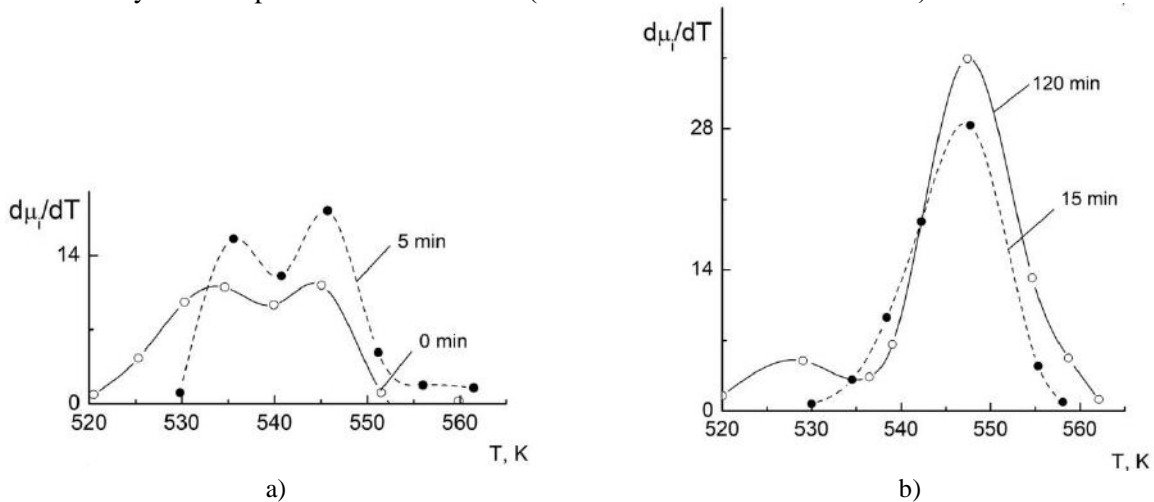


**Fig.5.** Differential temperature dependence of the initial permeability near the Curie temperature for samples sintered at 1373 K for 0, 5 min (a) and 15, 120 min (b) via T mode

It has been established that the magnetic anisotropy constant $k$ of "disordered" ferrite exceeds in absolute value $k$ "ordered" ferrite. The ordering of the ferrite structure also reduces the magnetostriction constant $\lambda_S$, but does not affect the saturation magnetization $M_S$ (since the cation distribution does not change in this case). By adjusting the cooling mode of sintered ferrite, one can influence the magnetic permeability of products. In this regard, the relationship between the cooling conditions of the samples and their initial magnetic permeability was studied.

Methodically, the cooling temperature range was divided into two parts: the first part included temperatures from 1370 K (sintering temperature) to 1030 K (cationic freezing temperature); the second is from 1030 K to 530 K (the lower limit of temperature control). Changing the duration of cooling in the first section created different degrees of cationic ordering. At such high temperatures, the samples are quite plastic, and there is no accumulation of thermoelastic stresses (at high cooling rates). And vice versa, when the cooling rate changes only in the second section, the degree of cationic ordering remains constant. The value of thermoelastic stresses can change, since the plasticity of the material at low temperatures is low.

Figure 6a shows the temperature dependences of $\mu_i$ at different cooling rates in the high-temperature section. It can be seen that with a decrease in the cooling rate, $\mu_i$ monotonically increases, which indicates the importance of the relationship between the cationic ordering and the value of $\mu_{i\,max}$ as well as a slight change in the stoichiometry of the composition at the cooling stage. In contrast to high-temperature cooling, low-temperature variations in the rate of temperature decrease do not lead to noticeable changes in the values of $\mu_i$. As follows from Figure 6b, changes in the cooling rate within 4.1–125 K/min in the temperature range 1030–530 K do not lead to a difference in the temperature dependences of $\mu_i$. Probably, the quenching stresses arising during thermal cooling are insignificant in comparison with the elastic fields created by the coalescence of grains with different crystallographic orientations, as well as various kinds of inclusions in the grain material.

The direct dependences of $\mu_{i\,max}$ on the cooling rate are shown in Figure 7. The specificity of radiation heating of sintered products lies, as is known, in the volumetric nature of heat release. The question arises: do the processes of removal of the technological binder (PVA) and spreading of the liquid phase ($Bi_2O_3$) over the array of grains of the resulting ferrite have time to complete in a short heating time (~2.5 min). The incompleteness of these processes leads to a deterioration in the quality of products.

The temperature dependences of $\mu_i$ were studied both on the rate of heating of press samples during their sintering and on the isothermal exposures during their heating. For this, the isothermal sintering was carried out at 1373 K for 60 min.



a)                                                                                      b)
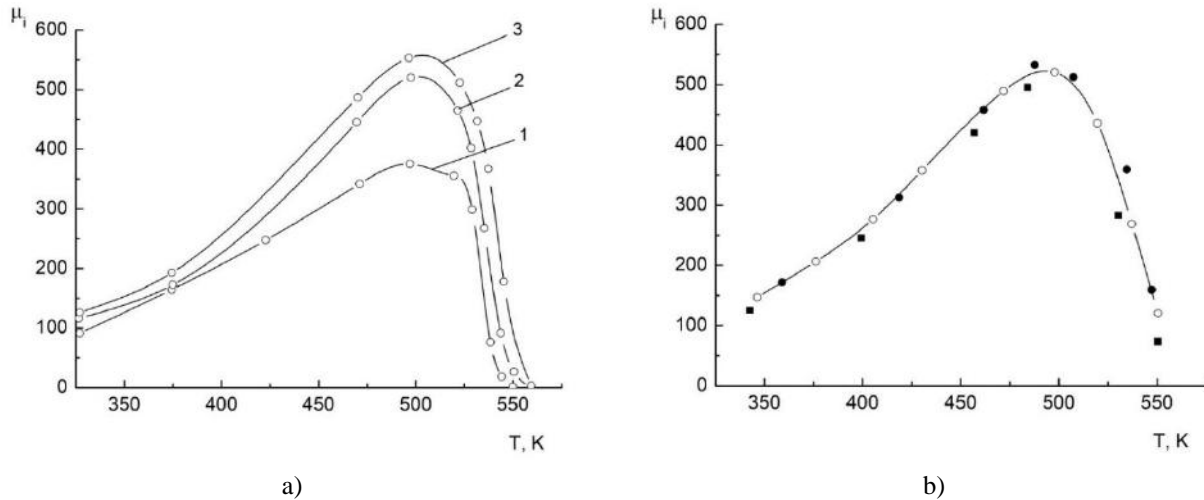
**Fig.6.** Temperature dependence of the initial permeability of ferrite with $Bi_2O_3$ sintered *via* RT mode at 1373 K for 2 h: (a) − high-temperature cooling during sintering at rates of 68 K/min (curve 1); 5.7 K/min (curve 2); 2.8 K/min (curve 3); (b) −low-temperature cooling at a rate of 4.1 K/min (•); 2.5 K/min (o); 125 K/min (■)
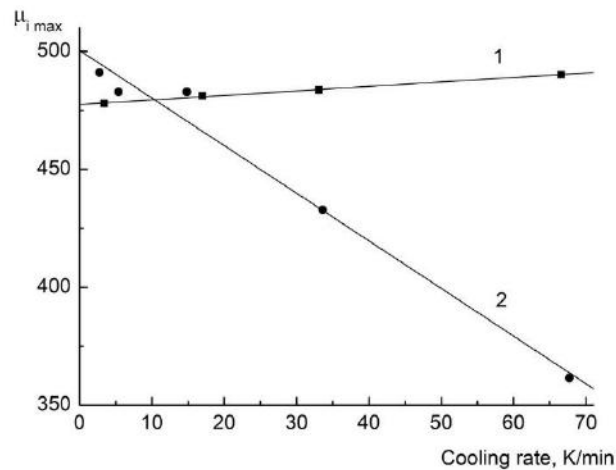


**Fig.7.** Dependence of $\mu_{i\,max}$ on the cooling rate: high-temperature cooling section (curve 1); low-temperature cooling section (curve 2)

The cooling rate was constant and amounted to 25 K/min. The results of $\mu_{i\,max}$ measurements (Fig. 8) indicate that a change in the rate of radiative heating by two orders of magnitude of pressed samples does not cause changes in the value of $\mu_{i\,max}$.
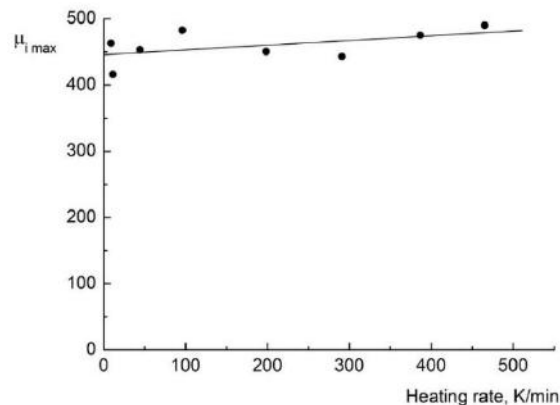
**Fig.8.** Dependence of $\mu_{i\,max}$ on the radiative heating rate of pressed samples up to a sintering temperature of 1373 K

In addition, isothermal exposures were carried out at characteristic points at the PVA removal temperature (673 K) and at the melting point of the $Bi_2O_3$ additive (1093 K). The exposure time was varied within 10–60 min, the sample heating rate between the characteristic temperatures was 450 K/min. The results showed that the presence of isothermal exposures does not affect the nature of the temperature dependence of $\mu_i$ and the value of $\mu_{i\,max}$.

## Conclusion

The scientific significance of the results is determined by the data on the initial magnetic permeability, as well as the relationship of this characteristic with phase changes in ferrite sintered under conditions of electron beam heating. It was shown that the presence of a low-melting additive $Bi_2O_3$ leads to a more defect-free state of the ferrite. This effect is enhanced by the action of radiation at the early stages of ferrite sintering by an electron beam. It was established for the first time that a change in the rate of radiative heating by two orders of magnitude and isothermal holding at the temperature of removal of polyvinyl alcohol (673 K) and melting of $Bi_2O_3$ (1093 K) do not affect the phase composition of the LiTiZnMn ferrite. Low-temperature variations in the cooling rate after sintering of the compacts do not lead to noticeable changes in the initial permeability. A decrease in the cooling rate in the high-temperature sintering region is accompanied by a monotonic increase in the initial permeability.

## REFERENCES

1  Lysenko E.N., Nikolaev E, Vlasov V.A., Surzhikov A.P. Microstructure and reactivity of Fe2O3-Li2CO3-ZnO ferrite system ball-milled in a planetary mill. *Thermochimica Acta*, 2018, Vol. 664, pp. 100 – 107.

2  Minin V.M. Effect of sintering conditions on the microstructure and electromagnetic properties of Li-Mg-Mn ferrite memory elements. *Soviet Powder Metallurgy and Metal Ceramics*. 1982, Vol. 21, pp. 698 – 701.

3  Zahir R., Chowdhury F.-U.-Z., Uddin M.M., et al. Structural, magnetic and electrical characterization of Cd substituted Mg ferrites synthesized by double sintering technique. *J. Magn. Magn. Mater*. 2016, Vol. 410, pp. 55 – 62.

4  Manjura Hoque S., Abdul Hakim M., Mamun Al, et al. Study of the bulk magnetic and electrical properties of MgFe2O4 synthesized by chemical method. *Materials Sciences and Applications*. 2011, Vol. 2, pp. 1564 – 1569.

5  Surzhikov A.P., Pritulov A.M., Lysenko E.N., et al. Calorimetric investigation of radiation-thermal synthesized lithium pentaferrite. *Journal of Thermal Analysis and Calorimetry*. 2010, Vol. 101, No. 1, pp. 11 – 13.

6  Zhuravlev V.A., Naiden E.P., Minin R.V., Itin V.I., Suslyaev V.I., Korovin E.Yu. Radiation-thermal synthesis of W-type hexaferrites. *IOP Conference Series Materials Science and Engineering*. 2015, Vol. 81, 012003.

7  Naiden, E.P., Zhuravlev, V.A., Minin, R.V., Suslyaev, V.I., Itin, V.I., Korovin, E. Yu. Structural and magnetic properties of SHS-produced multiphase W-type hexaferrites: influence of radiation-thermal treatment. *International Journal of Self-Propagating High-Temperature Synthesis*, 2015, Vol. 24, pp. 148 – 151.

8  Zhuravlev V.A., et al. Computer simulation of processes of radiation-thermal heating. *IOP Conference Series: Materials Science and Engineering*, 2015, Vol. 81, 012054. doi:10.1088/1757-899X/81/1/012054

9    Ancharova U.V., Mikhailenko M.A., Tolochko B.P., et al. Synthesis and Staging of the Phase Formation for Strontium Ferrites in Thermal and Radiation Thermal Reactions. *IOP Conference Series Materials Science and Engineering*, 2015, Vol. 81, 012122. doi:10.1088/1757-899X/81/1/011001

10   Ning K., Lu J., Xie P., et al. Study on surface modification of silicone rubber for composite insulator by electron beam irradiation. *Nuclear Instruments and Methods in Physics Research Section B: Beam Interactions with Materials and Atoms*, 2021, Vol. 499, pp. 7 – 16.  doi:10.1016/j.nimb.2021.04.019

11   Chettri P., Deka U., Rao A., Nagaraja K.K., et al, Dwivedi J. Effect of high energy electron beam irradiation on the structural properties, electrical resistivity and thermopower of $La_{0.5}Sr_{0.5}MnO3$ manganites. *Physica B: Condensed Matter*, 2020, Vol. 585, 412119. doi:10.1016/j.physb.2020.412119

12   Oane M., Toader D., Iacob N., Ticos C.M. Thermal phenomena induced in a small tungsten sample during irradiation with a few MeV electron beam: Experiment versus simulations. *Nuclear Instruments and Methods in Physics Research Section B: Beam Interactions with Materials and Atoms*, 2014, Vol. 337, pp. 17 – 20.

13   Salimov R.A., Cherepkov V.G., Kuksanov N.K., Kuznetzov, S.A. The use of electron accelerators for radiation disinfestation of grain, *Radiation Physics and Chemistry*, 2000, Vol. 57, pp. 625 – 627.

14   Salimov R.A., Cherepkov V.G., Golubenko J.I., et al. D.C. high power electron accelerators of ELV-series: status, development, applications. *J. Radiation Phys. Chem.* 2000, Vol. 57, pp. 661 – 665.

15   Cleland M.R., Parks L.A. Medium and high-energy electron beam radiation processing equipment for commercial applications. *Nucl. Instr. Meth. B.* 2003, Vol. 208, pp. 74 – 89.

16   Mehnert R. Review of industrial applications of electron accelerators. *Nucl. Instr. Meth. B* 1996, Vol. 113, pp.81–87.

17   Neronov V.A., Voronin A.P., Tatarintseva M.I., Melekhova T.E., Auslender V.L. Sintering under a high-power electron beam. *J. Less-Common Metals.* 1986, Vol. 117, pp. 391 – 394.

18   Kostishyn V., et al. Obtaining anisotropic hexaferrites for the base layers of microstrip SHF devices by the radiation-thermal sintering. *Eastern-European Journal of Enterprise Technologies*, 2016, Vol. 5, pp. 32 – 39.

19   Kostishin V.G., Andreev V.G., Korovushkin V.V., et al. Preparation of 2000NN ferrite ceramics by a complete and a short radiation-enhanced thermal sintering process. *Inorganic Materials*, 2014, Vol, 50, pp. 1317 – 1322.

20   Malyshev A.V., Lysenko E.N., Vlasov V.A., Nikolaeva S.A. Electromagnetic properties of $Li_{0.4}Fe_{2.4}Zn_{0.2}O_4$ ferrite sintered by continuous electron beam heating, *Ceramics International*, 2016, Vol. 42, pp. 16180 – 16183.

21   Neronov V.A., Voronin A.P., Tatarintseva M.I., Melekhova T.E., Auslender V.L. Sintering under a high-power electron beam. *Journal of the Less-Common Metals*, 1986. Vol. 117, pp. 391 – 394.

22   Solodkyi I., Bogomol I., Loboda P. High-speed electron beam sintering of WC-8Co under controlled temperature conditions, *International Journal of Refractory Metals and Hard Materials*, 2022, Vol. 102, 105730.

23   Auslender V.L. ILU-type electron accelerator for industrial technologies. *Nuclear Instruments and Methods in Physics Research Section B: Beam Interactions with Materials and Atoms*, 1994, Vol. 89, pp. 46 – 48.

24   Auslender V.L., Bryazgin A.A., Faktorovich B.L., Gorbunov V.A., Kokin E.N., Korobeinikov M.V., Voronin L.A. Accelerators for E-beam and X-ray processing, *Radiation Physics and Chemistry*, 2002, Vol. 63, pp. 613 – 615.

25   Tyutnev A.P., Saenko V.S., Vannikov A.V, Oskin V.E. Radiation induced dielectric effect in polymers, *Physica Status Solidi (a)*, 1984, Vol. 86, pp. 363 – 374.

26   Boev S.G.  Kinetics of charge formation in electron-irradiated dielectrics, *Soviet Surface Engineering and Applied Electrochemistry*, 1987, Vol. 2, pp. 69 – 72.

27   Lysenko E.N., Malyshev A.V., Vlasov V.A., et al. Microstructure and thermal analysis of lithium ferrite pre-milled in a high-energy ball mill. *Journal of Thermal Analysis and Calorimetry*, 2018, Vol. 134, No. 1, pp. 127 – 133.

28   Surzhikov A.P., Lysenko E.N., et al. Thermogravimetric investigation of the effect of annealing conditions on the soft ferrite phase homogeneity. *Journal of Thermal Analysis and Calorimetry.* 2011, Vol. 104, No. 2, pp. 613 – 617.

29   Stary O., Malyshev A.V., Lysenko E.N., Petrova A. Formation of magnetic properties of ferrites during radiation-thermal sintering. *Eurasian phys. tech. j.* 2020, Vol. 17, No. 2, pp. 6 – 10.

30   Surzhikov A.P., Frangulyan, T.S., Ghyngazov, S.A., Vasil'ev, I.P., Chernyavskii, A.V. Sintering of zirconia ceramics by intense high-energy electron beam. *Ceramics Int.* 2016, Vol. 42, No. 12, pp. 13888 – 13892.

31   Nikolaev E.V., Astafyev A.L., Nikolaeva S.A., Lysenko E.N., Zeinidenov A.K. Investigation of electrical properties homogeneity of Li-Ti-Zn ferrite ceramics. *Eurasian phys. tech. j.* 2020, Vol. 17, No. 1, pp. 5 – 12.

32   Surzhikov A.P., Malyshev A.V., Lysenko E.N., Stary O. Temperature dependences of the initial permeability of lithium-titanium ferrites produced by solid-state sintering in thermal and radiation-thermal modes.  *Eurasian phys. tech. j.* 2022, Vol. 19, No, 1, pp. 5 – 9.

33   Smith J., Wijn H.P.J. Ferrites: *Physical properties of ferromagnetic oxides in relation to their technical application.* 1959, Eindhoven, Phillips Technical Library, 233p.

34   Grishaev V.V., Lebed' B.M., Marchik I.I. Radiation-stimulated sintering of powder materials. *Electronic equipment. Ser. Materials.* 1983, Issue 5, pp. 13 – 17. [in Russian]

35   Letyuk L.M., et al. Special features of the formation of the microstructure of ferrites sintered in the presence of a liquid phase. *Izv.Vysshikh Uchebnykh Zavedenij - Chernaya Metallurgiya.* 1979, Vol. 11, pp. 124 – 127. [in Russian]

# THE EFFECT OF MOLYBDENUM DISULFIDE NANOPARTICLES ON THE PROPERTIES ZINC OXIDE ELECTRON TRANSPORT LAYER OF ORGANIC SOLAR CELLS

Aimukhanov A. K.[1], Seisembekova T. E.[1],  Zeinidenov A.K.[1], Ilyassov B.R.[2], Alexeev A.M.[3], Zhakhanova A.M.[1]

[1]E.A. Buketov Karaganda University, Scientific Center for Nanotechnology and Functional Nanomaterials, Karaganda, Kazakhstan, tosh_0809@mal.ru
[2]Astana IT University, Astana, Kazakhstan,
[3]Kazan Federal University, Kazan, Russia

*In this work, the effect of molybdenum disulfide nanoparticles on the properties zinc oxide electron transport layer of organic solar cells is studied. molybdenum disulfide nanoparticles were obtained by laser ablation of MoS2 powder in isopropyl alcohol. To form composite films, nanoparticles were added to a sol–gel zinc oxide solution with different concentrations. According to scanning electron microscope study, as the concentration of nanoparticles in the film increases, the thickness of the molybdenum disulfide layer on the zinc oxide surface changes. molybdenum disulfide nanoparticles in the film structure gradually fill the bulk and surface voids in zinc oxide. However, when the concentration exceeds 1%, holes and voids are formed in the film. The absorption spectra of composite films showed that as the concentration of nanoparticles in the film increases, the absorption intensity enhances due to the increase of the overall thickness. At the same time, zinc oxide optical band gap width does not change, which means the molybdenum disulfide nanoparticles do not affect the electronic structure of zinc oxide. It was shown that the observed changes in the* volt‑ampere characteristic *of organic solar cells with composite films electron transport layer composite films was associated with the influence of molybdenum disulfide nanoparticles on electron transport in* organic *solar cells. According to impedance spectroscopy study, it was found that molybdenum disulfide nanoparticles at concentration below critical value increases the lifetime of charge carriers and the diffusion coefficient in composite film.*

**Keywords:** zinc oxide, molybdenum disulfide, composite film, surface morphology, optical and impedance spectroscopy.

## Introduction

In inverted organic solar cells (OSCs), ZnO is used as electron transport layer (ETL) because of its high electron mobility, high visible light transmittance, stability in air and possibility to control electrical and optical properties. One of the reasons of the low power conversion efficiency of OSCs is the presence of bulk and surface defects in the ETL based on ZnO. Defects intensify the charge recombination, impede the charge transfer and reduce the efficiency of electron collection at electrodes [1]. To solve this problem, a number of researchers propose to use interfacial layers between the ZnO and the photoactive layer. For example, a two-layer ETL with conjugated polyelectrolyte was used [1], ZnO was doped with perylene bisimides [2-4], aluminum [5-7], fullerene derivatives [8,9] and Sn [10], which leads to the decrease in the electron work function, and to the improvement in electron transport in ZnO due to the decrease in the defect density.

Two-dimensional transition metal dichalcogenides (2D TMDs) can be also combined with ETL. The band gap, physical and chemical properties of 2D TMDs can be easily tuned by developing varies van der Waals structures in combination with other materials. In these materials, due to the special single-layer structure, the unshared pairs of electrons in the atoms of S and Se can provide rapid transport and as result increase the mobility of charge carriers. Graphene-like 2D materials have great potential and are alternatives to traditional hole transport layer (HTL) and ETL materials for organic solar cell  (OSC), Fig.1. J.-M. Yun et al. [11] showed the possibility to use transition metal dichalcogenide nanosheets as HTL and ETL layers in direct and inverted OSCs. However, nanosheets can not form a continuous layer, so they developed hybrid composite structures based on them. The authors of the work [1] reported that the increase of MoS2 nanosheet density in ZnO up to 0.5 wt.% led to the decrease in the interfacial resistance and the suppression

of the leakage current in devices, and as a result, power conversion efficiencies (PCE) boosted from 8.8% to 10.1%.

In our work to suppress bulk and surface defects in ZnO ETL, we doped ZnO ETL with MoS2 nanoparticles. MoS2 nanoparticles were added in ZnO solution and then composite ETLs were deposited. The effect of MoS2 nanoparticles on electron transport mechanisms in OSCs was studied in detail.
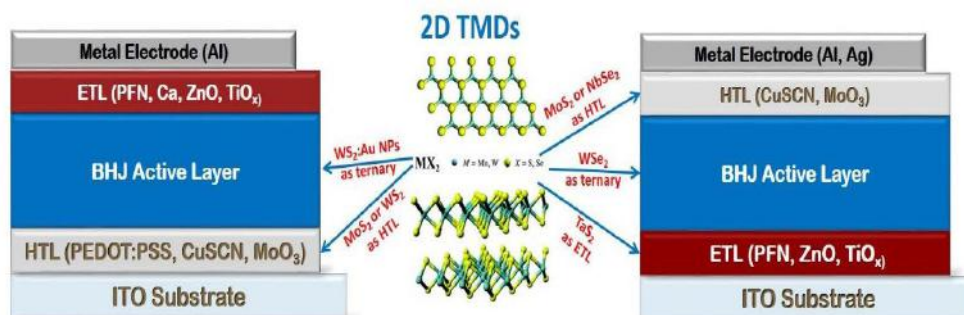


**Fig. 1**. Schematic diagram showing both the direct (left) and inverted OPVs structure. In the center the structure of various 2D TMDs are shown, and the blue arrows show the various layers in which TMDs were added [1].

## 1. Experimental part. Methods and materials

At first the FTO covered glass substrates were rigorously cleaned [12].The preparation of ZnO:MoS2 solution had the following steps: firstly, 98.7 mg of Zn5(OH)8Cl2 (pure 99.9% Sigma Aldrich) was dissolved in 1 ml of isoproponol (pure 99.9% Sigma Aldrich), then 75 µl of monoethanolamine (Sigma Aldrich) was added to the solution, after that, the solution was stirred at 60 °C for 2 hours, and then kept for 24 hours at room temperature, finally MoS2 nanoparticles were added to the solution with different concentrations. MoS2 nanoparticles were obtained by laser ablation of MoS2 powder by the second harmonic of a solid-state Nd:YAG laser (SOLAR LQ).

After, ZnO:MoS2 solution was spin-coated on clean FTO glass substrates by spin-coating techniques at the rotation speed of 4000 rpm. SPIN150i SPS was used for the spin-coating. Then the film was preheated in air at temperature of 200 °C for 15 minutes and immediately annealed at the temperature of 450 °C for one hour to form crystalline structure. Further, P3HT:IC60MA chlorobenzene solution (P3HT and IC60MA is pure 97% from Sigma Aldrich) with the ratio of 1:0.8 was spin-coated on ZnO:MoS2/FTO glass substrate to form the photoactive layer and annealed in air at a temperature of 140 °C for 10 minutes. Before creating inverted structure solar cells, P3HT:IC60MA solution was filtered using a syringe filter with a pore diameter of 0.45 microns. The rotation speed of the centrifuge was 2000 rpm, the rotation time at this speed was at least 30 seconds. After thermal annealing, a part of the photoactive layer was removed to provide access to the electrode on the surface of the FTO. Further, PEDOT:PSS solution was spin-coated to the substrates to form HTL [13]. Finally, silver electrodes was sputtered on PEDOT:PSS layer surface by thermal deposition (CY-1700x-spc-2 evaporator). The residual pressure in the working volume during operation did not exceed $10^{-4}$ Pa. The tantalum boat was used as a silver vaporizer. The current flowing through the boat during the spraying process varied in the range of 60-65 A [14].

## 2. Results and discussion

Morphology of ZnO:MoS2 nanocomposite ETLs was studied by a MIRA 3 LMU scanning electron microscope (TESCAN). In Fig.2 the surface morphologies and cross-sections of ZnO:MoS2 nanocomposite films with different concentrations of MoS2 nanoparticles are presented. As the concentration of nanoparticles increases, the thickness of the MoS2 layer changes. The morphology of the surface of composite films becomes smoother (Figure 2 a, b, c, d, e). The addition of MoS2 nanoparticles to ZnO enhances the generation and transport of charge in the mixture under study. This leads to an increase in the efficiency of solar energy conversion. A more efficient process of transporting charge carriers in the studied systems. It is worth noting that samples of nanocomposite films demonstrate various photoelectric and electrophysical characteristics.

These results indicate that MoS2 nanoparticles in the film structure gradually fill the bulk and surface voids in ZnO [15]. When nanoparticles are added in concentrations above 1%, holes and voids are formed in

the film (Fig.2f). Obviously, in this case, a uniform film is not formed. The quantitative content of MoS2 nanoparticles in ZnO was determined based on EDX analysis (Fig. 3).  The composition of the composite film includes elements such as Mo, S, Zn and O (Table 1). As the concentration of nanoparticles increases, so does the concentration of related elements.



a)                                            b)                                            c)

d)                                            e)                                            f)
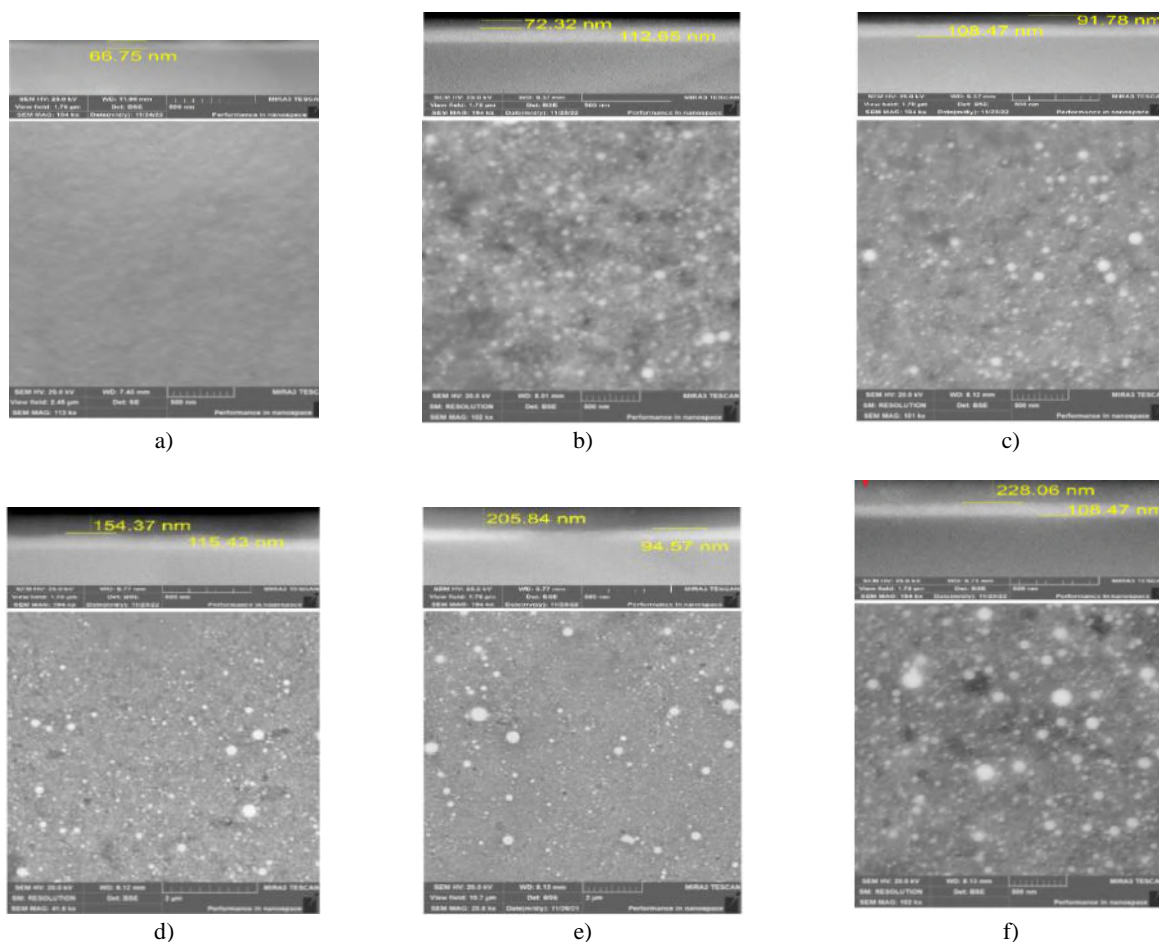
**Fig. 2**. Images of surface morphology of ZnO:MoS2 composite films
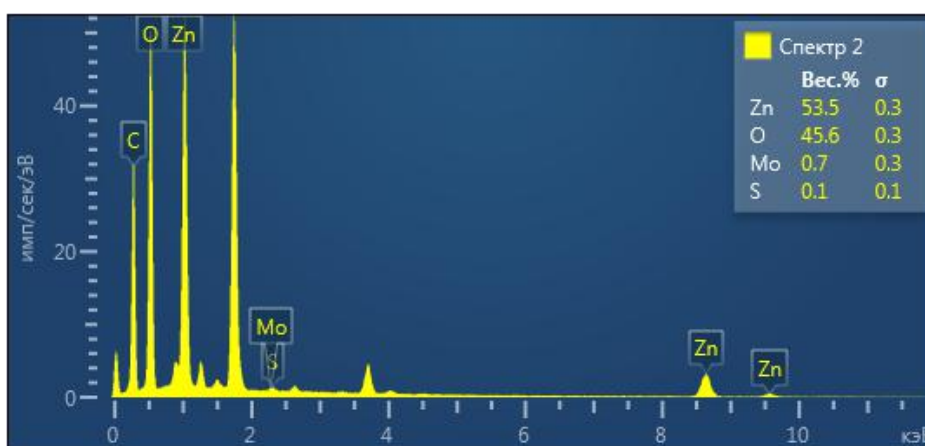


**Fig.3**. EDX analysis

Absorption spectra of ZnO and ZnO:MoS2 is shown in Fig. 4. As can be seen from the figure, as the concentration of nanoparticles in the film increases, the absorption of the film increases, which is associated with a change in the overall thickness. Using the Tauc graph, it was found that the values of the optical band gap width do not change, which indicates that the addition of MoS2 does not affect the electronic structure of

ZnO. The figure shows that the absorption spectrum of ZnO:MoS2 of the film is located in the range of 320-400 nm with peaks at 360 nm. When adding MoS2 nanoparticles, an increase in the optical density is observed.

**Table 1.** Elemental composition of ZnO:MoS2 composite films (Atomic percentages)

| Weight % | Mo, weight % | S, weight % | Zn, weight % | O, weight % |
|---|---|---|---|---|
| 0.2 | 0,7 | 0,1 | 53,5 | 45,6 |
| 0.4 | 1,6 | 0,8 | 54,4 | 43,2 |
| 0.6 | 2,1 | 2,0 | 53,6 | 42,3 |
| 0.8 | 3,7 | 2,5 | 51,9 | 41,8 |
| 1 | 4,7 | 2,7 | 51,9 | 40,7 |
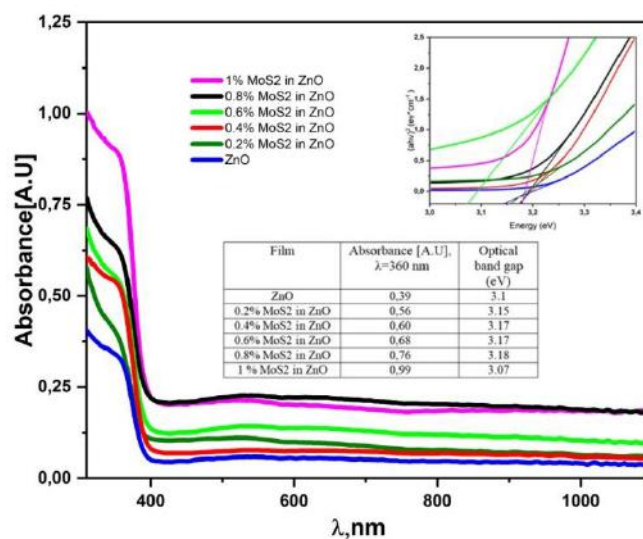


**Fig. 4**. Absorption spectra and Tauc plots (the inset) of ZnO:MoS2 composite films

In order to determine the effect of MoS2 nanoparticles on electron transport, a polymer solar cell with an inverted structure was assembled in a polymer solar cell. Upon photoexcitation of the photoactive layer P3HT:IC60MA, an electron-hole pair is formed, which then at the interface ZnO:MoS2/P3HT:IC60MA and P3HT:IC60MA/PEDOT:PSS decay into free charge carriers (Fig. 5). Electrons are injected into the ETL layer of ZnO:MoS2, and a hole is injected into the HTL layer of PEDOT:PSS.
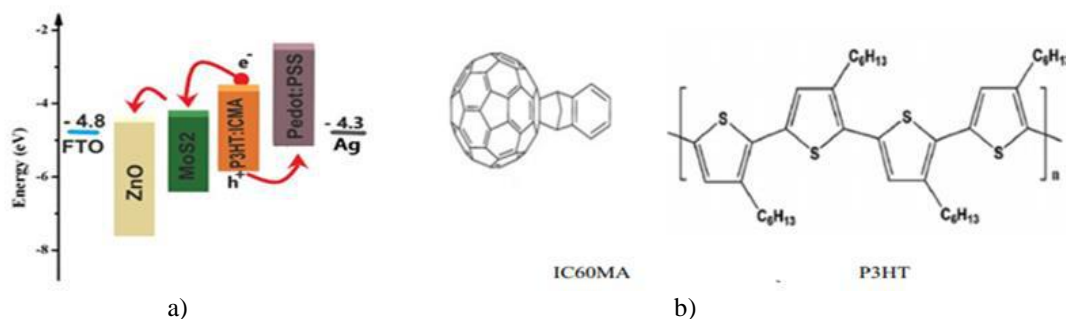


**Fig.5** (a) Energy level diagram of ZnO:MoS2 and (b) chemical structures of BHJ compounds

Samples of solar cells were prepared for the study of photovoltaic measurements, such as voltage characteristics and impedance spectra FTO/ZnO:MoS2/P3HT:IC60MA/PEDOT:PSS/Ag. Figure 6b shows that the addition of MoS2 nanoparticles affects the parameters of the VAC cells. For example, the filling factor of the composite cell 08% MoS2 in ZnO was FF = 0.42, and the value of the short-circuit current

density is equal to $J_{sc} = 10.5$ mA/cm$^2$. The maximum value of the increase in the VAC parameters is observed for the composite cell 08% MoS2 in ZnO, so the short-circuit current density increased by 3 times, the efficiency value was 2.6%.
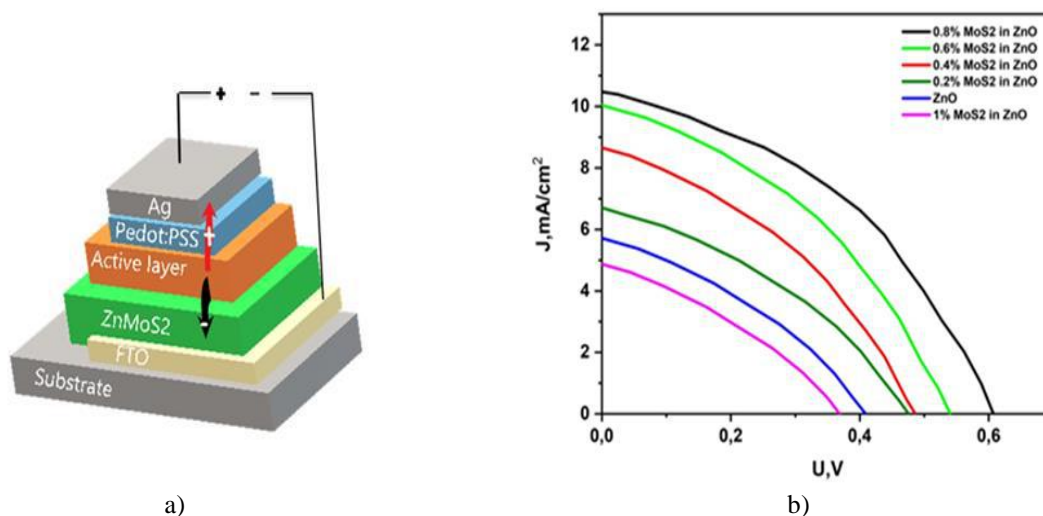


**Fig.6**. a) the architecture of the inverted PSC b) J–V characteristics of inverted solar cells

As the concentration of MoS2 increases to 0.8%, an increase in the parameters of the VAC is observed. A further increase in the MoS2 concentration leads to a decrease in the values of the VAC parameters. The obtained data correlate with the results of the morphology of the surface of composite films. 1% MoS2 in ZnO this sample has the lowest value of the fill factor and the lowest value of the maximum voltage. The inverted composite cell with added MoS2 nanoparticles has a low no-load voltage ($U_{oc} = 0.30$ V) among all the samples obtained. At the same time, this sample shows the lowest efficiency value among nanocomposites, equal to 0.5%.

**Table 2**. Photovoltaic characteristics of organic solar cells.

| Sample | $U_{oc}$ (V) | $J_{sc}$ (mA/cm$^2$) | $U_{max}$(V) | $J_{max}$ (mA/cm$^2$) | FF | PCE % |
|--------|------|------|------|------|------|------|
| ZnO | 0.4 | 5.7 | 0.24 | 3.37 | 0.35 | 0.7 |
| 0.2% MoS2 | 0.4 | 6.6 | 0.25 | 4.4 | 0.35 | 0.9 |
| 0.4% MoS2 | 0.4 | 8.6 | 0.30 | 5.2 | 0.37 | 1.3 |
| 0.6% MoS2 | 0.5 | 10.2 | 0.35 | 6.5 | 0.42 | 2.1 |
| 0.8% MoS2 | 0.6 | 10.5 | 0.39 | 6.9 | 0.42 | 2.6 |
| 1% MoS2 | 0.3 | 4.7 | 0.21 | 2.7 | 0.33 | 0.5 |

The observed changes in the IV curve are associated with the effect of MoS2 nanoparticles on electron transport in OSCs. To study in detail the effect of MoS2 nanoparticles on the kinetics of electron transport and recombination in OSCs, the impedance spectra of OSCs were measured. Fitting and analysis of spectrum parameters were carried out using the EIS-analyzer software package. With the using of this software, the values of capacity C and the values of $R_1$ and $R_2$ were calculated. The analysis of the impedance measurement results was carried out according to the diffusion-recombination model.

Fig. 7b shows the measured impedance spectra (points) of OSCs. The impedance spectra are described by an equivalent electrical circuit shown in the inset of Fig. 6a, where $R_1$ is the equivalent resistance of the external electrodes ($R_{FTO}$ + $R_{ZnO:MoS2}$ + PEDOT:PSS +Ag), $R_2$C is characterized by the photoactive layer/ZnO:MoS2 interface.

Since the films were obtained under the same conditions, the observed changes are associated with a change in the photoactive layer/ZnO:MoS2 interface. The greater the $R_2$, the lower the recombination rate at the phase interface. As can be seen from Table 3, an increase in the concentration of MoS2 nanoparticles also leads to a decrease in recombination resistance, which indicates an increase in recombination processes.
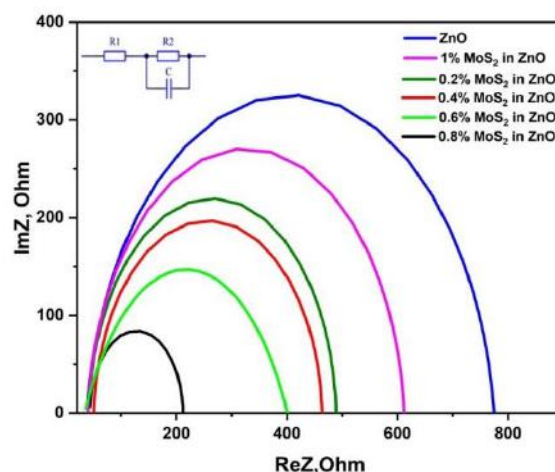
**Fig.7**.  Impedance spectra of PSCs

Table 3 shows the obtained values of $R_1$ $R_2$ and C. As can be seen from Table 3, the value of $R_1$ represents the total resistance of the external electrodes and adjacent ETL and HTL layers. Since all functional layers except ZnO are in the cells under ZnO:MoS2 were obtained under the same conditions, the observed changes in $R_1$ are associated with a change in the resistance of ZnO:MoS2 films. $R_1$ has a minimum value at the cell with the maximum concentration of MoS2. $R_2$, the resistance characterizing electron recombination at the photoactive layer/ZnO:MoS2 interface, varies depending on the concentration of MoS2 nanoparticles.

**Table 3.** The value of the electrophysical parameters of ZnO:MoS2 composite films

| Sample | $R_1$, (ohm) | $R_2$, (ohm) | $R_1 / R_2$ | $\tau_{eff}$, (ms) | $k_{eff}$, (s$^{-1}$) | $D_{eff}$, (см$^2$·с$^{-1}$) |
|---|---|---|---|---|---|---|
| ZnO | 47 | 737 | 15.7 | 2.4 | 404 | $1.1 \cdot 10^{-5}$ |
| 0.2% MoS2 | 27 | 383 | 14.1 | 2.6 | 373 | $1.9 \cdot 10^{-7}$ |
| 0.4% MoS2 | 30 | 449 | 14.9 | 3.1 | 319 | $2.6 \cdot 10^{-7}$ |
| 0.6% MoS2 | 30 | 432 | 14.4 | 3.7 | 264 | $3.5 \cdot 10^{-7}$ |
| 0.8% MoS2 | 16 | 178 | 11.1 | 8.6 | 115 | $4.1 \cdot 10^{-7}$ |
| 1% MoS2 | 37 | 569 | 15.4 | 2.6 | 372 | $1.4 \cdot 10^{-6}$ |

After photoexcitation, electrons from the photoactive layer are injected into ZnO:MoS2 and diffuse to the external electrode. At the same time, the reverse process occurs - the recombination of an electron with a hole into a photoactive layer. Usually, recombination occurs through surface defect levels in ZnO. Impedance spectroscopy also allows us to calculate the time constant $\tau = RC$, which characterizes the lifetime of charge carriers in ZnO:MoS2. It follows from the fitting data of the impedance spectra that $\tau$ has the maximum value for ZnO:MoS2 with a concentration of 0.8% nanoparticles. The impedance analysis data is correlated with the VAC data. OSCs with ZnO:MoS2 0.8% of nanoparticles form ETL films with improved conductivity and less structural defects. A sharp deterioration in the photovoltaic parameters of OSCs with ZnO over 0.8% of the MoS2 nanoparticle may be due to a infringement of the integrity of the film, which causes holes and voids to form in the film, through which current leakage occurs.

### Conclusions

In this paper, the effect of MoS2 nanoparticles on the morphology, optical and electric properties of ZnO electron transport layer of polymer solar cells is investigated. In the absorption spectra of ZnO:MoS2 composite films, an increase in the absorption intensity is observed. An increase in the absorption of the film

is associated with a change in the overall thickness. At the same time, the nanoparticles do not affect the electronic structure of ZnO. It is shown that the addition of MoS2 nanoparticles has an effect on the photoelectric and electrophysical parameters of the film in the polymer solar cell. It has been shown that the changes in the IV characteristic of OSCs based on $ZnO:MoS_2$ ETL are associated with the influence of MoS2 nanoparticles on electron transport. It was found that MoS2 nanoparticles at a concentration of 0.8% increase the lifetime of charge carriers and the diffusion coefficient in composite ETL ZnO:MoS2 and also the maximum value of the increase in the parameters of the VAC is observed for the composite cell 0.8%. As a result, the short-circuit current density increased by 3 times, the efficiency value was 2.6%.

## Acknowledgments

## REFERENCES

1    Huang Yi-J., Chen H.-Ch., Lin H.-K. Doping ZnO Electron Transport Layers with MoS2 Nanosheets Enhances the Efficiency of Polymer Solar Cells. *ACS Appl. Mater. Interfaces*. 2018, pp. 1- 31. doi:10.1021/acsami.8b06413

2    Nian L., Zhang W., Zhu N. Photoconductive Cathode Interlayer for Highly Efficient Inverted Polymer Solar Cells. *J. Am. Chem. Soc*. 2015, 137 (22), pp. 6995 – 6998. doi:10.1021/jacs.5b02168

3    Nian L., Gao K., Liu F. 11% Efficient Ternary Organic Solar Cells with High Composition Tolerance via Integrated Near-IR Sensitization and Interface Engineering. *Adv. Mater*. 2016, pp. 8184 – 8190. doi:10.1002/adma.201602834

4    Nian L., Chen Z., Herbst S. Aqueous Solution Processed Photoconductive Cathode Interlayer for High Performance Polymer Solar Cells with Thick Interlayer and Thick Active Layer. *Adv. Mater*. 2016, pp.7521–7526. doi: 10.1002/adma.201601615

5    Liu X., Li X., Li Y. High-Performance Polymer Solar Cells with PCE of 10.42% via Al-Doped ZnO Cathode Interlayer. *Adv. Mater*. 2016, pp.7405–7412. doi:10.1002/adma.201601814

6    Yang Z., Zhang T., Li J. Multiple Electron Transporting Layers and Their Excellent Properties Based on Organic Solar Cell. *Sci. Rep*. 2017, 7 (1), 9571. doi:10.1038/s41598-017-08613-7

7    Lin Z., Chang J., Zhang C. Enhanced Performance and Stability Page 20 of 31 ACS Paragon Plus Environment ACS Applied Materials & Interfaces of Polymer Solar Cells by In Situ Formed AlOX Passivation and Doping. *J. Phys. Chem*. 2017, 121 (19), pp.10275–10281. doi:10.1021/acsami.0c09046

8    Liao S.H., Jhuo H.J. Cheng Y.S. Fullerene Derivative-Doped Zinc Oxide Nanofilm as the Cathode of Inverted Polymer Solar Cells with Low-Bandgap Polymer (PTB7-Th) for High Performance. *Adv. Mater*. 2013, 25 (34), pp.4766–4771. doi:10.1002/adma.201301476

9    Liao S.-H., Jhuo H.-J, Yeh P.-N. Single Junction Inverted Polymer Solar Cell Reaching Power Conversion Efficiency 10.31% by Employing Dual-Doped Zinc Oxide Nano-Film as Cathode Interlayer. *Sci. Rep*. 2015, 4 (1), 6813. doi:10.1038/srep06813

10   Wei J., Yin Z., Chen S. C., Low-Temperature Solution-Processed Zinc Tin Oxide Film as a Cathode Interlayer for Organic Solar Cells. *ACS Appl. Mater. Interfaces,* 2017, 9 (7), pp.6186–6193. doi:10.1021/acsami.6b13724

11   Yun J.M., Noh Y.J., Yeo JS. Efficient work-function engineering of solution processed MoS2 thin-films for novel hole and electron transport layers leading to high-performance polymer solar cells, *J. Mater. Chem*. 2013, pp.3777 – 3783. doi:10.1039/C3TC30504J

12   Ilyassov B., Ibrayev N., Hierarchically assembled nanostructures and their photovoltaic properties. *J. Mater. Sci. Semicond. Process*. 2015, 40, pp.885–889. doi:10.1016/j.mssp.2015.07.087

13   Aimukhanov A.K., Seisembekova T.E., Zeinidenov A.K., The impact of SnO2 photoelectrode's thickness on photovoltaic properties of the solar cell FTO:SnO2:PTB7-TH:ITIC/Mo/Ag. *Bulletin of the Karaganda University, series Physics. 2022, №2(106),* pp.86-91. doi:10.31489/2022PH2/86-91

14   Zeinidenov A.K., Aimukhanov A.K., Ilyassov B.R. Impact of the annealing temperature of In2O3 films on the photovoltaic characteristics of a polymer solar cells. *Eurasian Physical Technical Journal*. 2022, Vol.19, №1(39). pp. 34–39. doi:10.31489/2022No1/34-39.

15   Gao M., Zhang M., Niu W. Tuning the transport behavior of centimeter-scale WTe2 ultrathin films fabricated by pulsed laser deposition. *Appl. Phys. Lett*. 2017, 111(3), 031906. doi:10.1063/1.4995227

# DYNAMIC VISCOSITY OF THE LUBRICANT AND ITS EFFECT ON STEEL MATERIALS WITH BORON

Kubich V.I.[1], Cherneta O.G.[2]

[1]National University "Zaporizhzhya polytechnic", Zaporizhia, Ukraine, schmirung@gmail.com

[2]Dniprovsk State Technical University, Kamenskoye, Ukraine, ocherneta@gmail.com

*In this work, the regularities of the change in the shear strength of the adhesive bond $\tau_0$ and the piezoelectric coefficient $\beta$ in the metal systems "12Kh2N4 (45KhN2MFA) - steel 45 + B", "12Kh2N4 (45KhN2MFA) - steel 45 + VS" were obtained during physical modeling of the shear of surfaces of small-sized samples and changes in dynamic viscosity environment of their interaction with the use of additional equipment of the SMTs-2 friction machine. It has been established that boriding and boron carburizing of the surface of steel 45 leads to the absence of adhesion to the surfaces of steels 12Kh2N4 and 45KhN2MFA in certain ranges of normal pressures, at which $\tau_0 > 0$ and the dynamic viscosity of liquid and grease. It was found that the parameter $\tau_0$ when lubricating surfaces is determined to a greater extent for the system "12X2H4 - steel 45", and partially for borating steel 45 and low values of dynamic viscosity $\mu = 0.027$ Pa•s. With an increase in the dynamic viscosity of the liquid phase of the lubricant in the "12X2H4 - steel 45" system, there is a tendency to an increase in the value of $\tau_0$. It was found that the absence of modification of steel 45 with boron and boron carbide predetermines the independence of the piezoelectric coefficient from the viscosity of the liquid lubricant and the shear rate. Boriding and boron carburizing steel 45 predetermines an increase in the piezoelectric coefficient by an average of 1.6 times with an increase in dynamic viscosity from 0.027 Pa•s to 0.19 Pa•s at a shear rate of $10.16 \pm 0.8$. At shear rate $= 5.08 \pm 0.6$ mm/s, the piezoelectric coefficient is relatively constant in the systems under study. With the transition to contact through a grease lubricant, there is an ambiguous manifestation of the rate of change of the piezoelectric coefficient.*

*Keywords:* piezo coefficient, dynamic viscosity, lubricant, shear rate, tangential strength

## Introduction

Forecasting the resource of mechanisms of mechanical engineering objects presupposes the presence of certain initial data. In this case, the main quantity is the wear rate of the surfaces of materials, which is determined both experimentally and theoretically. So, for example, when calculating the service life of a gear pair, it is necessary to know not only the geometric parameters of the engagement, but also the parameters of the adhesion properties and fatigue of the contacting surfaces. This is especially important when measures are proposed to modify the working surfaces to improve the physical and mechanical properties of metals. The existing structural alloy steels 12Kh2H4, 45KhH2MFA, high-quality carbon steel 45 are widely used for the manufacture of a wide range of mechanical engineering parts, including gears, gear shafts of gear drives for various purposes. Undoubtedly, the presence of numerical values of the parameters of the adhesion properties of the listed jointly working metals will determine the accuracy of the calculations performed, and the possible surface modification of one of them will expand the information on the nature of its influence on the manifestation of these parameters. Based on the above, the establishment of regularities in the manifestation of the parameters of adhesion properties in systems of structural metals seems to be an urgent scientific and fundamental task considered in tribology.

## 1. Review of previous publications, setting the goal of the work

The technology of surface modification of steel 45 by boriding and boron cementation is proposed, which predetermines the change in both the phase composition of the surface structures and their hardness [1-3]. Boriding of steel refers to the saturation of steel with the element boron. After such saturation, the surface layer with a size of about 0.3 mm becomes hardened with a hardness of 18000-20000 HV. The industry uses boron in solid, liquid and gaseous states. The disadvantage of the method is the fragility of the

surface layer, which can break off after impact. Boron cementation of steel is the process of simultaneously saturating its surface with elements of boron and carbon. This process is carried out at a temperature of about 1200 K using boron carbide. As a result of boron cementation, the hardness increases by 1.2-1.4 times and relative wear resistance in comparison with the carburizing process.

In [4], the regularities of the change in the shear strength of the adhesive bond τ0 and the piezoelectric coefficient β in the metal systems "steel 45 - 40X", "steel 45 + B - 40X", "steel 45 + BC - 40X" were obtained during physical modeling of the shear between small samples in the environment of lubricants I-20A, Wolf 10W-40, TAD-17i, Litol-24 with distinctive dynamic viscosities using additional equipment of the SMTs-2 friction machine. At the same time, the features of the manifestation of the parameters of the adhesion bond depending on the shear rate have been established. The results obtained are typical for systems of materials in which alloyed structural steel 40X is a constant element. This steel has one alloying element chromium, which predetermines the amount of surface energy, due to a greater extent to the chemical element - iron.

Steels 12Kh2N4, 45KhN2MFA can be alternative steel 40Kh structural metals, for example, as discussed above, for the manufacture of gears. Moreover, they have a different content of chemical elements, and, accordingly, surface energy (surface tension [5, 6]), which will affect the formation of adhesive interaction in contact with steel 45 when it is modified with boron and boron carbide. Moreover, the hardness of steels 12Kh2N4, 45KhN2MFA is less than steel 40Kh. From this, it is evident that it is necessary to perform not only an assessment of the manifestation of adhesion parameters in systems of metals with steels 12Kh2N4, 45KhN2MFA, but also to establish their change depending on the decrease in the hardness of one of the elements of the friction pair, in this case it is a direct pair.

The aim of the work is to establish the regularities of changes in the parameters of the adhesive bond in the systems of materials "steel 45 – 45KhN2MFA", "steel 45 + B - 45KhH2MFA", "steel 45 + VS - 45KhH2MFA", "steel 45 - 12Kh2H4", "steel 45 + B - 12Kh2H4 "," steel 45 + BC - 12Kh2H4 "in the physical modeling of the shift between small-sized samples in the environment of lubricants with distinctive dynamic viscosities using additional equipment of the SMTs-2 friction machine. Based on the above, this work seems to be a continuation of the complex of studies begun in [3, 4, 7].

## 2. Research methodology

The parameters of the adhesive bond were evaluated using an SMTs-2 friction machine with additional equipment in accordance with the procedure described in [7]. In this case, movable samples - disks were made of steels 12Kh2N4, 45KhN2MFA, and fixed pads in the form of triangular-shaped segments of steel 45 with surface modification with boron and boron carbide, i.e. the same samples were used as in [4]. To estimate the pressure in the contact zone and the tangential shear strength, we used the average values of the contour areas, which were determined from the indentations. The modeling of the manifestation of the properties of the lubricating medium was carried out using the same lubricants as in [4]. The following lubricants were applied to the surface of the samples:

- industrial oil I-20A (GOST 20799-88), dynamic viscosity at 40 ºC $\mu = 0.027$ Pa•s;
- transmission oil TAD-17i (GOST 23652-79), dynamic viscosity at 50 ºC $\mu = 0.106$ Pa•s;
- semi-synthetic motor oil Wolf 10W-40 API SL/SF, dynamic viscosity at 40 ºC $\mu = 0.19$ Pa•s;
- Litol-24 grease (GOST 21150-2017), dynamic viscosity at 50 ºC $\mu = 8$ Pa•s.

This choice of lubricants determined, firstly, different values of the dynamic viscosity for the liquid state of aggregation of the lubricating medium, and secondly, the presence of a consistent medium. This makes it possible to take into account the possible contact interaction of the surfaces of the teeth of gears of various gears, for example, in mechanical drives of machine tools, transmission units for cars and tractors, gearboxes of hand-held power tools, etc.

To assess the parameters of adhesion without lubricant, the surfaces were thoroughly degreased with gasoline "Kalosha".

## 3. Research results and their discussion

As a result of processing the tribograms of the shear surfaces of a stepwise loaded contact in the considered systems of materials, statistical data were obtained, which are summarized in tables 1, 2. Analysis of the data obtained indicates the following. First, the parameter τ0 is determined only:

- in the absence of lubricant for the system "45KhN2MFA - steel 45". In this case, exclusively boronization of the surface of steel 45 leads to a slight increase in the value of τ0 from 3.58 MPa to 5.6 MPa;

- when lubricating surfaces to a greater extent for the system "12Kh2H4 - steel 45" in the absence of surface modification of steel 45, as well as when it is boriding and low values of dynamic viscosity μ = 0.027 Pa•s. In this case, with an increase in the dynamic viscosity of the liquid phase of the interaction lubricant, a tendency to an increase in the value of τ0 is observed. To a lesser extent, this parameter manifested itself for the system "45KhN2MFA - steel 45" again with dynamic viscosity μ = 0.027 Pa•s, but without modification of steel 45. On the whole, the results obtained confirm the thesis given in [5] on the structural sensitivity of the adhesive parameters. The manifestation of the adhesive interaction parameter τ0 in the absence of lubrication can be explained by the ratio of the hardness of the interacting surfaces. According to the research conditions, H12Kh2H4 <H45KhH2MFA <H45, and H45 <H45 + B <H45 + BC.

**Table 1.** Parameters of approximation of experimental data for the system of materials "45KhN2MFA - steel 45 (+ B, + VS)" in the environment of lubricants

| Parameter | Steel 45 | | | | Steel 45+B | | | | Steel 45+BC | | | |
|---|---|---|---|---|---|---|---|---|---|---|---|---|
| Lubricant | I-20 | TAD-17и | Wolf 10W40 | Lithol -24 | I-20 | TAD-17и | Wolf 10W40 | Lithol -24 | I-20 | TAD-17и | Wolf 10W40 | Lithol -24 |
| Piezo coefficient $\beta$ | $\tau = 0,11p + 3,58$ | | | | $\tau = 0,05p + 5,6$ | | | | $\tau = 0,24p - 18,9$ | | | |
| | - | | | | $\tau = 0,14p - 0,24$ | | | | $\tau = 0,38p - 33,3$ | | | |
| | 0,12 | 0,13 | 0,12 | 0,12 | 0,15 | 0,13 | 0,17 | 0,12 | 0,11 | 0,1 | 0,14 | 0,15 |
| | - | - | - | - | 0,24 | 0,21 | 0,21 | 0,17 | 0,14 | 0,14 | 0,16 | 0,13 |
| Tangential strength $\tau_0$, MPa | 2,02 | >0 at $p{\approx}23$ MPa | >0 at $p{\approx}2$ MPa | >0 at $p{\approx}23$ MPa | >0 af $p{\approx}30$ MPa | >0 at $p{\approx}26$ MPa | >0 at $p{\approx}58$ MPa | >0 at $p{\approx}38$ MPa | >0 at $p{\approx}23$ MPa | >0 at $p{\approx}18$ MPa | >0 at $p{\approx}52$ MPa | >0 at $p{\approx}23$ MPa |
| | - | - | - | - | >0 at $p{\approx}40$ MPa | >0 at $p{\approx}48$ MPa | >0 at $p{\approx}46$ MPa | >0 at $p{\approx}40$ MPa | >0 at $p{\approx}24$ MPa | >0 at $p{\approx}18$ MPa | >0 at $p{\approx}56$ MPa | >0 at $p{\approx}88$ MPa |

Note. 1. The upper row of values at a shear rate $\upsilon_1 = 10.16 \pm 0.8$ mm/s, the lower one at $\upsilon_2 = 5.08 \pm 0.6$ mm/s.
2. The equation of the form is given for a system without lubricant.

**Table 2.** Parameters of approximation of experimental data for the system of materials "12Kh2H4 - steel 45 (+ B, + BC)" in the environment of lubricants

| Parameter | Steel 45 | | | | Steel 45+B | | | | Steel 45+BC | | | |
|---|---|---|---|---|---|---|---|---|---|---|---|---|
| Lubricant | I-20 | TAD-17и | Wolf 10W40 | Lithol -24 | I-20 | TAD-17и | Wolf 10W40 | Lithol -24 | I-20 | TAD-17и | Wolf 10W40 | Lithol -24 |
| Piezo coefficient $\beta$ | $\tau = 0,36p - 13,44$ | | | | $\tau = 0,2p - 10,5$ | | | | $\tau = 0,33p - 32,3$ | | | |
| | - | | | | $\tau = 0,2p - 5,56$ | | | | $\tau = 0,37p - 33,8$ | | | |
| | 0,1 | 0,11 | 0,1 | 0,15 | 0,11 | 0,18 | 0,17 | 0,1 | 0,18 | 0,16 | 0,18 | 0,13 |
| | - | - | - | - | 0,15 | 0,15 | 0,15 | 0,14 | 0,11 | 0,14 | 0,14 | 0,12 |
| Tangential strength $\tau_0$, MPa | 8.3 | 4,8 | 10,7 | >0 at $p{\approx}24$ MPa | 1,0 | >0 at $p{\approx}30$ MPa | >0 at $p{\approx}54$ MPa | 1,0 | >0 at $p{\approx}42$ MPa | >0 at $p{\approx}44$ MPa | >0 at $p{\approx}60$ MPa | >0 at $p{\approx}5$ MPa |
| | - | - | - | - | 1,21 | >0 at $p{\approx}17$ MPa | 0,5 | >0 at $p{\approx}17$ MPa | 0,1 | >0 at $p{\approx}62$ MPa | >0 at $p{\approx}58$ MPa | >0 at $p{\approx}38$ MPa |

Note. 1. The upper row of values at a shear rate $\upsilon_1 = 10.16 \pm 0.8$ mm/s, the lower one at $\upsilon_2 = 5.08 \pm 0.6$ mm/s. 2. The equation of the form is given for a system without lubricant.

From which it follows that in each of the contact options, the parameter $\tau_0$ is extrapolated back after the manifestation of plastic, elastic-plastic and elastic deformation of the microprofiles of metal surfaces. Such interaction can be estimated in accordance with the relaxation theory of adhesion, which considers deformation processes, the appearance of internal stresses in the thinnest surface layers and their subsequent relaxation [8]. In this case, the deformable metal layers have different thicknesses with one interface. When the load is removed during elastic deformation, the dimensions are restored, i.e., there is a sufficiently large supply of internal mechanical energy in the near-surface layers. From which it follows that such an energy reserve is capable of forming, among other things, the action of surface forces of adhesive interaction. While the supply of such energy can be critically maximum only up to a certain value from the point of view of a possible increase in the surface energy of one of the components of the system. This is exactly what happened when modifying steel 45 with boron carbide, i.e. it is possible to change the mechanism of adhesive interaction by the nature of its appearance.

The manifestation of the parameter $\tau_0$ of adhesive interaction in a lubricating medium can be explained by a large adsorption decrease in surface strength (Rebinder effect) for a less solid component of the system of materials, which predetermines the formation of the manifested large adhesion forces with a harder surface. Those. the less solid surface of the component of the metal systems under study seems to be more susceptible to penetration of the less viscous liquid phase of the lubricant, which manifested itself for the system "12Kh2H4 - steel 45". Based on the above, the considered interaction can be estimated in accordance with the theory of weak boundary layers [8].

In accordance with this theory, "weak" boundary layers with physicochemical properties that differ from those of the underlying layers are formed in the contact zone. In this case, it is the "weak" layers that determine the strength of the adhesive bond. In this case, the deformable metal layers have different thicknesses, but already with two interfaces. The first interface is formed by the elements "body (rotating disk, material 12Kh2H4, 45KhH2MFA) - a near-surface layer of a lubricant with bulk properties". The second surface is "a near-surface layer of a lubricant with bulk properties - a counterbody (fixed block, material steel 45)". From which it follows that the shear fracture mechanism can be not only cohesive [8], that is, within the adsorbed and deformed molecules of the lubricant (transition regions), but also mixed, taking into account the destruction of bonds along the interfaces. The latter is explained by the characteristics of the microprofiles of the contacting surfaces, which causes uneven deformation of the lubricant molecules distributed between them.

Second, boriding and boron carburizing of the surface of steel 45 leads to the absence of adhesion to the surfaces of steels 12Kh2N4 and 45KhN2MFA in certain ranges of normal pressures, at which $\tau_0 > 0$. This range is determined by the upper limit of the mechanical pressure p. In general, the following holds:

- a larger range of pressures is typical for the system "12Kh2H4 - steel 45", which, for example, at a shear rate of $\upsilon_1 = 10.16 \pm 0.8$ mm/s for liquid lubricant is from 0 to 42 MPa when borated steel 45, and from 0 to 48 MPa with its boron carburizing. For grease, this range is much smaller - from 0 to 17 MPa for boriding, and from 0 to 5 MPa for boron carburizing. At the same time, a twofold decrease in the shear rate leads to a decrease in the average range in a liquid medium by 2.5 times during boriding, and an increase in the range by 1.25 times for a liquid lubricant during boron cementation;

- a smaller range of pressures is typical for the system "45KhN2MFA - steel 45", which, for example, at a shear rate of $\upsilon_1 = 10.16 \pm 0.8$ mm/s for a liquid lubricant is from 0 to 38 MPa when boriding steel 45, and from 0 to 31 MPa with its boron carburizing. However, for grease, this range appeared from 0 to 38 MPa for boriding, and from 0 to 23 MPa for boron carburizing. At the same time, a twofold decrease in the shear rate leads to an insignificant increase in the average range in a liquid medium during boriding, and its equality for a liquid lubricant during boron cementation. For grease, the range was preserved within the same boundaries during boriding as in a liquid medium, and its increase by 3.8 times during boron cementation.

For a more detailed and visual assessment of the dependence of the upper pressure limit on the change in the dynamic viscosity of the liquid lubricant in accordance with the data of table 1, 2, graphical dependencies are built, Fig. 1, 2. From Figure 1 it follows that in the material system "45KhN2MFA - steel 45", the change in the dynamic viscosity of the liquid lubricant, starting from 0.11-0.12 Pa • s, predetermines an increase in the pressure of the beginning of the manifestation of adhesion forces during boron cementation of steel 45 and the shear rate of $5.08 \pm 0.6$ mm/s. The same takes place when it is borated and boron-cemented, but at a shear rate of $10.16 \pm 0.8$ mm/s. At the same time, the intensity of its growth remains unchanged. The viscosity in the range from 0.01 to 0.11 Pa•s does not affect the change in the beginning of

the manifestation of adhesion between the surfaces during boriding and boron-carburizing steel 45. The viscosity also does not affect the beginning of the manifestation of adhesion between the surfaces of the systems under study, even in the absence of modification, steel 45.



a)                                                                      b)
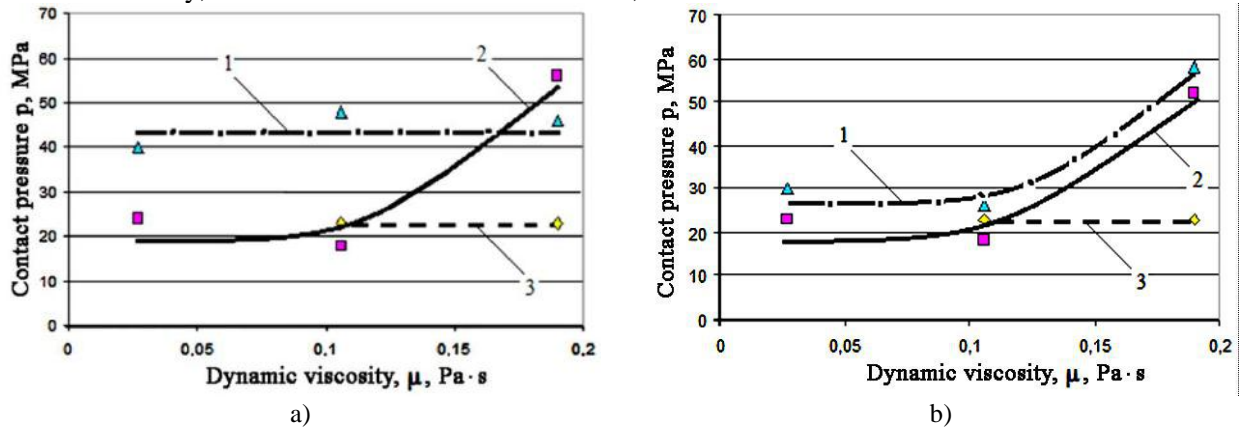
**Fig.1.** Influence of dynamic viscosity on the manifestation of adhesion in the system of materials "45KhN2MFA - steel 45" by pressure in contact: a - at $\upsilon_2 = 5.08 \pm 0.6$ mm/s; b - at $\upsilon_1 = 10.16 \pm 0.8$ mm/s; 1 - steel 45 when boriding; 2 - with boron carburizing steel 45; 3 - steel 45 without modification.



a)                                                                      b)
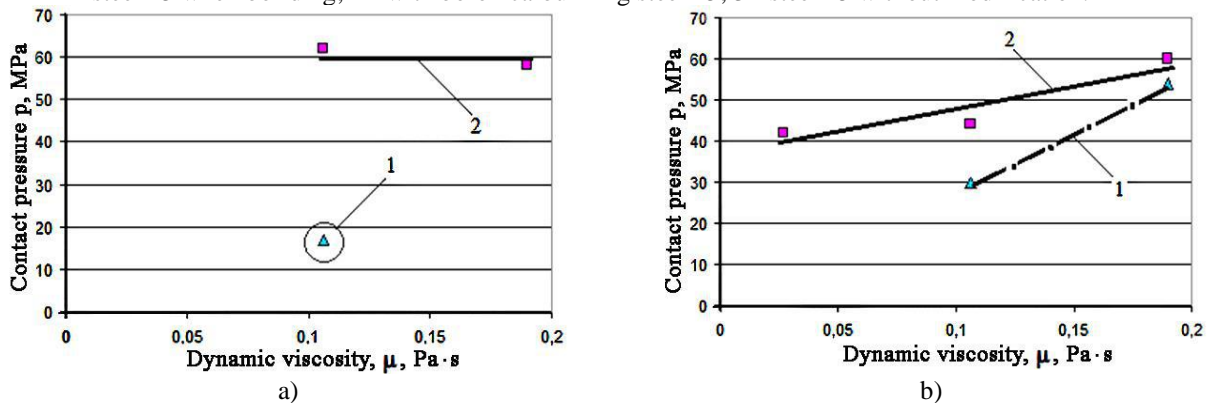
**Fig.2.** Influence of dynamic viscosity on the manifestation of adhesion in the system of materials "12Kh2H4 - steel 45" by pressure in contact: a) - at $\upsilon_2 = 5.08 \pm 0.6$ mm/s; b) - at $\upsilon_1 = 10.16 \pm 0.8$ mm/s; 1 - steel 45 when boriding; 2 - with boron carburizing steel 45

From Figure 2 it follows that in the system of materials "12Kh2H4 - steel 45" only at a shear rate of $10.16 \pm 0.8$ mm/s, a change in viscosity causes a linear increase in the pressure of the beginning of the manifestation of adhesion forces during boron carburizing of steel 45 throughout the simulated range. The same effect of viscosity occurs during boriding steel 45, but in the range from 0.11 to 0.2 Pa s, however, the increase in values occurs with greater intensity.

The obtained and described results on the parameter $\tau_0$ generally indicate the ambiguity and peculiarity of the manifestation of adhesion between the studied surfaces of steels, activated for interaction by the supply of external mechanical energy of high mechanical pressures, excess surface energies due to the introduction of additional chemical elements during the modification of steel 45 and components of the used lubricating media. At the same time, it should be noted the effect of a short-term structural change in liquid lubricants on the contour contact areas during their compression, since the design pressures are sufficiently high. The pressures in the zone of frictional interaction ranged from 80 MPa to 260 MPa. Due to the complexity and versatility of the components of these processes and the limited information on their course, this issue is not discussed in the work and remains open.

Thirdly, the parameter $\beta$ has a simpler and rather informative calculated manifestation. For a more visual assessment, graphical approximations of the trends in the change in the piezoelectric coefficient in the considered systems of materials when modeling the shear rate in the range of dynamic viscosity of liquid lubricants are shown in Figs. 3, 4. The analysis of the presented dependencies in Fig. 3, 4 indicates the following. First, the absence of modification of steel 45 with boron and boron carbide predetermines the independence of the piezoelectric coefficient from the viscosity of the liquid lubricant and the shear rate.
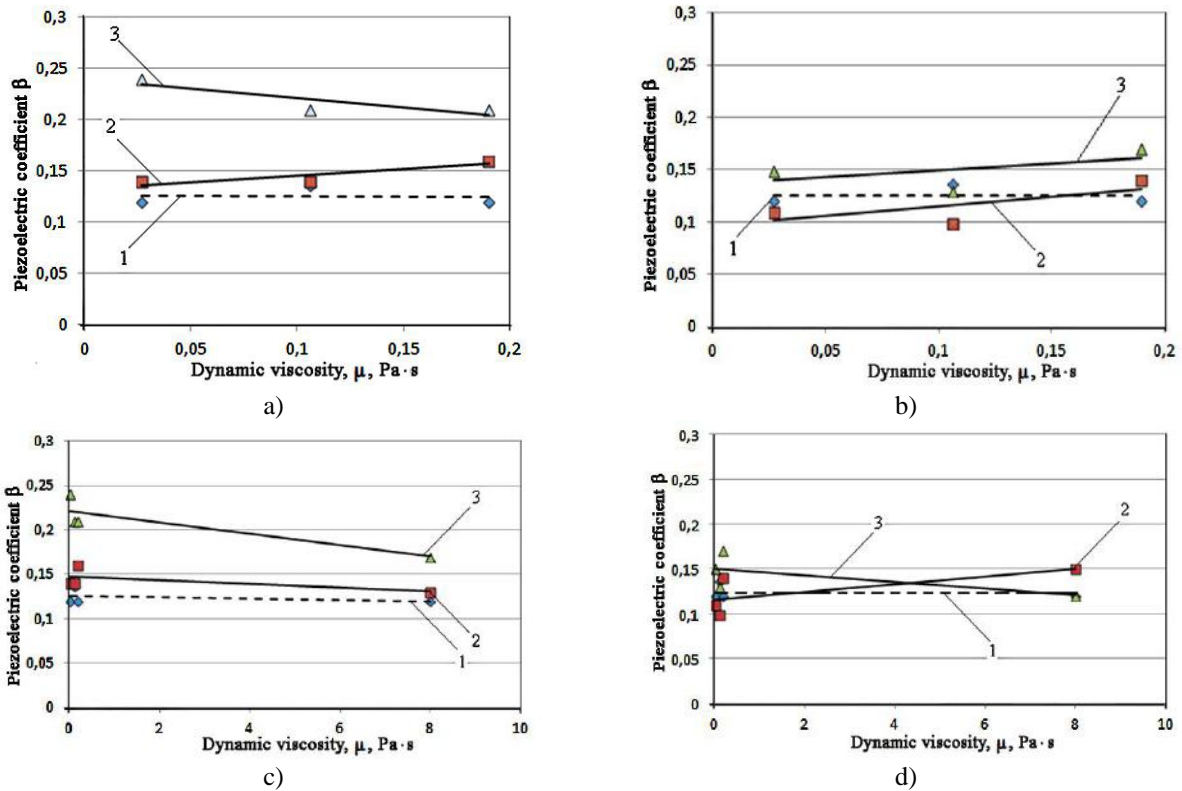
**Fig.3.** Influence of dynamic viscosity in the range of liquid (a, b) lubricant and taking into account the range of consistent state (c, d) on the change in the piezoelectric coefficient of adhesive bond in the material system "45KhN2MFA - steel 45": a, b - at = 5.08 ± 0.6 mm/s; b, d - at = 10.16 ± 0.8 mm/s; 1 - steel 45 is not modified; 2 - "steel 45 + BC"; 3 - "steel 45 + B".
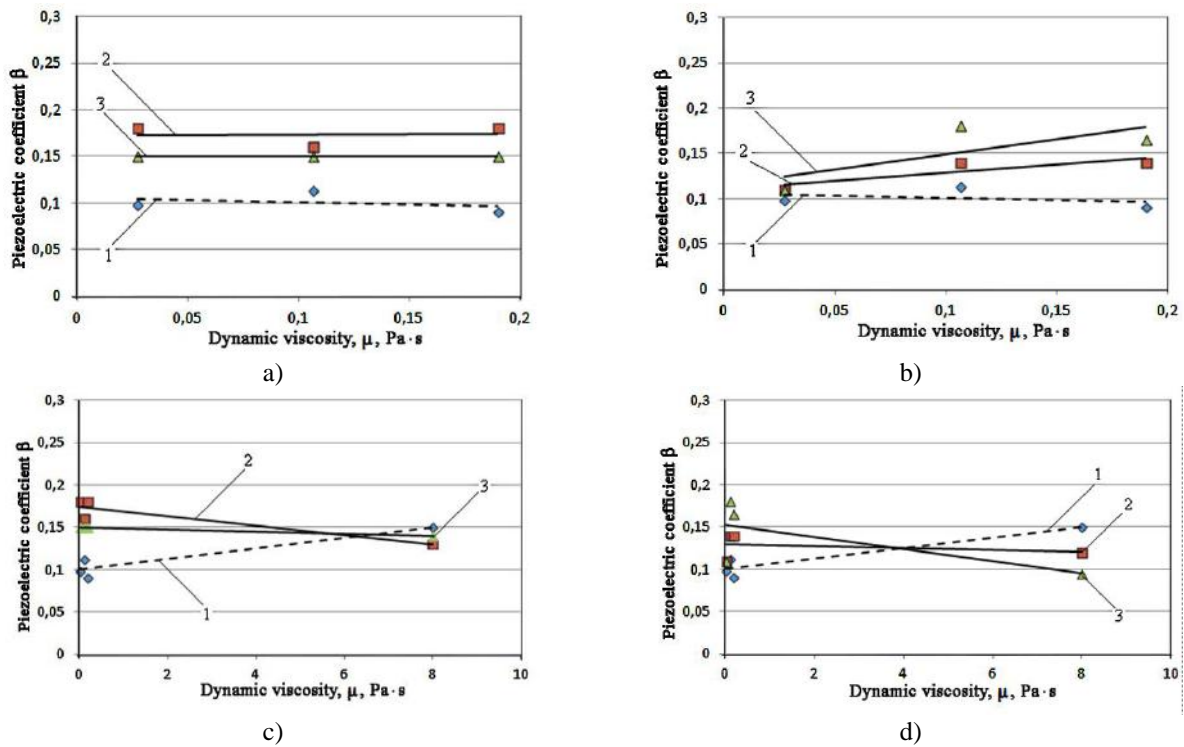


**Fig.4.** Influence of dynamic viscosity in the range of liquid (a, b) lubricant and taking into account the range of the consistent state (c, d) on the change in the piezoelectric coefficient of adhesive bond in the material system "12Kh2H2 - steel 45": a, b - at = 5.08 ± 0.6 mm/s; b, d - at = 10.16 ± 0.8 mm/s; 1 - steel 45 is not modified; 2 - "steel 45 + BC"; 3 - "steel 45 + B"

In the simulated ranges of viscosity and shear rate, the increment of the piezoelectric coefficient values is zero. The exception is the system "12Kh2H2 - steel 45". For this system of metals with the transition to a grease lubricant, the rate of increase in the piezoelectric coefficient is 0.0064 $(Pa \cdot s)^{-1}$.

At the same time, the average statistical values of the piezoelectric coefficient are: for the system "12Kh2H2 - steel 45" in the viscosity range from 0.001 Pa • s to 0.2 Pa•s $\beta = 0.1 \pm 0.003$, for the system "45KhN2MFA - steel 45" $\beta = 0,12 \pm 0.003$. From which it seems obvious that the intensity of the increase in the strength of the adhesive bond in the system "45KhN2MFA - steel 45" is 1.2 times higher.

For the system "12Kh2H2 - steel 45 + B (BC)" with a shift of $5.08 \pm 0.6$ mm/s, the rate of decrease of the piezoelectric coefficient is 0.005 $(Pa•s)^{-1}$. From which it follows that modification with boron and boron carbide predetermines a less intense increase in the strength of the adhesive bond of the investigated metal surfaces.

## Conclusion

The results obtained in the work revealed the features of the manifestation of the adhesive bond parameters in the investigated metal systems when simulating changes in dynamic viscosity in the range from 0.027 Pa•s to 8 Pa•s.

The constructed graphic patterns and the parameters of their mathematical approximation made it possible to determine the direction of the processes of adhesive interaction of the surface of 45 steel modified with boron and boron carbide with steels 12Kh2N2, 45KhN2MFA through lubricating formations compacted by contact pressure with distinctive gradients of dynamic viscosity.

It has been established that the boriding and boron cementation of steel 45 predetermines the expansion of the range of working normal pressures in lubricating media, excluding the manifestation of the adhesive friction component, and in contact with steel 45KhN2MFA upwards.

The data obtained can be used, firstly, as reference values of the adhesive bond parameters to substantiate the possibilities of increasing the reliability of the operation of friction pairs during shear, and secondly, when calculating the service life of a gear pair, in which the gears will be made from the studied systems of materials.

The direction of further research is proposed to consider the study of the nature of the relationship between the manifestation of the established parameters $\tau_0$ and $\beta$ and the surface energies of the contacting surfaces of the metal systems under consideration.

## REFERENCES

1   Cherneta O.G., Kubich V.I., Voloshchuk R.G, Averyanov V.S., Shmatko D.Z. Strengthening of the Restored Surface Layer of Steel Parts 45 by Laser Boring. *International Journal of Engineering & Technology (UAE)*. Science Publishing Corporation, RAK Free Trade Zone. 2018, Vol 7, No 4.3, pp.71-75.

2   Sitkevich M.V., Pishchov M.N., Belsky S.E. The influence of complex boride hardening on the structure and properties of the surface layers of steels for the manufacture of gear parts for skidding forest machines. *Casting and metallurgy*. 2008, no. 4(49), pp.140-146.

3   Cherneta O.G., Kubich V.I., Shcherbina M.A., Averyanov V.S., Shmatko D.Z. Research of steel 45 strugging influence on the parameters of adhesion communication with chrome, chrome-nickel steel. *Mathematical modeling*. Kamiansk. DDTU. 2019, No. 2 (41), pp.150-158.

4   Kubich V.I., Cherneta O.G., Yurov V.M. Influence of borination, borocement of steel 45 and viscosity of a lubricant on the parameters of adhesion bond in the steel 45-40X system. *Eurasian phys. tech. j.* 2021, Vol 18, No2(36), pp. 67-75.

5   Semenov V.I., Shuster L.Sh., Chertovskikh S.V., et al. Influence of the complex parameter of plastic frictional contact and material structure on the strength of adhesive bonds. *Friction and Wear*. 2005, Vol. 26, No. 1, pp.74-79.

6   Yurov V.M., Eremin E.N., Guchenko S.A. Application of high entropy coatings simultaneous in one cycle spraying three cathodes. *Bulletin of KarSU. Physics*. 2020, No. 1(97), pp. 7-17.

7   Kubich V.I., Cherneta O.G., Yurov V.M.  Potential difference of metal machine parts methodology for determining the parameters of adhesional properties of materials on the SMC-2 friction machine. *Eurasian Physical Technical Journa*l. 2019, Vol.16, No. 2(32). – pp. 78-82.

8   Bogdanova Yu.G. *Adhesion and its role in ensuring the strength of polymer composites*. – Moscow, MGU. 2010. http://nano.msu.ru/files/master/I/materials/adhesion.pdf

# OBTAINING OF CALCIUM-PHOSPHATE COATINGS ON THE TITANIUM SURFACE BY MICRO-ARC OXIDATION

Baizhan D.R.[1,3], Rakhadilov B.K.[2], Aldabergenova T.M.[3], Bayatanova L.B.[2,4],
Kurbanbekov Sh.R.[5], Buitkenov D.B.[1]

[1]S. Amanzholov East-Kazakhstan University, Ust-Kamenogorsk, Kazakhstan daryn.baizhan@mail.ru
[2]LPP «PlasmaScience», Ust-Kamenogorsk, Kazakhstan
[3]Shakarim University, Semey, Kazakhstan
[4]D. Serikbayev East-Kazakhstan Technical University, Ust-Kamenogorsk, Kazakhstan
[5]Ahmed Yasawi University, Turkestan, Kazakhstan

*The results of experiments on obtaining calcium-phosphate coatings on substrates of titanium grade VT1-0 by micro-arc oxidation (MAO) are presented. The coatings were obtained by adding different amounts of titanium oxide nanoparticles to the electrolyte. The microstructure and tribological properties of calcium phosphate coatings were investigated. In conducted research results have been established and determined optimal modes and parameters for obtaining calcium phosphate coatings. It is shown that the addition of titanium oxide nanoparticles to the electrolyte can affect the structure also the strength of the obtained coatings. The research results led to conclude that such treatment of MAO from titanium alloys is promising to improve their splices with bone tissue.*

## Introduction

For the date a wide range of developed and tested methods are used to create calcium phosphate (CF) coatings on metal implants: plasma spraying process, micro-arc oxidation, methods based on crystallization of coatings from various solutions, detonation-gas spraying method, electrochemical deposition, sol-gel processes, etc. Each of these methods has its advantages and disadvantages. Among the disadvantages, the following can be noted: poor adhesion of coatings to the substrate, the inability to regulate their elemental composition, restrictions in the choice of substrate material for coating formation. Studies have shown that the use of the micro-arc oxidation (MAO) method, namely the plasma electrolytic oxidation (PEO) method, provides high adhesion strength between the substrate and the coating [1-3].

The MAO method in aqueous solutions of electrolytes has become widespread in the last decade as a method of applying bioactive CF coatings to the surface of titanium [4]. The coating formation in a micro-arc discharge is associated with the course of high-temperature chemical processes in the zone of local micro-plasma and micro-arc discharges under the influence of an external high voltage source and is associated with the oxidation of the base material, as well as the transition of the ultrafine phase in the electrolyte into the coating. The coatings obtained by this method have a good complex of physicochemical properties: high corrosion resistance, wear resistance, hardness and chemical resistance in aggressive environments [5].

If evaluate the current state of the scientific or scientific-technological problem being solved, then in the last decade in the field of biomaterial development there have been directions for creating materials that ensure the formation of a transition zone between bone and implant [6]. Such area should have a strong connection with the implant material, also macro- and microstructure suitable for the body, as well as bioavailability. Structural materials such as stainless steel, cobalt- and titanium-based alloys are widely used to create artificial implants due to their excellent mechanical properties, however, in some cases they cause allergic reactions and, as a result, out of order. In addition, a violation of the splices of the surface of the endoprosthesis with bone tissue leads to its gradual loosening, which requires repeated operations to replace or strengthen the implant. To increase the bioavailability of these materials, additional coatings are applied to their surface. Recently, there has been an increased interest in coatings made of CF and hydroxyapatite

$Ca_{10}(PO_4)_6(OH)_2$ (HA), which significantly increase the adhesion of implants to bone tissue [7]. The solution of the problem of increasing the bioavailability and osseointegration of implants in orthopedics and surgery is of very important social importance, since at present the rejection of implants in the postoperative period, cases requiring repeated implantation operations, the development of allergic reactions, a high probability of relaxation can lead to a long recovery of the patient. Coating the implant surface close to HA with titanium oxide nanoparticles provides not only high bioavailability, also develops osseointegration [6].

The purpose of this work is to study the effect of PEO on the microstructure, roughness, tribological characteristics of calcium phosphate coatings with the addition of titanium oxide nanoparticles.

## 1. Materials and research methods

Technically pure titanium material VT1-0 which often used in medicine, was used as a substrate. Samples of technical titanium VT1-0 for research were cut from rods in the state of delivery in the form of parallelepipeds. Previously, the samples were grinded to remove the oxide film and scratches. Table 1 shows the chemical composition of technically pure titanium VT1- 0. In comparison with other metals used as implants, pure titanium has a number of advantages: good corrosion resistance due to the formation of a passive oxide layer on the surface; high bioavailability; bio-inertia; practically non-toxic; low thermal conductivity; low coefficient of linear expansion; relatively low density compared to steel [8].

**Table 1.** Chemical composition of technically pure titanium VT1-0 (wt.).

| Fe | C | Si | N | Ti | O | H |
|------|------|-----|------|------|-----|------|
| 0. 25 | 0. 07 | 0. 1 | 0. 04 | 99. 7 | 0. 2 | 0. 01 |

To obtain calcium-phosphate coatings by the PEO method, an experimental-industrial MAO installation was used, which consists of a power source, an electrolytic bath with a cooling system and electrodes. The pilot-industrial installation for PEO was developed and manufactured in the research and production company PlasmaScience LLP (Kazakhstan, Ust-Kamenogorsk). Equipped with APS-77300 AC power supply. This equipment makes it possible to apply calcium phosphate coatings to medical implants, changing the coating modes on a large scale and thereby allowing for research. By controlling the parameters of the MAO, the installation allows to simultaneously cover several products (with a total area of more than 200 $cm^2$) due to high power in one cycle.

APS-77300 power supply unit output power: 3000 VA, voltage: up to 600 V, current: up to 25.2 A. Wide range of output voltage settings (amplitude, frequency, initial and final phases). Frequency range: 999.9 Hz. Discrete setting of output parameters in increments of 0.01 V / 0.01 Hz. Low harmonic coefficient (0.5%).

Calcium-phosphate coating was carried out in the anode-potentiostatic mode. The parameters of the PEO process included the following limits: pulse duration - 100-500 µs, pulse frequency - 50-100 Hz, initial current density - 0.13-0.35 $A/cm^2$, process duration - 5-20 min, electrical voltage - 50-100 V. The scheme of the MAO device is shown in Figure 1.
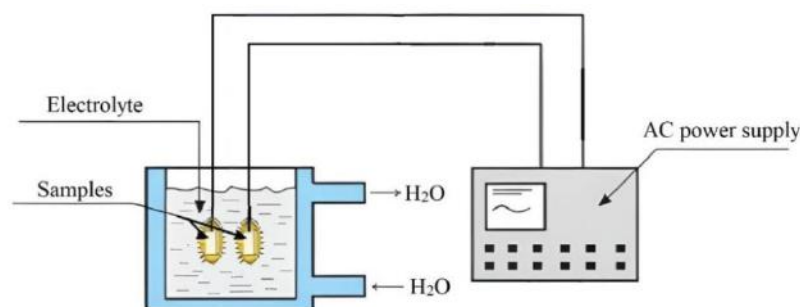


**Fig. 1** - Scheme of the MAO device.

Various acid, salt and alkaline electrolytes can be used for micro-arc machining of titanium and titanium alloys parts. The most common electrolyte for MAO-titanium is a mixed phosphate-alkaline electrolyte of the $KOH-Na_3PO_4$ type. In this composition, KOH is an activator that affects the enrichment capacity, which makes it possible to form a strengthening layer on the oxidized surface in relation to the nominal amount of the part; this leads to a significant increase in the adhesive strength of the coatings [9].

Three different electrolytes were obtained by adding 500 g of distilled water, 10g of phosphoric acid $H_3PO_4$, 5g of hydroxyapatite $Ca_{10}(PO_4)_6(OH)_2$, 0.5g/0.75g/1g of titanium oxide $TiO_2$. The parameters of the MAO process during exploitation include the following limits: pulse duration - 100 μs, pulse frequency - 100 Hz, electrical voltage - 100V, initial current density - 0.15-0.35 $A/cm^2$, process duration - 10min. When applying a calcium-phosphate coating with titanium oxide nanoparticles, titanium samples attached to the suspension were immersed in an electrolyte in a bath. The MAO was carried out in the anode mode at AC voltage of 100V for 10 minutes. As a result of the experiment, local micro-plasma discharges appeared on the surface of the samples, and a coating was synthesized in their area. To obtain a calcium-phosphate coating on samples of technical titanium grade VT1- 0, which underwent the PEO process, three different amounts of titanium oxide were introduced into the electrolyte.

Microstructural analysis was performed on an ALTAMI-MET-5Smicroscope. To improve the image quality in the microscope, an advanced lighting system with a powerful lamp (12V, 50W) is used as a light source. The basic equipment of ALTAMI -MET-5S is equipped with a digital USB camera with a resolution of 3 MP and Altami Studio software.

Tribological friction tests were carried out according to the standard "ball-disc" technique on the Anton Paar TRB[3] tribometer (international standards ASTM G 133-95 and ASTM G 99). As a counter wire, a ball with a diameter of 3.0 mm was used, certified material - $Al_2O_3$. The tests were carried out at a load of 1N and a linear velocity of 2cm/s, a wear curve radius of 3mm, a friction path of 40m. The tribological characteristics of the modified layer were characterized by the intensity of wear and friction coefficient.

The surface roughness was measured with a model 130 profilometer. The action of the profilometer is based on the principle of perception of the roughness of the measured surface by the probe of an inductive sensor - in the process of control by a diamond needle (moving the sensor along the measured surface at a constant speed), which converts the translation of the sensor into an analog-digital signal and further digital signal processing.

## 2. Research results

To find out the effect of electrolytes on the calcium-phosphate coating with titanium oxide nanoparticles from the MAO process, an electrolyte of three different compositions was prepared (Table 2). The calcium phosphate coating with titanium oxide nanoparticles was obtained using distilled water, orthophosphoric acid, hydroxyapatite and three different grams of titanium oxide.

**Table 2**. Limits of the MAO process for each electrolyte.

| Electrolyte | 0.5g $TiO_2$ + 500g dist.water + 10g $H_3PO_4$ + 5g HA: No1 | 0.75g $TiO_2$ + 500 500g dist.water + 10g $H_3PO_4$ + 5g HA: No2 | 1g $TiO_2$ + 500g dist.water + 10g $H_3PO_4$ + 5g HA:No3 |
|---|---|---|---|
| Frequency (Hz) | 100 Hz | 100 Hz | 100 Hz |
| Voltage (V) | 100 V | 100 V | 100 V |
| Impulse (μs) | 100 μs | 100 μs | 100 μs |
| Time (min) | 10 min | 10 min | 10 min |

The MAO process affects the structural characteristics and mechanical properties of titanium VT1-0 not only surface, but also deeply located structural elements. The nature of structural changes and changes in mechanical characteristics depends on the chemical composition of the alloy [9]. The microstructure, roughness, and tribological characteristics of VT1-0 titanium with a calcium phosphate coating with the addition of titanium oxide nanoparticles after the MAO process were studied. Figure 2 shows the initial microstructure of titanium VT1-0.  The initial dimensions of the VT1-0 titanium microstructure were assumed to be 70μm, 100μm and 300μm.

In the initial state (in the state of delivery), titanium grade VT1-0 has a partially recrystallized structure (Fig. 2), with an average size of the elements of the grain-subgrain mixture d = 4.7μm, while the size of the recrystallized grains in such a material is ~ 10μm. As a result of local high-energy exposure, layers were formed on the surface of the samples, including both matrix elements (oxidized metal) and electrolyte elements [8]. When the anode current lasts 100 μs, dense uniform oxide coatings are formed in all electrolyte solutions. The thickness of the oxide coatings was 30-60 μm.



a)                                    b)                                    c)
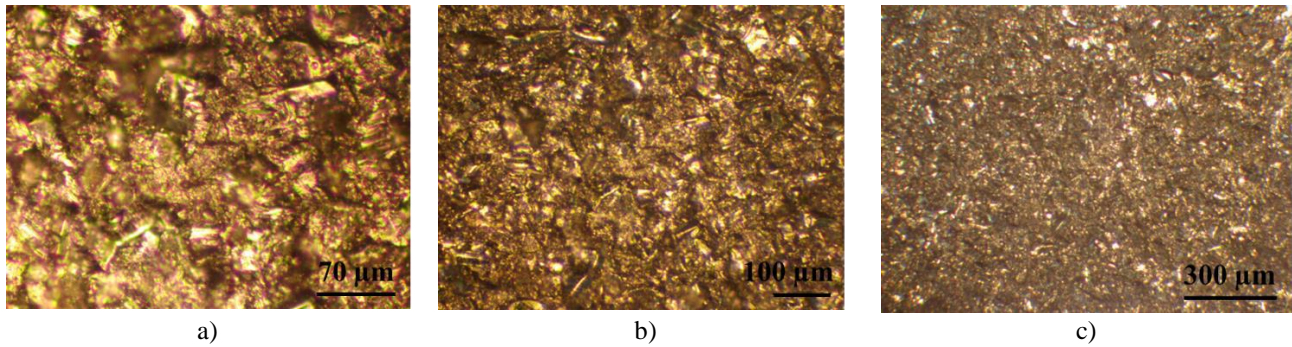
**Fig.2.** Microstructure of VT1-0 titanium in its initial state.



a)                                    b)                                    c)
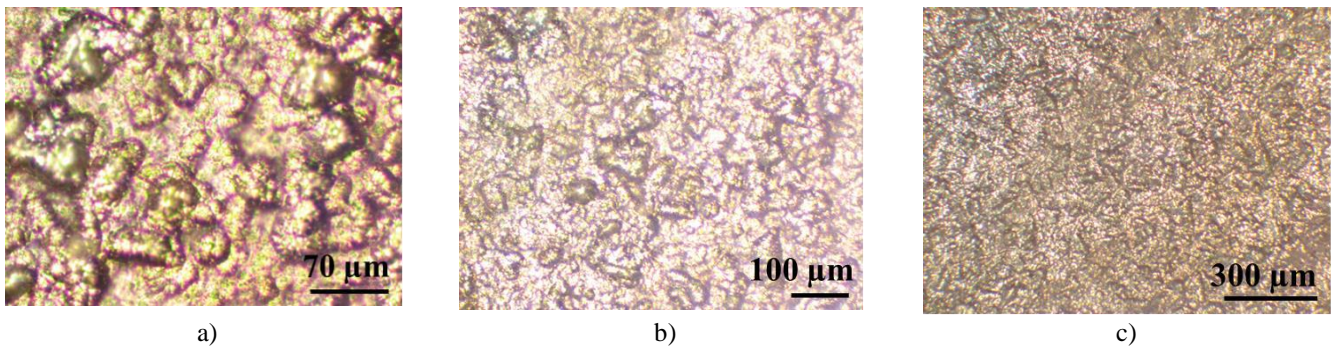
**Fig. 3.** Microstructure of titanium VT1-0 in a calcium phosphate coating with 0.5g of titanium oxide.

The microstructure of the calcium phosphate coating obtained in the presence of 0.75 nanoparticles of titanium oxide, orthophosphoric acid and hydroxyapatite in the electrolyte is shown in Fig. 4. The study of the structure of coatings formed during PEO on the surface of titanium with different electrolyte compositions shows that they have a common nature. In particular, when treated in such electrolytes, a coating with a developed porous structure and glassy bubbles is formed in the voltage range (Fig. 4.).



a)                                    b)                                    c)
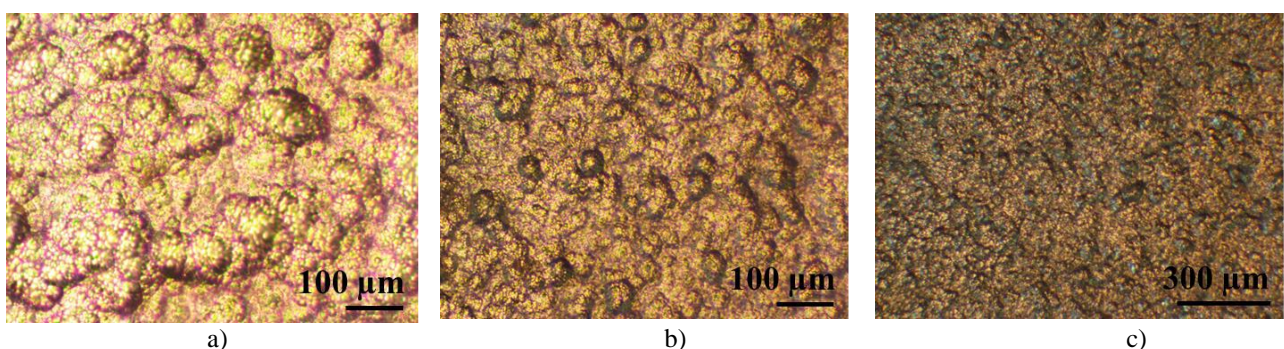
**Fig. 4.** Microstructure of titanium VT1-0 in a calcium phosphate coating with 0.75 g of titanium oxide.

The microstructure of the calcium phosphate coating obtained in the presence of nanoparticles of titanium oxide 1, orthophosphoric acid and hydroxyapatite in the electrolyte is shown in Fig.5.

Microstructural analysis showed that with this electrolyte composition and the corresponding PEO treatment mode, titanium dioxide is intensively formed on the surface of titanium samples, forming a sufficiently dense layer. The results of optical microscopy of calcium-phosphate coatings formed in the

electrolytes, the composition of which is given above, indicate that at these oxidation stresses they have small aggregates with a discontinuous loose structure.

At these voltages, developed loose aggregates are formed, similar to a spongy structure, formed by randomly arranged glassy bubbles. High porosity is observed in all samples. The presence of pores is favorable for the ingrowth of bone tissue in them and the formation of a stronger connection of the implant with the bone [4]. In order to confirm and coordinate the obtained optical microscopy data, it is necessary to additionally conduct scanning electron microscopy studies and X-ray spectral analysis, the results of which are planned to be published by the authors in the following papers.



a)                                      b)                                      c)
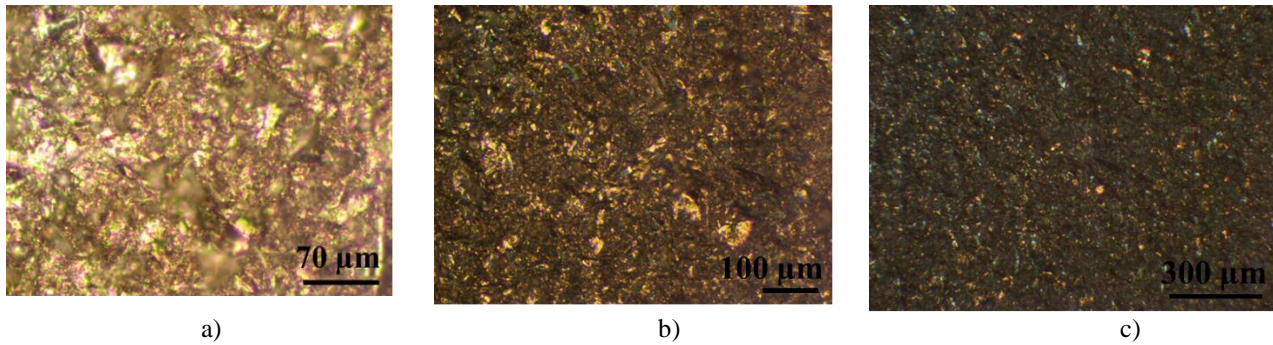
**Fig. 5.** Microstructure of titanium VT1-0 in a calcium phosphate coating with 1g of titanium oxide.

Thus, titanium PEO with the addition of titanium oxide nanoparticles is promising from the point of view of obtaining biocompatible coatings, the coatings obtained in this case have a developed surface, which will serve their improved fusion with bone tissue. A positive feature of this processing method is the high rate of film formation and, accordingly, the low energy intensity of the process [10]. The roughness of the investigated surface of titanium VT1-0 was measured at small permissible areas, so the baseline lines were selected considering the parameter of reducing the influence of the undulating state of the surface on the change in altitude parameters. The contours of the profile were obtained during control using a diamond needle, and the trace was recorded on a profilogram. Figure 6 shows the roughness of the surface of titanium VT1-0 in its initial state.



$R_a = 4.11$ μm
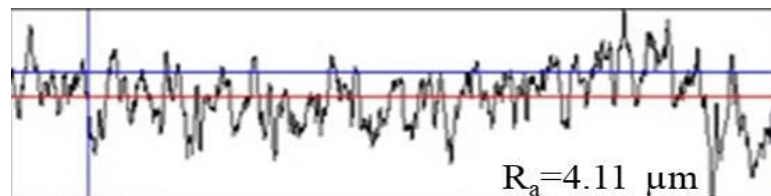
**Fig. 6**. Indicators for measuring the roughness of titanium VT1-0 in the initial state.

The surface roughness of the PEO coating is created by pores and irregularities in the form of meltdowns, which are formed during micro-plasma breakdown, as shown above (Fig.3-5). As the results of the study of surface roughness before and after processing have shown, the surface roughness of PEO coatings changing. Figure 7 shows the roughness of titanium VT1-0 with a calcium phosphate coating after the MAO process with the addition of 0.5g of titanium oxide nanoparticles to the electrolyte.



$R_a = 1.31$ μm
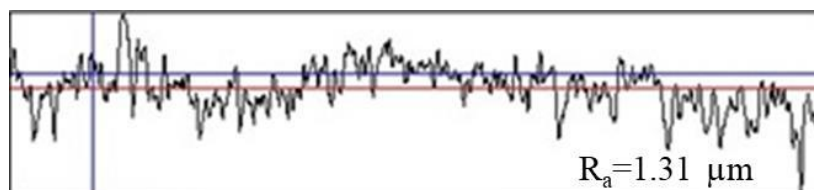
**Fig. 7**. Indicators for measuring the roughness of titanium VT1-0 in a calcium-phosphate coating with 0.5g of titanium oxide.

The roughness of titanium VT1-0 with a calcium phosphate coating obtained by the MAO method with the addition of 0.75g of titanium oxide nanoparticles to the electrolyte is shown in Figure 8. There is a direct relationship that determines the characteristics of the treated surface, the higher the class index, the lower the height of the measured surface and the better the quality of processing.
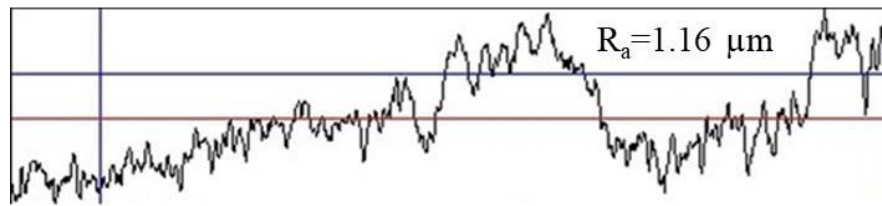


**Fig. 8.** Indicators for measuring the roughness of titanium VT1-0 in a calcium-phosphate coating with 0.75g of titanium oxide.

Figure 9 shows the roughness of titanium VT1-0 with a calcium phosphate coating after the MAO process with the addition of 1g of titanium oxide nanoparticles to the electrolyte.
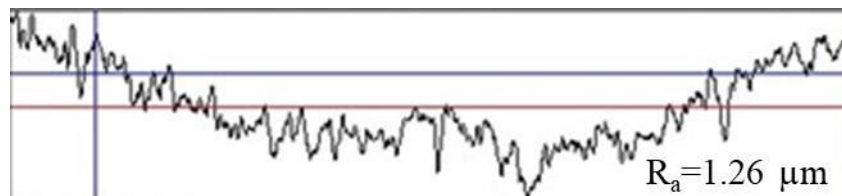


**Fig. 9.** Measurement values of titanium roughness VT1-0 on a calcium phosphate coating with 1g of titanium oxide.

The arithmetic mean deviation of roughness in the initial state was 0.0589 μm. The arithmetic mean deviation of titanium VT1-0 in a calcium phosphate coating with the addition of 0.5g of titanium oxide nanoparticles to the electrolyte after MAO is 1.456 μm, with 0.75g of titanium oxide nanoparticles is 1.223 μm, with 1g of titanium oxide nanoparticles is 1.253μm.

After the experiment, the value of the arithmetic mean deviation of roughness increased. The correct use of the method for determining the roughness of surfaces allows to achieve high processing accuracy, and the particle size allows to significantly improve the quality of the finished product. The smaller the roughness, the less corrosion and the higher the accuracy of the installation of parts during assembly [11].

During tribological tests, curves of change in the friction coefficient, data on the widths of the wear tracks were obtained. Coated samples were tested. Fig. 10-12 shows images of the type of wear strip with measurements of its width of the surfaces of samples with a track and shows the corresponding curves of the friction coefficients for the VT1-0 alloy with a coating obtained in solutions of electrolytes No.1, 2, 3.
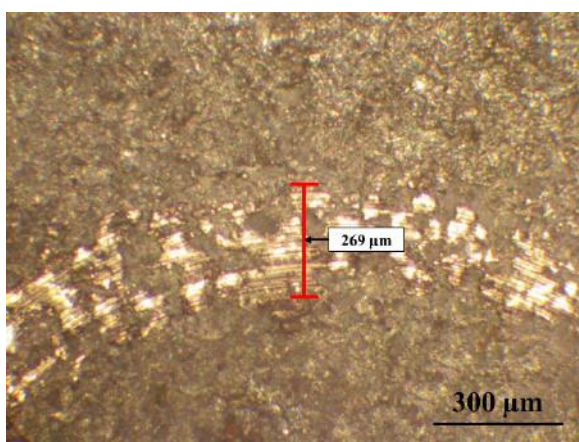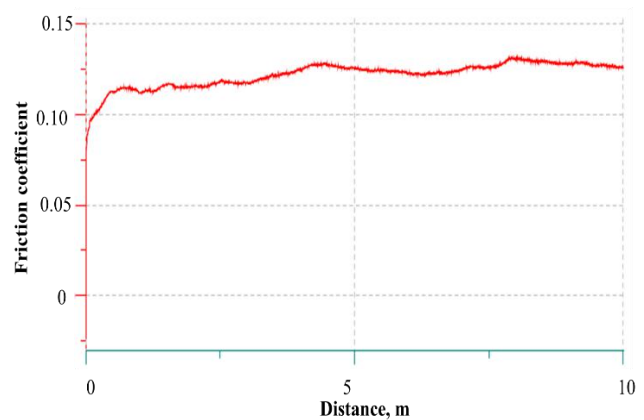


a)                                              b)

**Fig. 10.** Microstructural image of wear marks (a) and profilogram of titanium VT1-0 (b) on a calcium phosphate coating with 0.5g of titanium oxide as an electrolyte.

On the curves of the coefficient of friction of coatings, there are zones of tribosystem run-ins, where the rubbing surfaces adapt to each other and are accompanied by a high degree of wear. The stages are also visible, which are characterized by stable friction conditions and almost constant and relatively low wear intensity. There is no sharp change in the coefficient of friction characteristic of the destruction of the coating. Oxide coatings do not break down and do not wear down to the base. The length of the wear trace of titanium VT1-0 on a calcium phosphate coating containing 0.5g of titanium oxide nanoparticles in an electrolyte obtained by the MAO method is 269 µm.



a)                                              b)
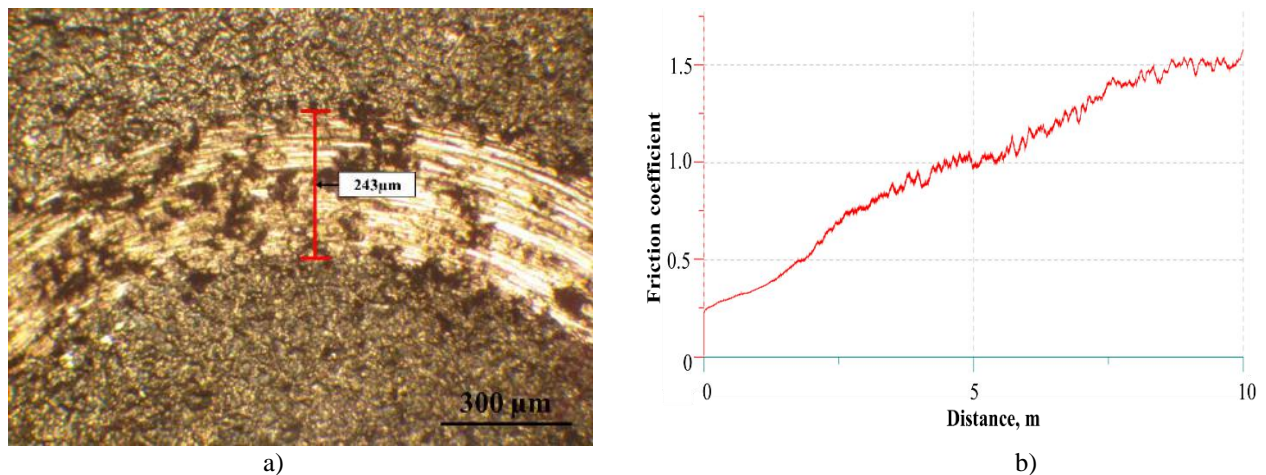
**Fig. 11.** Microstructural image of wear marks (a) and profilogram of titanium VT1- 0 (b) on a calcium phosphate coating with 0.75g of titanium oxide as an electrolyte

The length of the wear trace of titanium VT1-0 on a calcium phosphate coating containing 0.75 g of titanium oxide nanoparticles in an electrolyte obtained by the MAO method is 343 µm.



a)                                              b)
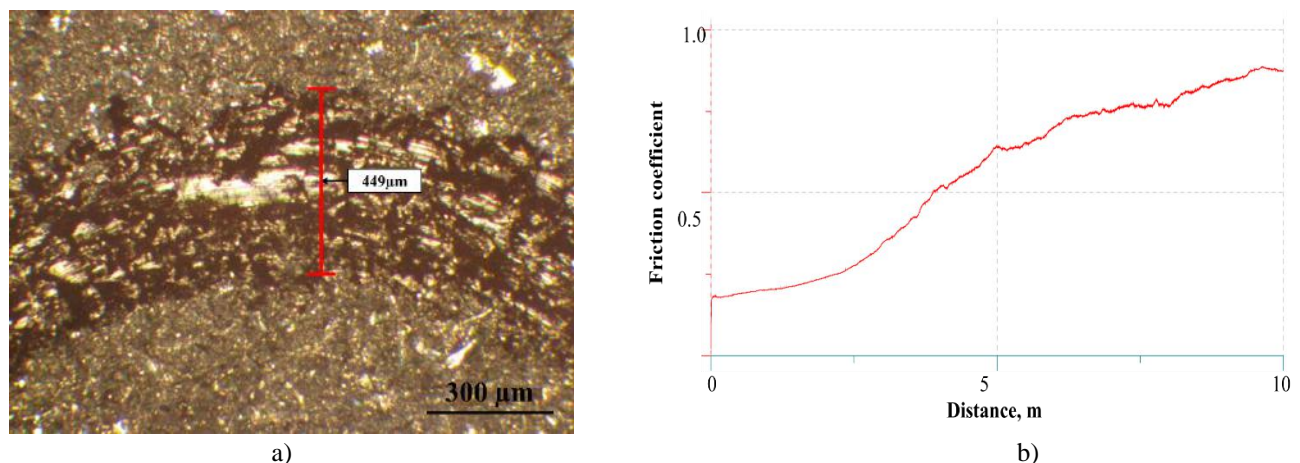
**Fig. 12.** Microstructural image of wear marks (a) and profilogram of titanium VT1- 0 (a) on a calcium phosphate coating with 1g of titanium oxide as an electrolyte

The length of the wear trace of titanium VT1-0 on a calcium-phosphate coating containing 1g of titanium oxide nanoparticles in an electrolyte obtained by the MAO method is 449µm. When the length of the wear marks is longer, the wear resistance becomes worse. After testing, it was found that titanium VT1-0 in a calcium-phosphate coating obtained by adding 0.5g of titanium oxide to the electrolyte has increased wear resistance. During tribological tests, the process of running in the product/counter body pair occurs, the rubbing surfaces adapt to each other. Then comes the stage of steady wear, which has the longest duration. It is characterized by stable friction conditions and almost constant and relatively low wear intensity [12]. During its development, wear gradually increases, which is accompanied by damage to the surface.

**Conclusion**

The study of the structure of coatings formed during PEO on the surface of titanium with different electrolyte compositions showed that they have a common nature. As a result of this MAO mode, a coating with a developed porous structure and glassy bubbles is formed. The presence of pores is favorable for the ingrowth of bone tissue in them and the formation of a stronger connection of the implant with the bone.

As the results of the study of surface roughness before and after processing have shown, the surface roughness of PEO coatings changing. After the experiment, the value of the arithmetic mean deviation of roughness decreased by 4 times compared to the initial state. After the conducted studies, it was found that the use of the addition of $TiO_2$ nanoparticles to the electrolyte can significantly improve the tribological characteristics of the oxide layers formed during the MAO of titanium alloys.

Studies of the wear resistance of oxide coatings have shown a significant increase in it compared to the uncoated sample. The oxide coating obtained in different electrolyte compositions increases wear resistance compared to the uncoated sample. It is shown that the introduction of titanium oxide nanoparticles into the electrolyte makes it possible to obtain wear-resistant coatings. This is probably due to the introduction of titanium oxide into the coating, which is formed under the influence of high temperatures during micro-arc discharge.

Thus, titanium PEO with the addition of titanium oxide nanoparticles is promising from the point of view of obtaining biocompatible coatings, the coatings obtained in this case have a developed surface, which will serve their improved fusion with bone tissue. A positive feature of this processing method is the high rate of film formation and, accordingly, the low energy intensity of the process.

**Acknowledgments**

**REFERENCES**

1    Suminov I.V., et al. *Microarc oxidation: theory, technology, equipment*. Moscow, 2005, 368 p. [in Russian].

2    Chernenko V.I., et al. Obtaining of coatings by anodic-spark electrolysis. *Chemistry*. 1991, 128 p. [in Russian]

3    Shandrov B.V., et al. *Fundamentals of micro-arc oxidation technology*. Moscow, 2008, 80 p. [in Russian]

4    Rakhadilov B., Baizhan D., Creation of Bioceramic Coatings on the Surface of Ti–6Al–4V Alloy by Plasma Electrolytic Oxidation Followed by Gas Detonation Spraying. *Coatings*. 2021. 11, No. 1433, doi:10.3390/coatings11121433

5    Sharkeev Yu. P., E. V. Legostaeva, A. Yu. Eroshenko, I. A. Khlusov, O. A. Kashin, The Structure and Physical and Mechanical Properties of a Novel Biocomposite Material, Nanostructured Titanium-Calcium-Phosphate Coating. *Composite Interfaces*. 2009, Vol.16, pp. 535 – 546.

6    Rakhadilov, B.K., Sagdoldina, Z.B., Baizhan, D.R., et al. Obtaining of hydroxyapatite coatings on A titanium substrate by detonation-gas spraying. *Eurasian phys. tech. j*. 2021, Vol.18, pp. 30 – 36.

7    Ivanov M.B., Kolobov Yu.R., Golosov E.V., et al. Mechanical properties of mass-produced nanostructured titanium. *Russian nanotechnology*. 2011, Vol.6, No.5-6, pp. 108 – 114. [in Russian]

8    Gnedenkov S.V., Sharkeyev Y.P., Sinebryukhov S.L., et al. Calcium-phosphate bioactive coatings on titanium. *Bulletin of FEB RAS*, 2010, Vol.5, pp. 47 – 57. [in Russian]

9    Suminov I. V., Belkin P. N., Epelfeld A. V., et al. *Plasma-electrolytic modification of surfaces of metals and alloys*. Part. 2. Moscow, Technosphere Publisher, 2011, 512 p. [in Russian]

10    Shashkina G. A. *Calcium-phosphate coating by micro-arc method. Structure and properties of biocomposite based on titanium with calcium-phosphate coatings*. Diss. of the candidate of technical sciences degree. Tomsk, 2006, 184 p. [in Russian]

11    Lyubimov V.V., Sundukov V.K., Gavrilin V.I. Effect of micro-arc oxidation modes on the roughness and wear resistance of coatings. *Proceedings of the scientific and technical conference "Modern electrotechnology in industry of Central Russi".* Tula State University, 2003. 126-130. [in Russian]

12    Chichinadze A.V., et al. *Friction, Wear and Lubrication (Tribology and Tribotechnics)*. Moscow: Machinostroenie, 2003, 576 p. [in Russian]

.

# PERFORMANCE IMPROVEMENT OF SOLAR DRYER USING AN AUXILIARY HEAT SOURCE UNDER DIFFERENT VALUES OF AIRFLOW RATES

Alkahdery L.A.[1], Yurchenko A.V.[2], Mohammed J.A.-K.[3], Mekhtiyev A.D.[4], Neshina Y.G.[5*]

[1] National Research Tomsk Polytechnic University, Tomsk, Russia
[2] National Research Tomsk State University, Tomsk, Russia
[3] Electromechanical Engineering Dept., University of Technology, Baghdad, Iraq
[4] S. Seifullin Kazakh Agrotechnical University, Astana, Kazakhstan
[5] A. Saginov Karaganda Technical University, Karaganda, Kazakhstan, 1_neg@mail.ru

*One of the most crucial methods for preserving agricultural produce is solar drying. The major focus of this paper is increasing solar drying systems' effectiveness. The development of new methods and variables that may have an impact on the functionality of solar dryers aids in enhancing their efficiency. An indirect-type solar dryer for drying agricultural products is proposed and developed in this study. A dryer consisting of a solar flat plate air collector, an insulated drying chamber, an auxiliary (electric) heat source, and an electric fan is constructed to improve the dryer's performance. The dryer's most typical function is to blow hot air at the product, forcing the water in it to evaporate. The effect of air temperature and velocity on evaporation rate has been studied experimentally. Tests with three different airflow rates—0.042, 0.0735, and 0.105 m³/s—are conducted. When there is little or no solar radiation, an auxiliary heater is used to provide sufficient heat. For varying airflow rates, solar mode and electrical mode were tested experimentally with only one energy source in each mode. The findings revealed that using a different heat source in addition to solar radiation will allow you to keep the air temperature in the drying chamber between 32 ºC and 42ºC. Also, it was found that for the whole drying process at high air velocities, the temperature had less influence on the dryer's performance.*

***Keywords:*** Solar dryer; auxiliary heat source; moisture content; solar air collector; airflow rate, PCB.

## Introduction

The solar dryer enters many applications and the most important one is the food applications [1]. Drying is said to be the earliest method of preserving agricultural produce. The moisture content is lowered to its saturation level using this procedure. A heated air stream is blown across the product, either naturally or artificially, to create a moisture concentration gradient, causing moisture to move from the product's inside to its outside. Temperature variations that are above or below the allowed range induce physical and chemical changes, which eventually degrade the dried product's quality. Because most of the water content is dehydrated, providing air at a controlled temperature improves their storage life, decreases loss, and lowers costs of transportation [2–4].

The most crucial parameter that directly affects the drying rate is the temperature within the drying chamber. The major problem with a traditional solar dryer that doesn't have an auxiliary heat source is that solar energy is unpredictable. Nevertheless, the temperature threshold of drying air is greatly influenced by changing weather conditions and the intermittent nature of solar radiation. Hence, the quality of the dried product diminishes dramatically. As a result, without the presence of another energy source and complete control over all drying parameters, solar dryers are restricted and worthless.

Auxiliary heat of various forms can be used to augment solar energy and reduce drying time even further. During the various phases of the drying process, it is frequently beneficial to alter the rate of airflow passing through the drying system. There's also an auxiliary heating coil for use at night and on wet or cloudy days. Many different techniques of auxiliary heat have been used as complementary tools in the literature. Boughali et al. [5] developed a prototype of an energy-efficient indirect active hybrid solar–electric drier for agricultural goods. Song and Songlin [6] built a hybrid solar dryer that included a heat storage device and supplementary electricity heating. Mortezapour et al. created a hybrid photovoltaic-thermal solar dryer [7].

To ensure a continued drying process and the flexibility to operate the solar dryer under poor weather conditions, Zoukit et al. [8] employed a solar-gas collector in combination with an auxiliary heat system. By formatting the operation of a proportional valve, a control system is required to adjust the gas flow in the injector. Eltief et al. [9] employed a drying chamber, V-groove collectors, two variable-speed centrifugal fans, and an auxiliary electric heater as part of a solar-assisted drying system.

For rice drying, Zomorodian et al. [10] proposed a rig that included six standard solar air heaters, a drying chamber with an electrically rotational discharge valve, an auxiliary electric heating channel, and an air distribution system. During instances of low sunlight, Bennamoun and Belhamri [11] utilized a heater to dry onions. The most essential criteria that impact the dried product quality are the mass flow rate, temperature, and humidity of the air [12,13]. The performance of a solar-only dryer and another solar dryer with an auxiliary heater as a complement to the solar heat is investigated in an experimental study. Khalifa and Al-Dabagh [14] experimentally studied the effectiveness of a solar drying system that uses two flat plate collectors, a blower, and a drying chamber was experimentally tested with and without an auxiliary heater to augment the solar heat, and its performance was compared to that of natural drying. Four distinct airflow rates are used in the tests, namely 0.0383, 0.05104, 0.0638, and 0.07655 $m^3/s$. The drying time was seen to have been cut from 56 hr for natural drying to 12–14 hr for sun drying and to 8–9 hr for combined (solar and auxiliary) drying. As compared to a system that uses only solar energy for drying, it was discovered that the combined system's efficiency increased by 25-40%. Krokida et al. [15] investigated how air drying of different plant materials (potato, carrot, pepper, garlic, mushroom, onion, leek, pea, maize, celery, pumpkin, and tomato) affected the drying kinetics and characteristic sample size. The equilibrium moisture content of dried goods within the range of 0.10-0.90 water activity at two temperatures (30 and 70 °C) was fitted to the GAB equation using a first-order reaction kinetics model. The drying sample size and air conditions were shown to have a significant impact on the model parameters under consideration. In instance, the temperature rise lowers the equilibrium moisture content of the dehydrated items and raises the drying constant.

During thin-layer drying of figs, Babalis and Belessiotis [16] investigated the effect of drying circumstances on the moisture diffusivity and drying constants and found that air velocities larger than 2 m/s had no considerable influence on the drying rate. The air temperature has the greatest impact on the drying kinetics, according to the findings. Purta and Abed [17] built and tested a solar dryer that consists of three main components: a drying sun collector, a solar dryer chamber, and a chimney. A fan was fitted at the chimney outlet to manually expel the hot air outside the solar dryer to boost drying efficiency.

In Basrah province, theoretical and practical research was undertaken by Al-Hilphy et al. [18] for the vacuum solar dryer, who was locally made to dry salted and unsalted carp fish, and it was compared to natural sun drying and vacuum electric dryer. It was found that the moisture content of dried fish dried using a vacuum solar dryer and a vacuum electric dryer were similar, although it was much better than sun-drying.

Ajiwiguna [19] experimented to find the impact of air temperature and velocity on evaporation rate. According to the findings, the impact of temperature is less important at high air speed. Suherman et al. [20] investigated the seaweed drying performance of a hybrid solar dryer combined with an auxiliary heater. Hybrid sun drying and conventional drying were both used to dry the samples. El Ferouali et al. [21] developed a new hybrid solar-electric dryer in which an electric auxiliary heater was put within the drying chamber to provide temperature control. Silva et al. [22] used the Photovoltaic PV system to power the blowers and the electric heater to provide a long-term drying solution. The maize grains were dried from 23 % moisture to 13 % moisture in 8.5 hours, with an average thermal and drying efficiency of 27 % and 6%, respectively.

Jadallah et al. [23] proposed a developed computational and experimental design of a hybrid PV Thermal double-pass counterflow system connected with a mixed-mode solar dryer system. The temperature of the solar cells was reduced by manually pumping air into the Photovoltaic thermal PVT system via a fan-created by the PV module, hence increasing the PV module's electrical efficiency. The air is passed from the fan to the PVT solar system, then into the drying chamber, using the forced convection mode.

The majority of previous studies have concentrated on the possibility of improving the solar dryer's efficiency by utilizing an extra heat source. A backup heater and variable airflow rates are employed to build an indirect solar dryer for large-scale agricultural drying, with solar mode (energy provided exclusively by solar energy) and electrical mode (energy provided solely by electrical power) dominated by a control system. When the temperature and relative humidity in the drying chamber change, the control system adjusts the amount of auxiliary heating and airflow as needed as a backup to solar energy.

In the present study, an indirect type solar dryer was proposed and developed to improve the drying process of agricultural products such as (banana). The dryer consists of a solar air collector, an isolated drying chamber, an auxiliary (electric) heat source, and an electric fan to drive the hot air according to the temperature and moisture in the dryer chamber. The most common function of the dryer is to blow hot air onto the product, forcing the water in it to evaporate. The effect of air temperature and velocity on the evaporation rate will be studied experimentally. The tests will be conducted at three different air flow rates. For variable air flow rates, the solar mode and the electric mode were experimentally tested with only one power supply in each mode.

## 1. Experimental system setup

The experimental setup includes a flat plate air solar collector and an indirect solar dryer with forced convection mode, as illustrated in Fig. 1, with external methods, such as a cross-flow cooling fan, for transporting solar energy in the form of hot air from the solar collector to the drying chamber. Between the absorber plate and the glass, heated air is transmitted. To optimize solar radiation exposure, the solar collector is affixed to a support structure that is inclined at a 30° angle to the horizon and faces south. Drying air enters the chamber directly after leaving the solar collector through a rectangular opening (Air Intake) with dimensions of (0.7 m × 0.06 m). The underside of the constructed drying chamber is connected to an electrical heater (220V 4kW, accuracy ±2%) acting as an auxiliary source.

The air passes through the trays from the bottom to the top. The drying chamber is made of galvanized iron plate measuring (1.50 m × 0.87 m × 0.87 m) in dimension. The products are entered through an insulated door and mounted on the trays inside the drying cabinet. There are three trays, each with a dimension of 0.85 m × 0.65 m. The trays are made up of Plastic wire mesh having a thickness of 0.004 m and surrounded by a wooden frame. The sidewalls, bottom, and door of the drying chamber are made of two layers of steel (2 mm thick) separated by a polyurethane insulating foam layer (5 cm thick).
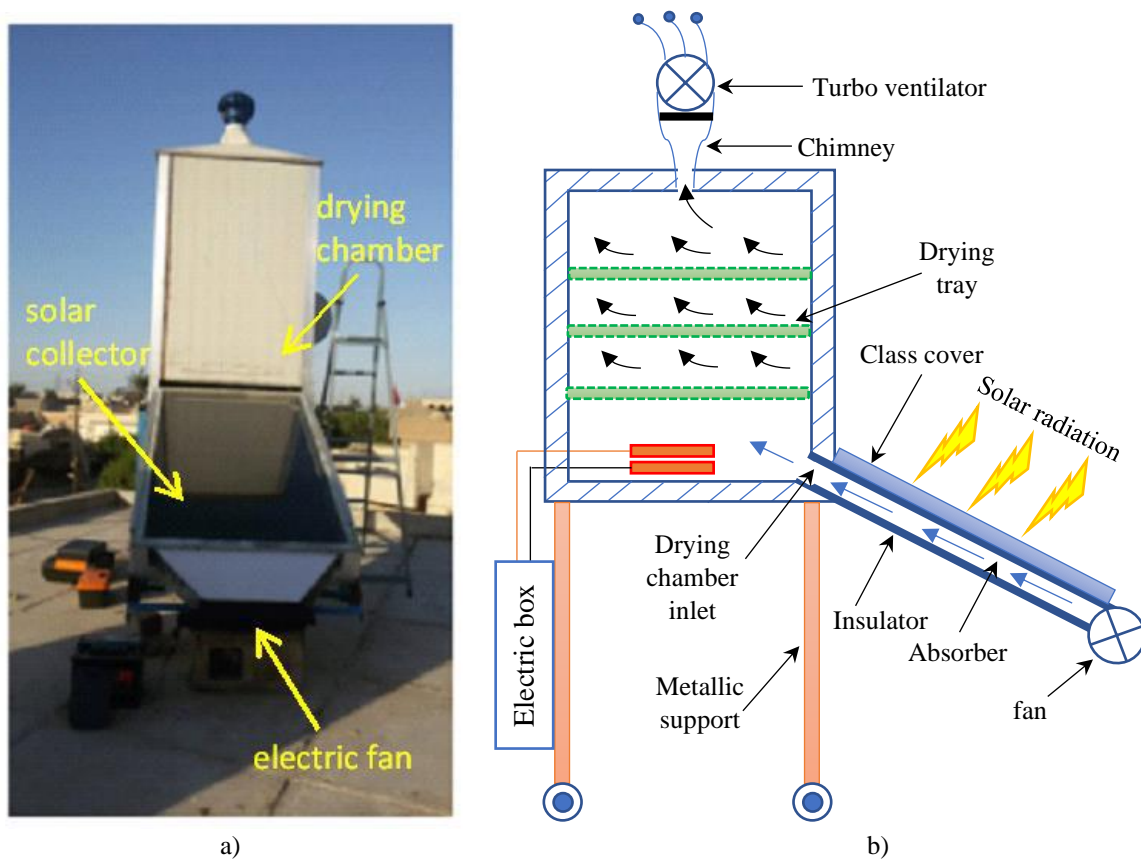


**Fig. 1.** Experimental set-up: a) photographic image and b) a schematic diagram of the solar dryer.

The distance between the lowest tray and the solar drying chamber's base is 0.40 m, with a gap of 0.15 m between each tray. When the sun goes down, an auxiliary backup heater is employed to assist this system

to replace solar energy. In both circumstances, the fan continues to function in line with the drying environment and uniform hot air circulation throughout the chamber. The flow of heated air within the drying chamber causes the drying process to take place.

## 2. System implementation procedure

Experiments on drying were carried out in October 2020 from 7:00 a.m. to 5:00 p.m., with solar radiation as the heat source. The next day, from 5:00 p.m. until 7:00 a.m., a new source was added to the drying system. The tests were implemented in Baghdad, Iraq (latitude 33.333 and longitude 44.433) on days with a clear sky on the 21, 22, and 23 October, respectively. For both heating modes, several experiments were implemented on the systems utilizing varying airflow rates of 0.042, 0.0735, and 0.105 m³/s. In the drying experiments, fresh banana slices were used. Banana slices, with a thickness of 4–5 mm, were chosen for optimal drying.

The reduction in moisture content was calculated by weighing the product sample every hour. The system must first be brought to steady-state conditions before the tests can begin. As a result, each test run must be preceded by an operating period of at least 1 hour. The (SM206-SOLAR) solar meter was employed to measure the global components of solar radiation in real-time. Also, the temperature of the collector inlet and outlet, the temperature of the absorber plate, the temperature of the exterior glass cover, the temperature of the drying chamber inlet and outlet, and the temperature of the product were all measured using a Lutron (TM – 903 A) four-channel temperature data logger.

A TES-1341 hot-wire anemometer relative humidity was used to measure the relative humidity of the ambient air and the entrance of the drying chamber. The air speed was measured by using wind speed (UNI-T UT362 anemometer with USB). To acquire the average value of air speed, the air exit speed was measured at three positions in the exit air throat of the aperture area at the top of the drying chamber. The average speed could be used in determining the air density and cross-section area of the aperture area and the air mass flow rate. All specifications of the measuring devices are listed in Table 1.

**Table 1.** The specifications of measuring instruments

| Instrument | Accuracy | Range | Resolution |
|---|---|---|---|
| SM206-SOLAR   Solar irradiation meter | ±5% of reading | 1-3999 w/m² (btu) | 0.1 W/m² |
| Lutron (TM – 903 A), 4 channels temperature data logger | $\pm$ (0.5 % + 1 °C) | - 100 °C to 1300 °C | 0.1 ° C. |
| Lutron HT-3007SD Humidity/Temperature Meter | 3% reading + 1% RH., 0 to 50°C | 5 % to 95 % R.H., ± 0.8°C | 0.1 % R.H., 0.1 degree |
| TES-1341 HOT-WIRE ANEMOMETER relative humidity | ±3% RH | 10% to 95% | ±3%RH |
| UNI-T UT362 anemometer with USB | (± 3%+5) | 2~10 m/s | ----- |

## 3. Analysis of dryer performance

The moisture content is computed using the equation below:

$$M = \frac{W_o - W_d}{W_o} \times 100,$$  (1)

where $M$ is the moisture content (g water/g dry solid), $W_o$ is the initial weight of undried product (g), $W_d$ is the weight of dry matter in produce (g).

Many factors impact the effectiveness of a flat plate collector, including the collector's size, geographic location, velocity, humidity, and ambient air temperature, among others. The solar collector's thermal efficiency is calculated as follows:

$$\eta_c = \frac{\dot{m}_a \, c_{pa} \, (T_{oc} - T_{ic})}{A_c \, I}.$$  (2)

Here $\eta_C$ is the efficiency of solar collector, $\dot{m}_a$ is the air mass flow rate (kg/s), $C_{pa}$ is the air specific heat (kJ/kgK), $T_{oc}$ is the Exit air temperature of collector (°C), $T_{ic}$ is the input air temperature of collector (°C), $A_c$ is the area of collector (m$^2$), and $I$ is the global solar radiation (W/m$^2$).

The solar collector's thermal efficiency was determined to be 28% for average solar radiation of 600 W/m$^2$ and average input and exit air temperatures of 31°C and 45°C, respectively. The thermal efficiency of the solar dryer system can be calculated as follows [24].

$$\eta_d = \frac{m_w \, h_l}{A_c \, I \, t},\tag{3}$$

The efficiency of the heater is determined as:

$$\eta_h = \frac{\dot{m}_a \, C_{pa} \, (T_{oc} - T_{ic})}{I_e \, V},\tag{4}$$

where $\eta_d$ is the efficiency of the solar dryer (%), $\eta_h$ is the efficiency of the heater (%), $M_w$ is the mass of evaporated water (kg). $h_l$ is the latent heat of vaporization (kJ/kg), $t$ is the Solar drying time (hour), $I_e$ is the electric current (A), and $V$ is the voltage (V).

Understanding the performance parameters of solar dryers requires analyzing them. Depending on the current circumstances, which are dictated by the partial pressure vapors in the air and as well as the gradient of the vapor pressure of water contained in the product, a wet product exposed to the air stream may lose or acquire moisture. Assume that the vapor partial pressure in the air in a sample remains constant, we will arrive at a situation known as equilibrium moisture content after passing a stream of air through it for a long enough time (EMC). The EMC is affected by temperature, relative humidity, and the product's nature. These equilibrium moisture relationships are normally expressed mathematically. The equilibrium moisture content can be calculated as follows [25]:

$$\%RH = 1 - exp(- K_t \, (EMC)^N),\tag{5}$$

where %$HR$ is the equilibrium moisture content, $K_t$ and $N$ are constant, and $EMC$ is the equilibrium moisture content.

### 3.1 Activity of water

The more water in a product, the better it is for microbial development, which affects shelf stability and safety. A banana's water activity is estimated to be (0.987–0.964) [26]. The following equation [27] can be used to calculate the water activity.

$$a_w = \frac{EMC}{100},\tag{6}$$

where $a_w$ is the Equation of water activity.

The difference in moisture content between the materials to be dried and the equilibrium moisture content is usually related to the drying rate. The drying rate is proportional to the change in moisture content between the items to be dried and the content of equilibrium moisture, according to the following equation [28]:

$$A_{dr} = \frac{m_o}{t_d},\tag{7}$$

where $A_{dr}$ is the Average drying rate (kg/hr), $m_o$ is the Moisture mass removed by solar heat (g), and $t_d$ is the Overall drying time (hour). The following equation [29] can be used to calculate the quantity of moisture to be extracted from the product, $m_w$:

$$m_w = m_i \left(\frac{M_i - M_f}{1 - M_f}\right),\tag{8}$$

where $m_i$ is the initial mass of product to be dried (g), $M_i$ is the Initial moisture content on a % wet basis, $M_f$ is the final moisture content % wet basis.

## 4. Results and discussion

Throughout October 2020, several continuing experimental testing on the improved dryer were conducted. Figures 2 and 3 show the time variation of solar intensity (I), ambient temperature ($T_a$), inlet temperature ($T_i$), and outlet temperature ($T_o$) of air from the drying chamber, for three consecutive days on October 21, 22, and 23, 2020, with three different airflow rates of 0.042, 0.0735, and 0.105 m³/s, respectively. It is clear that all figures are a natural phenomenon and a clear fact based on the weather data at that location and these days of the year. Temperature changes are exactly related to intensity changes, as seen in the figures. In addition, there is a large difference in hot air and ambient temperature due to the collector's capacity to heat the surrounding air.
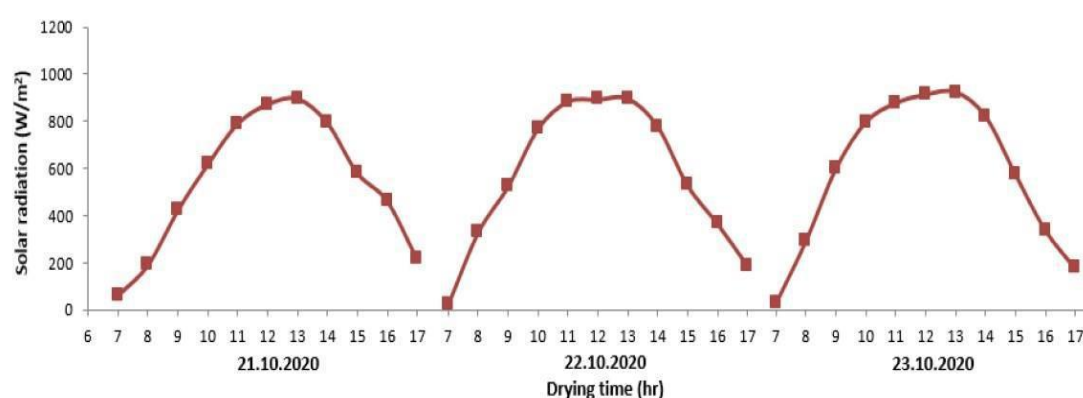


**Fig. 2.** Variation of the intensity of solar radiation (*I*) versus drying time
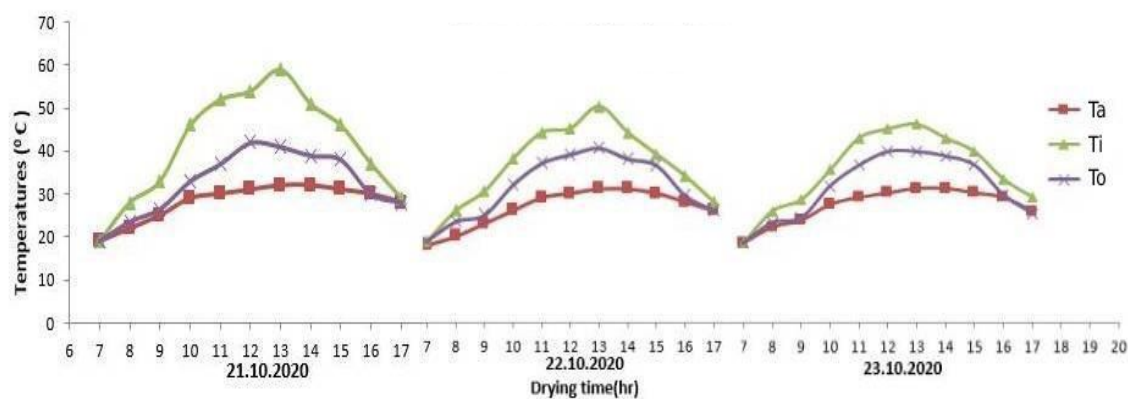


**Fig. 3.** Ambient temperature ($T_a$), drying chamber inlet air temperature ($T_i$), drying chamber outlet air temperature ($T_o$) versus drying time.

Fig. 4 demonstrates the variation of relative humidity with solar drying time for various airflows. It can be observed that relative humidity decreases as drying time rises, peaking at 13:00, before rising again at 17:00 for all airflows at the end of the sunny hours. It can be seen that the relative humidity is the lowest in the chamber dryer at airflow of 0.105 m³/s compared to the lowest values for airflows.

The speed of the air may not be sufficient to carry away the moisture from the material surface to the outside of the drying chamber, so the relative humidity of the air increases at low flow rates. Also, with a higher airflow of 0.105m³/s, relative humidity is very low in the drier, which is helpful for a faster drying rate since low humid air has a greater potential to absorb moisture. The most significant criteria for successful drying are a greater temperature and lower relative humidity.

Fig. 5 depicts the chamber temperature ($T_r$) as a function of overall drying time ($t_d$) under varied airflow rates. When applying an additional source (backup heater) to the dryer from 1 a.m. to sunrise at 5:23 a.m., the drying chamber temperature dropped slightly as drying time increased due to the low temperature of the ambient air.

The heater continues to heat the air until 7:30 a.m., after which the heater is shut off and only solar radiation is used to heat the air flowing over the solar collector's absorber surface. The radiation is low at the start of the day, gradually increasing until it peaks at midday, and then gradually decreasing until it reaches its lowest point at sunset. Throughout the day, the temperature rise is determined by the radiation levels. Due to the absence of solar radiation energy at sunset and the decreased ambient air temperature, a backup heater is employed once again. The temperature of the chamber decreases as the airflow rates increase in all three scenarios.
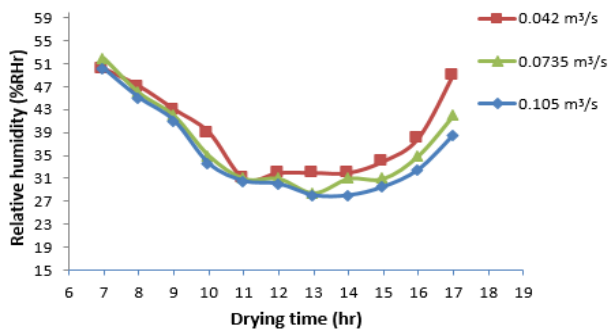


**Fig. 4.** The drying chamber humidity ratio vs. solar drying time under variable airflow rates
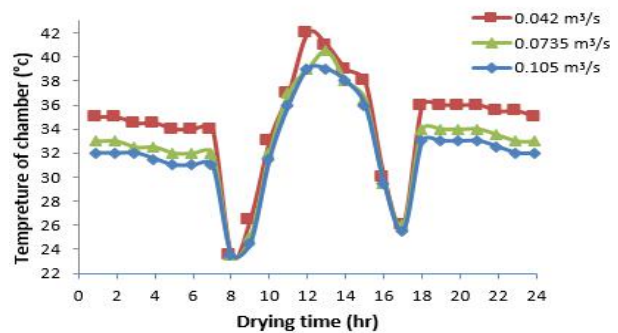


**Fig. 5.** Drying chamber temp. of ($T_r$) with auxiliary heat source vs. overall drying time ($t_d$) under variable airflow rates

Fig. 6 shows how larger airflows improve drying system efficiency because more air passes over the product perimeter, forcing water vapor to evaporate and therefore improving the drying rate. The drying system's efficiency improves as the airflow velocity rises. Fig. 7 depicts the relationship between moisture content and overall drying time for various airflow speeds. At the beginning of the drying curve, there is a constant drying rate, followed by a falling rate drying period. It's worth noting that the drying rate remains constant at the start of the drying curve before rapidly decreasing.
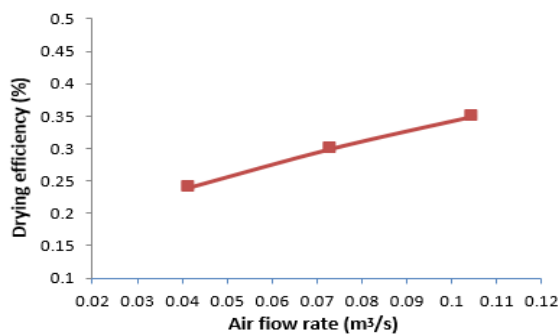


**Fig. 6.** Drying system efficiency vs. air flow rate
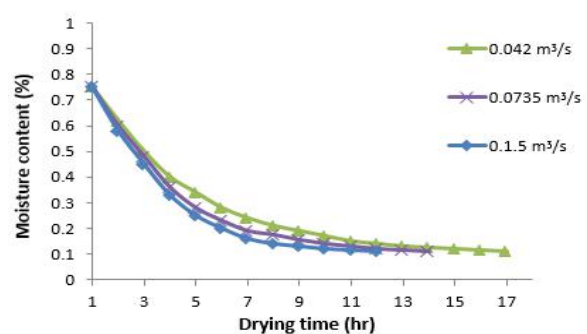


**Fig. 7.** Moisture content vs. overall drying time under variable airflow rates

Moisture will be removed by evaporation as air passes over the surface of banana slices, and moisture will be continuously transported from the inner portion of the slice to the surface in an attempt to maintain that moisture pool. Nevertheless, the surface moisture pool will eventually disappear. At this point, the dryer will start a decreasing rate drying period, in which moisture must diffuse from the material's core to the surface. The amount of water that evaporates steadily reduces over time in the lowest airflow used during measurements, even though the banana receives considerable heat. The impact of controlling air flow rate on sun drying time depends on the strength of solar radiation. In light of this, monitoring the dryer's functioning is made easier by the temperature and humidity measurements.

## Conclusions

The performance of the solar dryer including an auxiliary heat source was evaluated in an experimental investigation with varying airflow speeds. From the results, some conclusions can be drowning as follows:

1. The air temperature in the range of 32-42 ºC within the drying chamber may be maintained throughout the duration of the product drying by using an additional heat source in addition to sun radiation.

2. It's a good idea to use an electric fan and backup heater to improve the dryer's thermal performance. As a result, the proposed dryer is more effective and practical than the conventional solar dryer in drying and heating applications.

3. The proposed dryer speeds up the drying process (decrease in drying time) and thus minimizes humidity and spoilage risk, and increases product quality. This will significantly reflect on the performance efficiency.

4. Higher air temperatures have a considerable influence on the drying rate in the early stages of drying, but this effect decreases after around 10–15 hours.

5. Because it inhibits the creation of the stagnant boundary layer air, air velocity has a significant impact in the early stages of drying. This means that the air around the product will not be saturated, preventing steam from leaking into the surrounding air.

6. The maximum average drying efficiency was determined to be 35 % at a flow rate of 0.105 $m^3$/sec, with average solar radiation of 600 $W/m^2$ and an average ambient temperature of 27.5°C, with a relative humidity of 35.136 % in the drying chamber.

7. The drying time at varied flow rates of 0.042, 0.0735, 0.105 $m^3$/sec with a moisture content of 0.11 was 17, 14, 11.5 hours during daylight hours, respectively.

## REFERENCES

1    Mohana Y., Mohanapriya R., Anukiruthika T. , Yoha K.S., Moses J.A., Anandharamakrishnan C. Solar dryers for food applications: Concepts, designs, and recent advances. *Solar Energy*. 2020, Vol. 208, pp. 321 – 344. doi:10.1016/j.solener.2020.07.098

2    Fudholi A., Sopian K., Ruslan, M.H., Sulaiman, M.Y. Review of solar dryers for agricultural and marine products. *Renew. Sustain. Energy Rev*. 2010, Vol.14, pp. 1–30. doi:10.1016/j.rser.2009.07.032

3    Afriyie J.K., Nazha M.A.A., Rajakaruna H., Forson F.K. Experimental investigations of a chimney-dependent solar crop dryer. *Renew. Energy*. 2009, Vol.34, pp. 217 – 222. doi:10.1016/j.renene.2008.04.010

4    Kumar R., Chauhan R., Sethi M., Sharma A., Kumar A. Experimental investigation of effect of flow attack angle and thermohydraulic performance of air flow in a rectangular channel with discrete V-pattern baffle on the heated plate, *Adv. Mech. Eng*. 2016, Vol.8, pp. 1–12. doi:10.1177/1687814016641056

5    Boughali S., Benmoussa H., Bouchekima B., Mennouche D., Bouguettaia H., Bechki D. Crop drying by indirect active hybrid solar-Electrical dryer in the eastern Algerian Septentrional Sahara, *Solar Energy*. 2009, Vol.81, No.12, pp. 2223–2232. doi:10.1016/j.solener.2009.09.006

6    Song M., Songlin Y., Biguang Z., Dong Z. Experimental Research of Grape Drying Using Solar Dryer with Latent Heat Storage System. *Int. Conf. on Computer Distributed Control and Intelligent Environmental Monitoring*. 2011, pp. 740– 742. doi: 10.1109/CDCIEM.2011.33

7    Mortezapour H., Ghobadian B., Minaei S., Khoshtaghaza M.H., Mortezapour H., M.S. Saffron. Drying with a Heat Pump – Assisted Hybrid Photovoltaic – Thermal Solar Dryer, *Drying Technology*. 2012, Vol.30, No.6, pp. 37–41. doi:10.1080/07373937.2011.645261

8    Zoukit A., El Ferouali H., Salhi I. Doubabi S., Abdenouri N., El Kilali T. Control of a solar dryer using a hybrid solar gas collector. *2016 Inter. Conf. on Elect. Sci. and Tech. in Mag. (CISTEM)*. doi:10.1109/CISTEM.2016.8066825

9    Eltief S.A., Ruslan M.H., Yatim B. Drying chamber performance of V-groove forced convective solar dryer. *Desalination*, 2007, Vol.209, No.1, pp. 151–155. doi:10.1016/j.desal.2007.04.024

10   Zomorodian A., Zare D., Ghasemkhani H. Optimization and evaluation of a semi-continuous solar dryer for cereals (Rice, etc). *Desalination*, 2007, Vol.209, No.1, pp. 129–135. doi:10.1016/j.desal.2007.04.021

11   Bennamoun, L. and Belhamri, A. Design and simulation of a solar dryer for agriculture products, *Journal of Food Engineering*. 2003, Vol.59, pp. 259–266. doi:10.1016/S0260-8774(02)00466-1

12 Chanakarn C. Drying by Producer Gas from an Up-Flow Gasifier. *Department of energy technology king Mongkut, s University of Technology Thonburi*, 1991. https://www.researchgate.net/publication/237134220

13 Elston A.J. Rates of Water Vapour Adsorption from Air by Silica Gel. *Industrial and Engineering Chemistry*. 1939, Vol.31, No.8, pp. 988–992. doi:10.1021/ie50356a014

14 Khalifa A.N., Al-Dabagh A. An Experimental Study of Vegetable Solar Drying Systems with and without Auxiliary Heat. *ISRN Renewable Energy*, 2012, Vol.2012, pp. 1-8. doi:10.5402/2012/789324

15 Krokida M.K., Karathanos V.T., Maroulis Z.B., Marinos-Kouris D. Drying kinetics of some vegetable. *Journal of Food Engineering*, 2003, Vol.59, No.4, pp. 391-403. doi:10.1016/S0260-8774(02)00498-3

16 Babalis S.J., Belessiotis V.G. Influence of the drying conditions on the drying constants and moisture diffusivity during the thin-layer drying of figs. *J. of Food Eng.*, 2004, Vol.65, No.3, pp. 449-458. doi:10.1016/j.jfoodeng.2004.02.005

17 Abed E.M. Design and Testing Solar Dryer Performance. *Eng. and Tech. J.* 2013, Vol.31, No.12, pp. 169-184. doi:10.30684/etj.31.12A.14

18 Al-Hilphy A.R.S., Al-Shatty S.M.H., Gahffr A.A. A Practical and Theoretical Study of the Locally Manufactured Vacuum Solar Dryer for Fish Drying. *Eng. and Tech. J.* 2016, Vol.34, No.3, pp. 76-91. doi: 10.30684/etj.34.3B.17

19 Purta R.N., Ajiwiguna T.A. Influence of Air Temperature and Velocity for Drying Process. *Procedia Engineering*. 2017, Vol.170, pp. 516 – 519. doi:10.1016/j.proeng.2017.03.082

20 Suherman S., RIzki H., Rauf N., Susanto E.E. Performance study of hybrid solar dryer with auxiliary heater for seaweed drying. *Journal of Physics: Conf. Series*. 2019, Vol.1295, No.012002. doi:10.1088/1742-6596/1295/1/012002

21 El Ferouali H., Zoukit A., Salhi I., El Kilali T., Doubabi S., Abdenouri N. Optimization study and design of a hybrid solar-electric dryer suitable to the developing countries context. *Solar for Africa and Renewable Energies Journal (SARE)*, V1-FEB19. 2019, pp. 35-39. https://www.researchgate.net/publication/337496021

22 Silva G.M., Ferreira A.G., Coutinho R.M., Maia C.B. Experimental Analysis of Corn Drying in A Sustainable Solar Dryer. *Journal of Advanced Research in Fluid Mechanics and Thermal Sciences*. 2020, Vol.67, No.2, pp. 1-12. https://www.akademiabaru.com/submit/index.php/arfmts/article/view/3569

23 Jadallah A.A., Alsaadi M.K., Hussien S.A. The Hybrid (PVT) Double-Pass System with a Mixed-Mode Solar Dryer for Drying Banana, *Eng. and Tech. J.* 2020, Vol.38, No.8, pp. 1214-1225. doi:10.30684/etj.v38i8A.535

24 Midilli A. Determination of pistachio drying behavior and conditions in a solar drying system, *International Journal of Drying Res*. 2001, Vol.25, No.8, pp. 715-725. doi:10.1002/er.715

25 Iglesias and Chirfe, 1982; ASAE, 2000.

26 Chirife J., Fontan C.F. Water activity of fresh foods. *Journal of Food Science*. 1982, Vol.47, pp. 661-663. doi:10.1111/j.1365-2621.1982.tb10145.x

27 Barbosa-Cánovas G.V., Fontana A.J., Schmidt S.J., Labuza T.P. Water Activity in Foods: Fundamentals and Applications. *John Wiley & Sons*, 2020, Inc. ISBN:978-1-118-76831-0

28 Adelaja A.O., Babatope B.I. Analysis and Testing of a Natural Convection Solar Dryer for the Tropics. *Journal of Energy*. 2013, Vol.4, pp. 1-8. doi:10.1155/2013/479894

29 Moisture P.Y. Water Activity. *Handbook of Processed Meats and Poultry Analysis*. 2008, pp. 35-67. doi:10.1201/9781420045338.ch3.

# MODELING THE DYNAMICS OF HEAT AND MASS TRANSFER PROCESSES IN A TUBULAR HEAT EXCHANGER UNDER PULSED INFLUENCES

Sakipova S.E., Shaimerdenova K.M., Nussupbekov B.R., Ospanova D.A., Kutum B.B.
bota_didar@mail.ru

E.A. Buketov Karaganda University, Karaganda, Kazakhstan

*The paper discusses the results of experimental studies of the influence of the degree of inhomogeneity of a liquid flow on the dynamics of heat and mass transfer processes under pulsed impacts. High-voltage electric discharges in a liquid medium were used as impulse actions, through which an electro-hydraulic effect is realized, accompanied by the appearance of shock waves. The dynamics of the occurring nonlinear, rapidly changing heat and mass transfer processes at high hydraulic pressures cannot be described using differential equations. The simulation was carried out on the basis of the method of group consideration of arguments, the advantage of which is the construction of polynomial dependencies using a small amount of experimental data. The results of constructing polynomial dependences made it possible to reveal the synergistic effect of the influence of flow parameters on the dynamics of the impulse pressure amplitude and the intensity of heat transfer.*

**Keywords:** heat and mass transfer, tubular heat exchanger, diffuser, method of group consideration of arguments, impulse action, electrohydraulic effect, heat transfer rate.

## Introduction

The widespread use of electricity and thermal energy leads to the development of methods for increasing the efficiency of heat exchange processes, which helps to reduce overall energy consumption and protect the environment. At industrial and energy enterprises and branches of technology, the task of intensifying the heat transfer process and creating highly efficient heat exchangers is very relevant. The efficiency of each stage of electricity production is discussed and ways to improve the efficiency of heat production are proposed [1-7]. It's known that at the transport enterprises of thermal power engineering and in many industrial production processes, processes are responsible for heat consumption due to the movement of the coolant in the form of hot water through pipelines that are limited by parameters and configuration. To implement specialized technologies, a heterogeneous flow is used, consisting of water-soluble solutions with gaseous solutions and chemical impurities in the form of components.

At thermal power plants, industrial water is used as a heat carrier, which, before entering the heating boilers and steam generators, undergoes a 2- or 3-stage purification from impurities. But during operation, a layer of solid scale deposits is formed on the internal surfaces of tubular heat exchangers, which impair the efficiency of the heat exchanger by reducing the diameter of the pipeline [3-5]. Thus, after a certain period of operation, the purified water becomes a non-uniform flow. The degree of heterogeneity associated with the presence of gaseous and solid impurities can sometimes cause undesirable effects, such as an increase or, conversely, a decrease in pressure, which leads to a significant change in the intensity of heat transfer. These factors necessitate the study of the mechanisms of formation of hard scale deposits on the internal surfaces of tubular heat exchangers, and, accordingly, the development of technologies for removing such deposits.

Among the many methods of treating heat exchange objects from deposits, the most effective method is the electrohydraulic effect (EHE), in which the conversion of thermal energy into mechanical energy without intermediate energy conversion takes place [8]. EHE is based on the phenomenon of a strong effect of a hydraulic wave, accompanied by a high-voltage pulsed development of a discharge in an aqueous medium [9]. Non-linear, non-stationary, rapidly changing heat transfer processes, in which physical parameters increase with large gradients, cannot be described using differential features. In practice, semi-empirical formulas with large numerical constants are used to describe them, but they are valid in a narrow range of parameters. In this regard, modeling of heat transfer processes in pipes with a two-phase coolant under

pulsed impacts is still an urgent engineering problem. The development of computer technology and the creation of new application software packages make it possible to quickly process data and simulate complex physical processes with great care. In this paper, we consider the results of modeling the parameters of a pulsed heat transfer process in an inhomogeneous aqueous medium using the method data regression analysis

## 1. Method of group consideration of arguments

Method of group consideration of arguments (MGCA) consists in building statistical models using regression analysis of experimental data and allows you to get the most adequate solutions that are consistent with the real physical picture [10]. The correct choice of support functions is carried out automatically by the combinatorial MGCA algorithm. Interpolation is reduced to direct restoration of a polynomial function from a small number of points (interpolation nodes) determined from the experiment. Based on the universal laws of the theory of self-organization, MGCA allows you to get the most adequate solutions that are consistent with the real physical picture. A preliminary model is compiled, which is further refined using single and multiple forecasts synthesized using the MGCA. The advantage of MGCA is that even when using 6 - 10 points taken from observations, this method allows you to build a model of arbitrarily high complexity.

The selection criterion is the most important parameter that must be set in the design module for the MGUA. The criterion used is the GCV - Generalized Cross Validation criterion, which is defined as

$$GCV = Norm. \ MSE \ / \ (1 - KK \times k/N)^2,$$

where Norm. MSE is the normalized *mean squared error*;

KK - criterion coefficient;

N is the number of points in the data file;

k is the number of coefficients to minimize the mean squared error.

Based on the enumeration of various models, a combinatorial MGCA algorithm is determined. On each MGCA layer, a polynomial of the following form is constructed:

$$C_0 + C_1 \cdot X_1 + C_2 \cdot X_2 + C_3 \cdot X_3 + C_4 \cdot X_1 \cdot X_2 + C_5 \cdot X_1 \cdot X_3 + C_6 \cdot X_2 \cdot X_3 + C_7 \cdot X_1^2 + C_8 \cdot X_2^2 + C_9 \cdot X_3^2,$$

where $C_0$ is a constant, $C_1$, $C_2$, ... are coefficients, and $X_1$, $X_2$, $X_3$ are input variables.

Based on the results of the calculations, a technique for constructing binomial dependencies was developed that most accurately describes the experimental data on the dependence of the intensity of heat and mass transfer processes on the frequency of electro-hydro-impulse action in a liquid coolant [11]. Let us consider the possibility of constructing functional dependences of the impulse pressure and heat transfer intensity on the parameters of the coolant motion using the method of group consideration of arguments (MGCA).

## 2. Experimental data

The relevance of the study of rapidly changing, high-gradient processes associated with the propagation of shock waves in inhomogeneous media is of great practical interest. This is due to the importance of its application in a wide variety of technological processes, where the energy of impulse pressure is widely used for pressing, crushing, destruction of solid deposits on the inner surfaces of pipes of heat exchangers, pipelines, oil pipelines, etc. [6]. The pulse pressure amplitude reaching $\sim(10^8 \div 10^9)$ N/m$^2$ within $\sim(10^{-4} \div 10^{-5})$ s depends on the state of the working medium and on the geometry of the working area where the shock wave propagates [12-17]. The propagation of the shock wave is fast, the pressure pulses have a duration of $\sim10^{-4}$ s. The study of the patterns of propagation of wave processes is important for the development of methods for regulating the intensity of the dynamic impact of shock waves.

The analyzed experiments were carried out in technical water with the presence of solid, conical reflectors, rigidly fixed in the working area in order to enhance the action of the shock wave accompanying the discharge in a given direction [6]. In [16] presents the results of an experimental study of methods for controlling the power of the electrohydraulic effect by varying the degree of heterogeneity of the working medium and the geometry of the working channel with the same electrical parameters of the discharge. The possibility of cumulation of impulse pressure by using conical reflectors with a certain degree of heterogeneity of the working medium has been established.

The control and measuring system of the electro-hydraulic installation makes it possible to observe the change in pressure pulses by time sweeps of voltage and current. Description of the electro-hydraulic installation, the device and the principle of measuring pulsed pressure with an amplitude of up to (50-60) bar

and a signal duration of ~ (0.001÷0.005)s using a piezometric sensor are given in [6, 8-10]. Calibration of the sensor was carried out in the installed state on the working section of the experimental stand using the dynamic method. During calibration, the cover of the working area was replaced by a device consisting of a cylinder and a piston. Using a storage oscilloscope, the electrical signals from the piezometric sensor were recorded at a given hydraulic force of the piston impact. In the experiments, reflectors with a taper angle θ: 0°, 10°, 30°, 45°, were used, made of a sufficiently strong synthetic material, kapralan. Testing was carried out repeatedly, the measurement error was 5-7%. The volumetric gas content coefficient $\varphi$ and the angle $\theta$ of cone-shaped reflectors placed in the working area in order to increase the pressure force in a given direction were used as variables [6]. The degree of volumetric gas content is equal to:

$$\varphi = \frac{V_g}{V_g + V_l},$$

were $V_g$, $V_l$ - volume of gas and liquid.

As a result of repeated measurements, a nonlinear dependence of the pressure amplitude on the value of the taper angle was found.

### 3. Results and discussion

### 3.1 Modeling impulse pressure dynamics

Let us consider the results of the analysis of experimental data on the study of the dependence of the pressure amplitude accompanying a high-voltage electric discharge in an inhomogeneous medium. Experiments have shown that the magnitude of the amplitude of the pulsed pressure during EHP exposure in an inhomogeneous aquatic environment depends on the degree of gas content. As a result of the regression analysis of the experimental data using various selection criteria, polynomial models were constructed that describe the dependences of the impulse pressure amplitude at various concentrations of the gas phase and various boundary conditions. To calculate the magnitude of the pulse pressure amplitude based on the MGCA method, an expression was obtained in the form of binomials:

$$P = 25 + 17.2 \cdot \varphi - 0.85 \cdot \theta + 0.063 \cdot \theta^2 - 0.00096 \cdot \theta^3 - 19.25 \cdot \varphi^2 + 5.2 \cdot \varphi^3 + 0.26 \cdot \varphi \cdot \theta - 0.02 \cdot \varphi \cdot \theta^2 + 0.00031 \cdot \varphi \cdot \theta^3 \qquad (1)$$

The results of modeling the magnitude of the impulse pressure according to this formula with a change in the degree of gas content of the liquid working medium at different taper angles are shown in Fig.1.



a) θ = 0°

b) θ = 10°

c) θ = 30°

d) θ = 45°
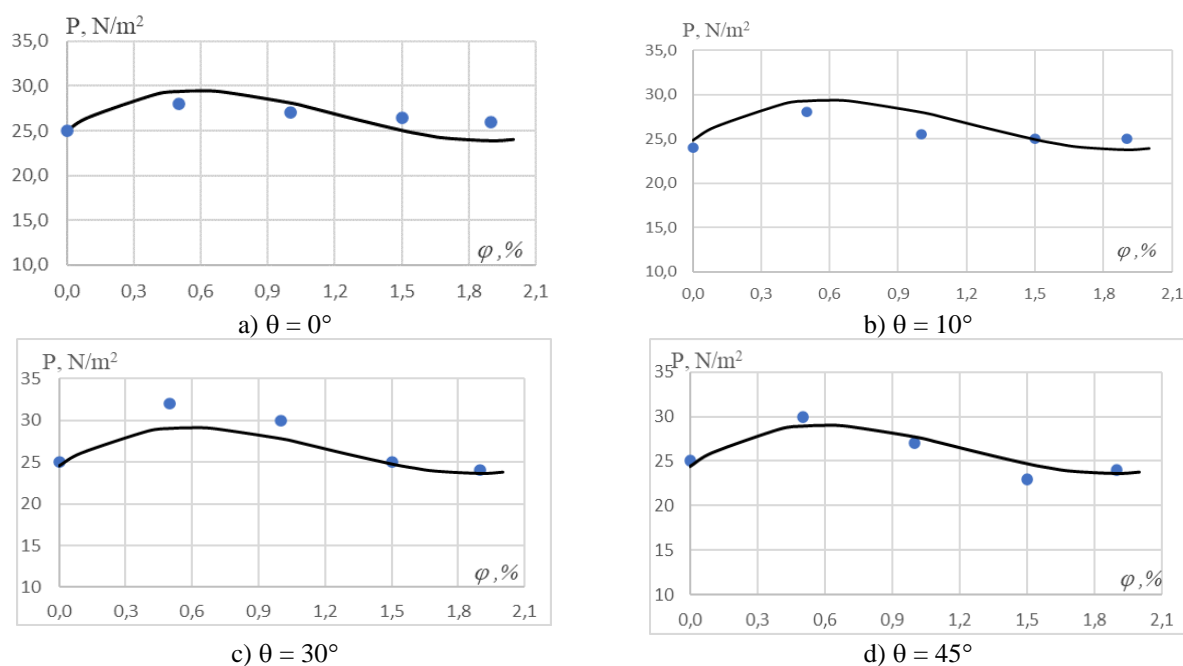
**Fig.1.** Dynamics of the impulse pressure amplitude on the degree of gas content:
lines are calculated by MGCA dependences, points are experimental data

Calculations show that at a volume concentration of carbon dioxide bubbles φ=0.5%, as a result of the simultaneous influence of two effects of cumulation and cavitation, the pressure amplitude can increase up to 1.5 times (Fig.1c). Model (1) describes well the behavior of the experimental data for all values of the angles of the reflectors (the calculation error does not exceed 2÷3%) and confirms the possibility of increasing the pulse pressure at a certain degree of gas content of the working medium.

### 3.2 Modeling of heat transfer dynamics under electro-hydro-pulse impact

Practice has shown that with a constant pulse action, the nature of the coolant flow changes from laminar to turbulent, which in turn contributes to mixing and, accordingly, more intense heat transfer. Analysis of the data showed that the main parameter that determines the degree of heat transfer intensification is the electric discharge frequency f. The intensity of heat transfer, which is determined by the thermophysical properties of the heat exchange surface and depends on the regime of the coolant flow, characterized by the Reynolds criterion. To assess the influence of the main factor - the frequency of the applied electrical pulses in a wide range of boundary conditions, the nature of the dependence of the average value of the Nusselt numbers were analyzed.

$$\text{Nu} = \alpha \times \text{a} / \Delta \lambda_f , \tag{2}$$

where $\alpha$ is a heat transfer coefficient, a is a characteristic linear scale, $\lambda_f$ is the thermal conductivity of the pipe walls.

A pulsed electric discharge causes turbulence in the coolant flow with energy-containing large-scale vortices, the repetition frequency of which determines the nature of the flow and the intensity of heat transfer from the surface. The mechanism of heat transfer intensification by electrohydraulic action is the turbulization of the boundary layer. To describe the results of the experiment using the MGCA, the following dependences for the dimensionless Nusselt number were obtained:

$$\frac{Nu}{Nu_*} = 0.56 + 1.19 \cdot 10^{-5} fq - 1.41 \cdot 10^{-4} q + 0.43 \cdot 10^{-8} q\, Re - 1.09 \cdot 10^{-6} f^2 q + 3.01 \cdot 10^{-8} f^3 q, \tag{3}$$

$$\frac{Nu}{Nu_*} = 0.56 + 1.19 \cdot 10^{-5} fq - 1.41 \cdot 10^{-4} q + 0.51 \cdot 10^{-8} q\, Re - 1.05 \cdot 10^{-6} f^2 q + 3.01 \cdot 10^{-8} f^3 q, \tag{4}$$

where: f is a discharge frequency, Hz; q is the heat flux, W/m2; Re is the Reynolds number.

In the experiments, the magnitude of the discharges was maintained constant, equal to the discharges q = 3393 W/m$^2$, only the discharge frequency f was varied. It can be seen from the graphs (Fig. 2) that model (3) describes the experimental dependence well at low Reynolds numbers, while model (4) is more suitable for regimes with Re > 20000. As can be seen from the graphs, the heat transfer dynamics is determined by the degree of flow turbulence. The difference between the polynomials lies solely in the numerical values of the coefficients, reflecting the joint synergistic effect of the influence of turbulence intensity on heat transfer.
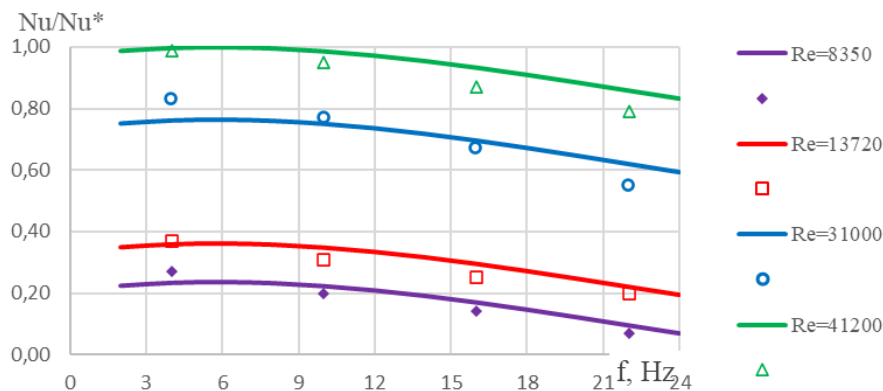


**Fig.2.** Dynamics of the heat transfer from the change in the frequency of discharges $f$;
line - calculation according to MGCA; points - experimental data.

In general, the nature of the regularity does not change, which confirms the fact that the physics of the process is the same for all modes. The use of the MGCA method made it possible to quickly and accurately

process the experimental data of complex nonlinear processes of heat-mass-transfer in inhomogeneous flows and, at the same time, to detect implicit synergistic effects of the mutual influence of various arguments.

## Conclusion

Calculations based on the constructed MGCA model describe well the behavior of the experimental dependences under various boundary conditions. The calculations performed adequately demonstrate the behavior of the experimental data for all angles and confirm the possibility of cumulating the impulse pressure using conical reflectors at a certain degree of heterogeneity of the working medium. The superimposition of the two effects of cumulation and cavitation leads to an increase in the amplitude by almost one and a half times at a given volumetric concentration of the gas phase. An analysis of the results of modeling nonlinear processes shows the advantages of MGCA in building a model of arbitrarily high complexity when using a small number of observations, for example, 6-10 data. This determines its applicability for modeling nonlinear heat transfer processes under variable boundary conditions.

**REFERENCES**

1    Zhang T. Methods of Improving the Efficiency of Thermal Power Plants. *ISPECE 2019 IOP Publishing. Journal of Physics: Conference Series.*  2020, 1449, 012001. doi:10.1088/1742-6596/1449/1/012001

2    Popov I.A., Yakovlev A.B., Shchelchkov A.V., et al. Improving the efficiency of boiler units by intensifying heat transfer. *Energy of Tatarstan.* 2010, No.3 (19), pp. 31-36. [in Russian]

3    Karminsky V.D. *Technical thermodynamics and heat transfer.* Moscow, 2005, 222p. [in Russian]

4    Batrakov P.A., et al. The analysis of the deposit formation on the working surfaces of heat exchange industrial equipment. *Journal of Physics: Conference Series*, 2022, 2182. 012040. IOP Publishing. doi:10.1088/1742-6596/2182/1/012040/

5    Karabelas Anastasios J. Scale formation in tubular heat exchangers. *International Journal of Thermal Sciences.* June 2002. doi: 10.1016/S1290-0729(02)01363-7

6    Nussupbekov B.R., Sakipova S.E., Ospanova D.A., et al. Some technological aspects of cleaning pipes of heat exchangers from solid scale deposits. *Bulletin of the Karaganda University. Physics series.* 2022, No.4(108), pp. 106 -114. doi:10.31489/2022PH4/106-114

7    Methods    for    intensifying    heat    transfer    in    heat    exchangers.    Available    at: https://www.teploobmenka.ru/oborud/art-intensification.

8    Yutkin L.A. *Electrohydraulic effect and its application in industry.* Leningrad, 1986, 253 p. [in Russian]

9 Nussupbekov, B.R., Sakipova, S.E., Edris, A., et al.  Electrohydraulic method for processing of the phosphorus containing sludges. *Eurasian phys. tech. j.* 2022, 19(1), pp. 99–104. doi: 10.31489/2022No1/99-104

10    Ivakhnenko A.G. Long-term control and forecasting of complex systems. Kyiv: Technique, 1975, 312 p.

11    Kussaiynov K., Sakipova S.E., Shaimerdenova K.M.  Modelling of nonlinear processes based on the method of group registration of arguments. *Proceeding of the XI-th Intern. Conf. on the Methods of Aerophysical Research "ICMAR"*, Novosibirsk, 2002, part III, pp.145-147. [in Russian]

12    Fedorov A.V., Fedorova N.N., Fomin P.A., Valger S.A. *Propagation of explosive and shock waves in cluttered spaces.* Novosibirsk, NGASU, 2015, 232 p.

13    Gimaltdinov I.K. Pressure waves in a liquid containing bubble zones. *Bulletin of the Ural State University. Mathematics and mechanics.* Ekaterinburg. 2005,Vol. 8, No. 38, pp. 37 - 52. [in Russian]

14    Gimaltdinov I.K., Bayazitova A.R. Pressure waves in a pipe containing a gas-liquid cluster. *Materials of the XVI session of the Russian Acoustic Society.* Moscow. 2005, pp. 125-129.

15    Dontsov V.E. Propagation of pressure waves in a gas-liquid medium of a cluster structure. *Applied mechanics and theoretical physics.* 2005, Vol.46, No.3, pp. 50 - 60.

16    Sakipova S.E. On the calculation of impulse pressure under electro-discharge action in an inhomogeneous liquid. *Bulletin of Tomsk State University. Mathematics and mechanics.* 2009, No.1(5), pp. 74-81.

17    Lazareva G.G. *Numerical modeling of amplification of shock waves in bubble media.* Diss. cand. phys.-math. Nauk., Novosibirsk, 2003, 155 p. [in Russian]

# COMPUTER MODELING OF PROPERTIES OF A COMPOSITE MATERIAL WITH POROUS FILLERS

## Miryuk O.A.*, Oleinik A.I., Akhmedov K.M.

Rudny Industrial Institute, Rudny Kazakhstan, psm58@mail.ru

*The article is devoted to forecasting of heat-shielding and mechanical properties of composite materials based on porous fillers. Analytical dependencies for determining the thermal conductivity coefficient of materials of homogeneous and heterogeneous structure are given. Based on the finite element method, there has been developed a method for numerical determination of the thermal conductivity coefficient of composite materials with a variotropic structure. The results of computer studies are in line with the dependences obtained on analytical models. The expediency of using multilayer composite materials based on porous fillers in load-bearing and enclosing structures of shell and plate types has been shown.*

**Keywords:** composite material, porous filler, thermal conductivity, finite element method, multilayer shell.

## Introduction

Concrete retains its leading position in the modern construction due to its vast raw material base, the ability to control composition and structure, the variety of products, high technical characteristics and durability. Lightweight concrete is an effective type of composite material that combines mechanical strength with heat-shielding properties. Development of lightweight concrete technology is associated with the creation of highly porous fillers of form stability and development of rational structures of the composite material. Variety of shapes and heterogeneity of the surface of filler's particles, chemical instability of the binder stone, defectiveness of the contact zone set the concrete up as one of the complex artificial composite materials. The structure of concrete, as a composite material, consists of two main components as follows: a matrix (a binder stone) and a discrete component (filler particles). Regulation of lightweight concrete properties is achieved by changing filler's porosity, the content and structure of composite material's matrix.

To increase the efficiency of lightweight concrete, it is important that structure's indicators (the size and nature of filler's particles distribution, the content of the matrix) provide high heat-shielding properties, the maximum value of elastic modulus of the composite material without loss of system connectivity [1–3].

The criterion for heat-shielding properties of materials is the coefficient of thermal conductivity, the values of which are determined instrumentally using devices of various modifications and calculation methods [4–7]. For many natural and artificial materials, the values of thermal conductivity coefficient were determined and given in the reference literature. To develop technology and improve the efficiency of composite materials of a combined structure with balanced mechanical and thermal insulation properties, it is necessary to predict thermal conductivity at the stage of composite development [8–10]. Therefore, analytical and numerical methods for determining this characteristic for a composite material are very relevant. Formulas for calculating the thermal conductivity coefficient of porous concrete are known [11–15]. The use of newly developed porous granular filler and matrix requires refinement of methodology for determining the thermal conductivity coefficient of lightweight concrete.

The aim of the work is to study the nature of the change in thermal conductivity and mechanical properties of a composite material based on granular porous filler by numerical methods.

Previously, authors had carried out numerical studies of the influence of porous filler's characteristics on composite material's strength properties. The paper [4] represents the results obtained using the Lira Sapr program, which makes it possible to study stress-strain state of systems taking into account the plastic and brittle deformation mechanisms. The studies made it possible to determine boundary values of filler's packing density, to identify critical situations leading to grains flattening. This work is continuation of research on composite materials.

## 1. Object and methods of research

The object of the study was a cementless composite material of a multilayer variotropic structure, made from molding sands containing various amounts of porous granular filler. Variotropic concrete is characterized by variable values of density and strength over the section of the moulded product, smooth transition of layers with structural properties into heat-insulating layers. Instrumental determination of the thermal conductivity of composite materials of this structure is difficult.

Here are some well-known analytical dependencies for determining the thermal conductivity coefficient, which are used both for homogeneous porous media and for heterogeneous systems, for example, concrete with porous granular filler. To calculate thermal conductivity of binary mixtures ($\lambda_{mix}$), consisting of continuous matrix (stone binder concrete) with a thermal conductivity coefficient of $\lambda_{mat}$ and discrete inclusions (concrete filler) with a thermal conductivity coefficient $\lambda_{fil}$, it is possible to use the formula of V.I. Odelevsky [4, 6, 8]. However, for calculation of concrete with high content of filler (for example, a large-pore structure), this formula is unacceptable.

Calculations by the method of Landau P.F. [4, 8, 16] for mixtures with the number of phases i, which occupy volumes Vi, provide an error of no more than 14% compared to the experimental data:

$$\lambda^{\frac{1}{3}}_{mix} = \sum_i V_i \lambda_i^{\frac{1}{3}}. \tag{1}$$

To determine thermal conductivity coefficient of a binary mixture with a matrix volume content $V_{mat}$ and filler volume content $V_{fil}$, the Burger formula is used [4, 8, 16], in which C is an empirical coefficient depending on distribution of phases in the system:

$$\lambda_{mix} = \frac{V_{mat}\lambda_{mat} + cV_{fil}\lambda_{fil}}{V_{mat} + cV_{fil}}. \tag{2}$$

The need to select the value of the coefficient C for each composition reduces universality of the formula (2). The value of empirical coefficient can be calculated by comparing the formula (2) with other mathematical models, for example, with the well-known Maxwell formula [17]:

$$\lambda_{mix} = \lambda_{mat}\left(\frac{\lambda_{fil} + 2\lambda_{mat} - 2V_{fil}(\lambda_{mat} - \lambda_{fil})}{\lambda_{fil} + 2\lambda_{mat} + V_{fil}(\lambda_{mat} - \lambda_{fil})}\right). \tag{3}$$

The solution of the system of equations (2) and (3) makes it possible to determine the value of the coefficient C:

$$C = V_{mat}\frac{V_{mix}\lambda_{mat}}{V_{fil}(\lambda_{mat} - \lambda_{mix})}. \tag{4}$$

Using the dependences according to formulas (1), (2) the coefficients of thermal conductivity are calculated for arbitrary concrete compositions that differ in the content and properties of the components (Table 1). The values of the coefficient C (Table 1) are determined using equation (4). Analysis of the calculation results indicates sensitivity of analytical methods to changes in the composition of concrete. However, the use of calculation methods has limitations. For example, for concretes with a matrix, the thermal conductivity of which is equal to or less than the thermal conductivity of the filler, the coefficient C takes values close to zero. This is not typical for real concrete structures.

Wide opportunities for modeling and predicting the properties of composite materials are provided by computer programs [18-21]. The finite element method implements the solution of stationary and non-stationary problems of thermal conductivity and thermoelasticity [22, 23]. For a flat system, it is efficient to use the Agros2D program (University of West Bohemia, Pilsen, Czech Republic), developed for calculating physical fields of various nature.

Numerical modeling of thermal conductivity was performed on the example of a composite material with porous granular filler. Two options for the structure of lightweight concrete were considered. The first option is a regular packing of filler particles of the same diameter, equal to 0.7 cm (Figure 1a). The second option is filler particles with diameters of 0.7 and 1.0 cm are distributed according to the law of an equilateral triangle (Figure 2a).

The method developed for numerical determination of thermal conductivity coefficient for the models under study is based on the well-known dependence relating the heat flux (q), the temperature of the outer surface of the layer ($tc_1$), the temperature of the inner surface of the layer ($tc_2$), the layer thickness ($\delta$) and the thermal conductivity of the layer ($\lambda$) [4, 6]:

$$q = \frac{\lambda \ (tc_1 - tc_2)}{\delta}. \tag{5}$$

Based on equation (5), the thermal conductivity of the layer is equal to:

$$\lambda = \frac{q \cdot \delta}{(tc_1 - tc_2)}. \tag{6}$$

Calculation results using the numerical method are shown in Table 1.

Calculations of composite material's mechanical characteristics were made for the structures of roof and ceiling under the distributed load $P = 10$ kN/m$^2$. The accepted value of load corresponds to the normative indicator of permanent and temporary load for standard prefabricated and monolithic reinforced concrete structures.

To assess the level of stresses in the model under study, the method recommended by the Construction Norms and Rules 2.03.01.84 «Concrete and reinforced concrete structures» was used. The bending moment, M, in the design section can be expressed in terms of the height of the concrete compression zone, determined by the parameter, $\alpha_R$, and the normal bending stresses in the concrete, $R_b$, and reinforcement, $R_{SC}$, by the formula:

$$M \leq \alpha_R R_b b \delta_0^2 + R_{SC} A_S' (\delta_0 - a'), \tag{7}$$

where, $\alpha_R$ is a coefficient equal to 0.4 for lightweight concrete; $R_b$ is design resistance of concrete; b is design width of the wall section, equal to 1 m; $\delta_0$ is the wall thickness of the coffered ceiling; $R_{SC}$ is design resistance of the reinforcement, equal to 355 MPa; $A_S'$ is cross-sectional area of reinforcement of the compressed belt; $a'$ is thickness of concrete cover.

For the model under study, the case is accepted when the effect of reinforcement in the compressed zone is not taken into account. In such a situation, from formula (7) for normal stresses, $\sigma$, the dependence is obtained:

$$\sigma = \frac{M_{max}}{\alpha_R b \delta_0^2} \leq R_b. \tag{8}$$

**Table 1.** Calculated values of thermal conductivity for concrete of various compositions.

| Number | Content of concrete components | | Thermal conductivity of concrete components, W/(m·⁰c) | | Thermal conductivity of concrete, calculated according to the formulas $\lambda$mix, W/(m·⁰C), | | | Coefficient C |
|---|---|---|---|---|---|---|---|---|
| | matrix, $V_{mat}$ | filler, $V_{fil}$ | matrix, $\lambda_{mat}$ | filler, $\lambda_{fil}$ | Landau | Burger | Numerical method | |
| 1 | 0.300 | 0.700 | 1.90 | 0.08 | 0.305 | 0.491 | 0.269 | 1.469 |
| 2 | 0.300 | 0.700 | 0.80 | 0.10 | 0.220 | 0.263 | 0.396 | 1.412 |
| 3 | 0.300 | 0.700 | 0.50 | 0.08 | 0.157 | 0.179 | 0.189 | 1.389 |
| 4 | 0.300 | 0.700 | 0.20 | 0.20 | 0.200 | 0.200 | 0.240 | 0.000 |
| 5 | 0.337 | 0.673 | 0.10 | 0.04 | 0,058 | 0.057 | 0.081 | 1.288 |
| 6 | 0.500 | 0.500 | 0.70 | 0.07 | 0.275 | 0.329 | 0.329 | 1.429 |
| 7 | 0.510 | 0.490 | 0.80 | 0.10 | 0.344 | 0.397 | 0.396 | 1.412 |
| 8 | 0.673 | 0.337 | 0.10 | 0,80 | 0,200 | 0.193 | 0.210 | 0.305 |
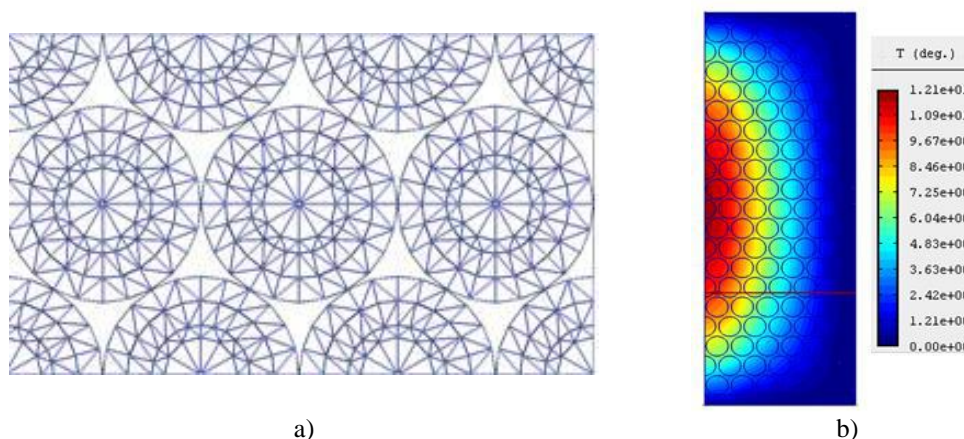
**Fig.1.** Model of a composite material with regular packing of granules of the same diameter:
a) layout of filler's particles; b) temperature fields obtained in the Agros2D program.
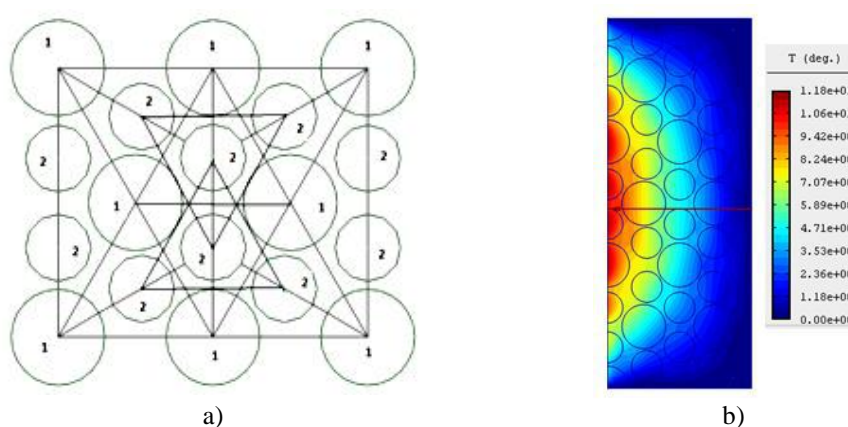


**Fig.2.** Composite material model with the packing of filler particles of different diameters according to the law of an equilateral triangle: a) arrangement of filler particles; b) temperature fields obtained in the Agros2D program.

## 2. Results and discussion

In accordance with the method developed, a flat layer was isolated in the form of a strip of length L with an aspect ratio $L/\delta>2$. A heat flux with intensity of $q = 100$ W/m$^2$ is set on one of the faces of the computational domain. The temperature T= 0 is set for the other three faces. As a result of the calculation, the values of the temperature distribution inside the layer and on the active surface of the layer, along which the heat flux is set, are obtained. Taking into account the given boundary conditions in formula (6), it is assumed that $tc_2 =T=0$.

Numerical calculations showed approximate correspondence between the obtained values of the thermal conductivity coefficient for both cases at equal values of $V_{mat}$, $V_{fil}$ and the corresponding thermal conductivity coefficients of the matrix and filler. Thermal protection layers with a thickness of 0.03 and 0.05 m were considered. The packing densities of the granules were controlled by assigning characteristics of the binder to some part of the filler. This made it possible to regulate the volume ratio of filler and matrix in the composite material. Figures 1b and 2b show the temperature fields obtained using the Agros2D program.

In the calculations, the ratio of the filler and matrix in the composite material was controlled by imparting the properties of the matrix material to some granules. In this way, the volume of the matrix was increased. It should be noted that the thermal conductivity coefficient of concrete with porous granules is almost three times lower than for the matrix material.

Numerical methods make it possible to compare the thermal efficiency of using multilayer shells made of different materials. Multilayer objects of traditional structure and those objects developed using composite materials with porous granular filler were used as a comparison [3, 24, 25].

The traditional object is represented by a three-layer shell with two outer layers of heavy concrete, thickness is $\delta_2 = \delta_3 = 0.04$ m, thermal conductivity is $\lambda_2 = \lambda_3 = 1.7$ W/(m·$^0$C); the central layer with a

.

thickness of $\delta_1 = 0.05 - 0.20$ m made of mineral wool with $\lambda 1 = 0.07$ W/(m·$^0$C). The object developed is a 20 cm thick five-layer shell made of a composite material with porous granular filler. Separate layers are made of composite materials with porous granular filler, which have a similar composition and differ in structure (Figure 3). The outer layers of the object developed have the following fixed parameters: thickness is $\delta_2* = \delta_3* = 0.04$ m, thermal conductivity of the layers is $\lambda_2* = 0.11$ W/(m·$^0$C) and $\lambda_3* = 0.13$ W/(m·$^0$C). The calculated thickness of the central layer ($\delta_1*$, m) with thermal conductivity of $\lambda_1* = 0.08$ W/(m·$^0$C) ensures that the thermal resistance of three-layer and five-layer shells is the same (Table 2). Assuming that the values of thermal resistance on the boundary surfaces of both compared shells are the same, we obtain:

$$r = \sum_{i=1}^{5} \frac{\delta_i^*}{\lambda_i^*} = \sum_{i=1}^{3} \frac{\delta_i}{\lambda_i} . \qquad (9)$$

**Table 2.** Parameters of models of multilayer shells made of materials of various compositions and structures.

| Number | Five-layer shell made of composite material with variotropic structure | | | | | | | Three-layer shell made of heavy concrete and mineral wool | | | | |
|---|---|---|---|---|---|---|---|---|---|---|---|---|
| | $\lambda_1^*$, W/(m·$^0$C) | $\delta_1^*$, m | $\lambda_2^*$, W/(m·$^0$C) | $\delta_2^*$, m | $\lambda_3^*$, W/(m·$^0$C) | $\delta_3^*$, m | $\sum \delta_i^*$, m | $\lambda_1$, W/(m·$^0$C) | $\delta_1$, m | $\lambda_2$, W/(m·$^0$C) | $\delta_2$, m | $\sum \delta_i$, m |
| 1 | 0.08 | 0.000 | 0.11 | 0.04 | 0.13 | 0.04 | 0.160 | 0.07 | 0.05 | 1.7 | 0.04 | 0.130 |
| 2 | 0.08 | 0.000 | 0.11 | 0.04 | 0.13 | 0.04 | 0.160 | 0.07 | 0.08 | 1.7 | 0.04 | 0.160 |
| 3 | 0.08 | 0.020 | 0.11 | 0.04 | 0.13 | 0.04 | 0.180 | 0.07 | 0.10 | 1.7 | 0.04 | 0.180 |
| 4 | 0.08 | 0.050 | 0.11 | 0.04 | 0.13 | 0.04 | 0.210 | 0.07 | 0.12 | 1.7 | 0.04 | 0.200 |
| 5 | 0.08 | 0.085 | 0.11 | 0.04 | 0.13 | 0.04 | 0.245 | 0.07 | 0.15 | 1.7 | 0.04 | 0.230 |
| 6 | 0.08 | 0.146 | 0.11 | 0.04 | 0.13 | 0.04 | 0.306 | 0.07 | 0.20 | 1.7 | 0.04 | 0.280 |
| 7 | 0.08 | 0.000 | 0.11 | 0.04 | 0.13 | 0.04 | 0.160 | 0.07 | 0.05 | 1.7 | 0.04 | 0.130 |
| 8 | 0.08 | 0.056 | 0.11 | 0.04 | 0.13 | 0.04 | 0.216 | 0.07 | 0.08 | 1.7 | 0.04 | 0.160 |
| 9 | 0.08 | 0.096 | 0.11 | 0.04 | 0.13 | 0.04 | 0.256 | 0.07 | 0.10 | 1.7 | 0.04 | 0.180 |
| 10 | 0.08 | 0.136 | 0.11 | 0.04 | 0.13 | 0.04 | 0.296 | 0.07 | 0.12 | 1.7 | 0.04 | 0.200 |
| 11 | 0.08 | 0.196 | 0.11 | 0.04 | 0.13 | 0.04 | 0.356 | 0.07 | 0.15 | 1.7 | 0.04 | 0.230 |
| 12 | 0.08 | 0.296 | 0.11 | 0.04 | 0.13 | 0.04 | 0.456 | 0.07 | 0.20 | 1.7 | 0.04 | 0.280 |
| 13 | 0.08 | 0.012 | 0.11 | 0.00 | 0.13 | 0.04 | 0.092 | 0.07 | 0.05 | 1.7 | 0.04 | 0.130 |
| 14 | 0.08 | 0.046 | 0.11 | 0.00 | 0.13 | 0.04 | 0.126 | 0.07 | 0.08 | 1.7 | 0.04 | 0.160 |
| 15 | 0.08 | 0.069 | 0.11 | 0.00 | 0.13 | 0.04 | 0.149 | 0.07 | 0.10 | 1.7 | 0.04 | 0.180 |
| 16 | 0.08 | 0.092 | 0.11 | 0.00 | 0.13 | 0.04 | 0.172 | 0.07 | 0.12 | 1.7 | 0.04 | 0.200 |
| 17 | 0.08 | 0.126 | 0.11 | 0.00 | 0.13 | 0.04 | 0.206 | 0.07 | 0.15 | 1.7 | 0.04 | 0.230 |
| 18 | 0.08 | 0.183 | 0.11 | 0.00 | 0.13 | 0.04 | 0.263 | 0.07 | 0.20 | 1.7 | 0.04 | 0.280 |
| 19 | 0.08 | 0.055 | 0.11 | 0.00 | 0.13 | 0.04 | 0.135 | 0.07 | 0.05 | 1.7 | 0.04 | 0.130 |
| 20 | 0.08 | 0.115 | 0.11 | 0.00 | 0.13 | 0.04 | 0.195 | 0.07 | 0.08 | 1.7 | 0.04 | 0.160 |
| 21 | 0.08 | 0.155 | 0.11 | 0.00 | 0.13 | 0.04 | 0.235 | 0.07 | 0.10 | 1.7 | 0.04 | 0.180 |
| 22 | 0.08 | 0.195 | 0.11 | 0.00 | 0.13 | 0.04 | 0.275 | 0.07 | 0.12 | 1.7 | 0.04 | 0.200 |
| 23 | 0.08 | 0.255 | 0.11 | 0.00 | 0.13 | 0.04 | 0.335 | 0.07 | 0.15 | 1.7 | 0.04 | 0.230 |
| 24 | 0.08 | 0.355 | 0.11 | 0.00 | 0.13 | 0.04 | 0.435 | 0.07 | 0.20 | 1.7 | 0.04 | 0.280 |

For multilayer materials, the balance of heat-shielding and mechanical characteristics is important. Behavior of the studied materials in shells (Figure 3a) and pan floor (Figure 4) has been considered.

We take the thickness of individual layers $\delta_i* \leq 0.04$ m. From here, we can find the thickness of the variable central highly porous layer of the five-layer shell, which plays the main role in the thermal insulation of the five-layer model (Table 2).

Positions 13 – 24 of Table 2 reflect the properties of a five-layer model, in which one of the layers with the thermal conductivity coefficient of $\lambda_2* = 0.11$ W/(m·$^0$C) has a thickness of $\delta_2* = 0$. In this case, the

total thickness of the multilayer shell can be reduced without significant change values of the thermal conductivity coefficient.



a)                                                                    b)
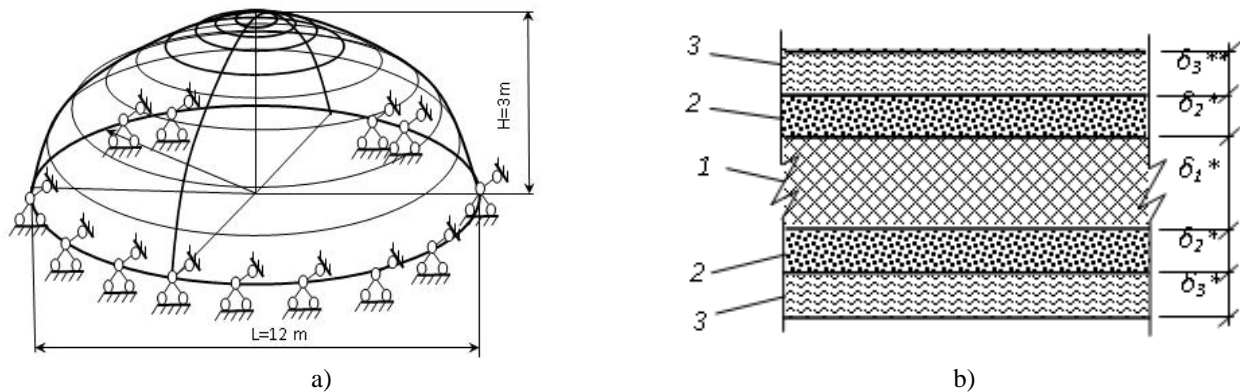
**Fig.3.** Five-layer model for the shell: a) shell structure; b) the structure of a five-layer material (1 – central layer; 2 – middle layers; 3 – surface layers).
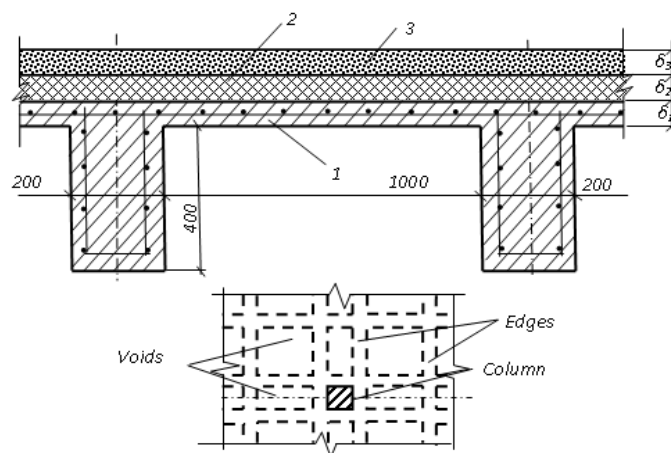


**Fig.4.** Pan floor: 1− heavy layer concrete; 2 – a layer of heat-insulation material; 3 – top protective layer.

Figures 5 and 6 illustrate the efficiency of using composite materials based on granular porous filler in the various types of floors. In numerical studies, the calculated vertical uniformly distributed load of $P = 10$ kN/m$^2$ was adopted on the walls of the shell and the pan floor. Strength calculations were performed by the finite element method in SCAD Office program using a multilayer shell finite element [22, 23]. Calculations confirm the advantages of using multilayer models of composite materials based on granular porous filler. Calculations show that the shell wall is subjected mainly to normal stresses; bending moments in the structure are small and can be neglected. Analysis of normal stress isofields (Figure 5a−b) indicates that the level of normal maximum stresses in a five-layer model made from composite material is three times lower than for a three-layer model of the same thickness. The level of vertical movements for the models compared is approximately equivalent and corresponds to the scheme (Figure 5c).

According to the calculations, the wall of the pan floor works in bending. The normal stresses in the wall are determined by the values of maximum bending moments. The use of a five-layer composite material in insulating layers (Figure 4) makes it possible to reduce the level of maximum bending moments by 25%; accordingly, the level of normal stresses will decrease by 25% compared to the three-layer model (Figure 6).

At the same time, vertical displacements are reduced by 20%, which is due to the increased deformability of the central layer and the violation of uniformity of the wall material made using a soft heat-insulating layer. To calculate the normal stresses, σ, using formula (8) from Figure 6c, it is assumed that the maximum bending moment for a five-layer model of a caisson slab 1 m wide is $M_{max}= 0.04$ t·m $= 0.04 \cdot 10^3$ kg·m.

a)                                                    b)

c)
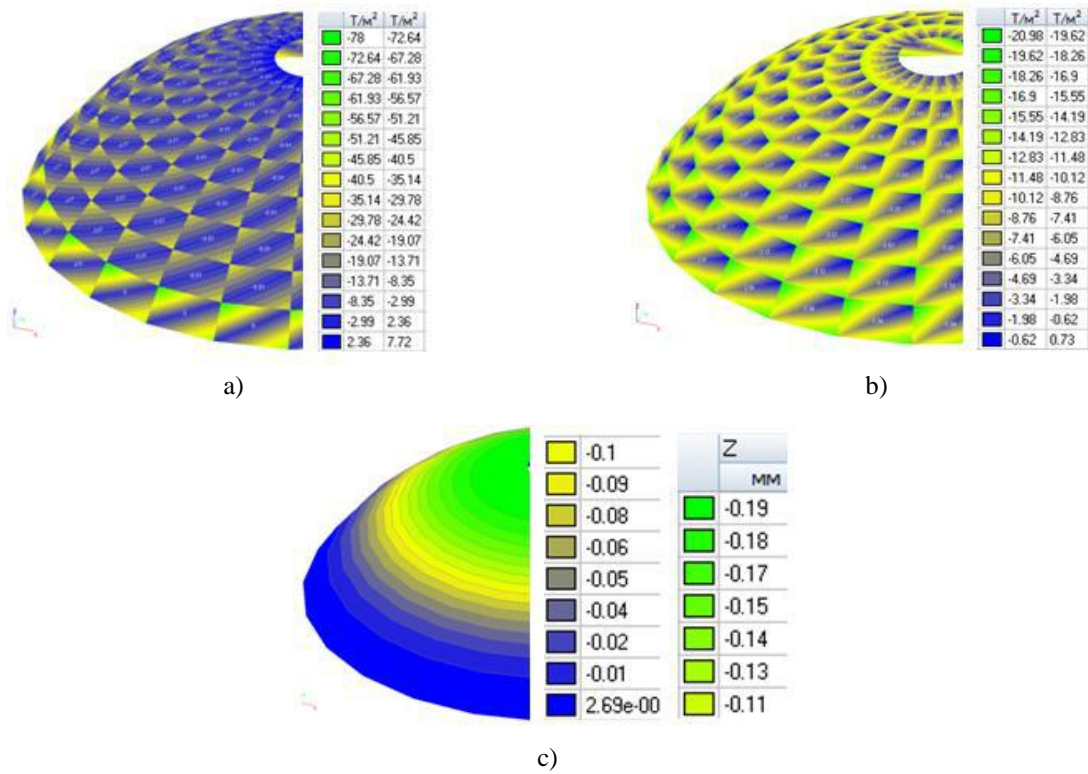
**Fig.5.** Stress and strain isofields in the shell: a) normal stresses in a three-layer shell with a central layer of mineral wool; b) normal stresses in a five-layer composite shell; c) vertical movements in a three-layer shell.



a)                                                    b)

c)                                                    d)
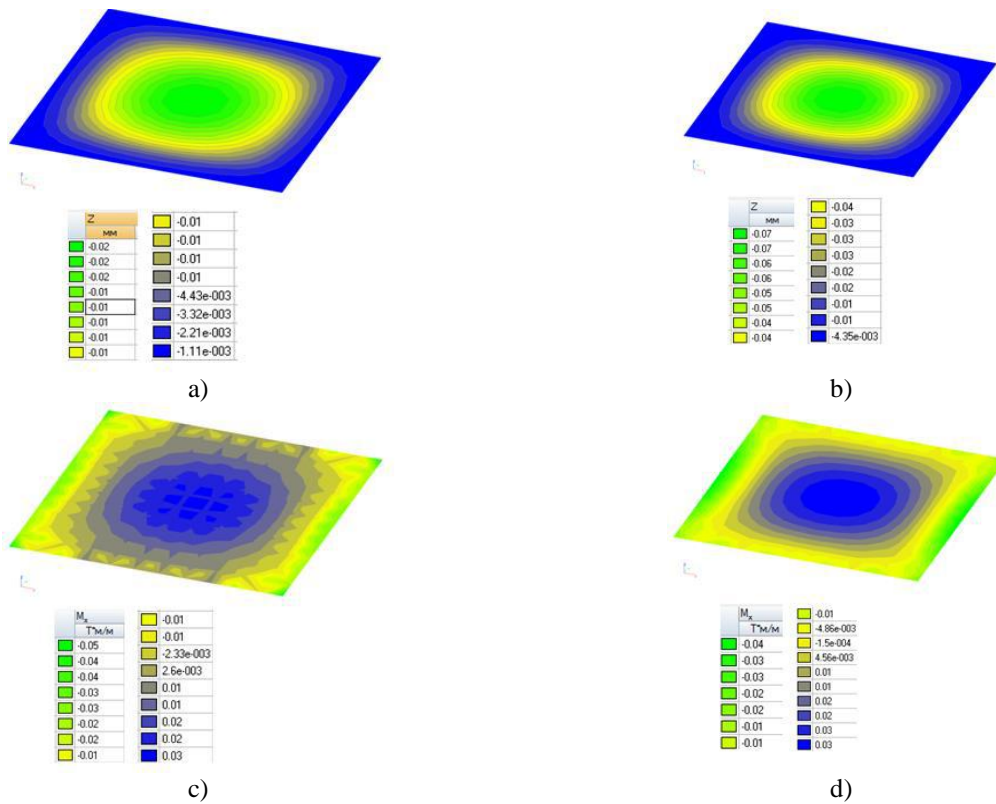
**Fig.6.** Isofields of stresses and deformations in the wall of the pan floor: a) displacement isofields in a five-layer wall made from a composite material based on porous filler; b) displacement isofields in a three-layer wall based on mineral wool; c) isofields of bending moments in a five-layer wall made from composite material based on porous filler; d) isofields of bending moments in a three-layer wall based on mineral wool.

For the situation described in line 14 (Table 2), only one layer with a thickness of $\delta_0 = 0.126 - 0.03 = 0.096$ m $= 9.6$ cm is accepted with a margin of safety:

$$\sigma = \frac{0.04 \cdot 10^3}{0.4 \cdot 10^2 \cdot 9.6^2} = 0.0108\,\text{kN}/\text{cm}^2 = 0.11\,\text{MPa} \leq R_b.$$

According to building codes, the ultimate resistance of lightweight concrete of strength classes B2.5 − B12.5 varies from 0.18 to 0.59 MPa. Therefore, the necessary strength of the layer is provided. The calculated characteristics correspond with the results of experimental studies of composite materials [26].

## Conclusion

Results of numerical studies made it possible to determine the nature of the change in heat-shielding and mechanical properties of multilayer materials and draw the following conclusions.

1. A technique for numerical determination of the thermal conductivity coefficient of a multilayer composite material with a variotropic structure based on porous granular filler has been developed. The results obtained correspond to the values obtained with the help of analytical dependencies.

2. The results of computer-aided design obtained for a flat model are in line with the data of an analytical calculation of composite materials' thermal conductivity coefficient for three-dimensional models.

3. Behavior of a composite material based on porous granular filler was studied by numerical methods in a spherical shell and a pan floor wall. The resulting stress and strain's isofields are comparable to the corresponding fields for a three-layer model containing dense load-bearing layers of heavy concrete and a central heat-insulating layer of mineral wool.

4. It has been revealed that with the same thermal characteristics and almost the same total thickness, the level of stresses and deformations in a multilayer shell made of a composite material based on porous granular filler is significantly lower than in a three-layer model made using heavy concrete. This is due to the absence of variotropic structure of abrupt change in layers' stiffness in the composite material, which is characteristic of a three-layer model of materials of different nature.

5. Computer simulation methods make it possible not only to predict technical characteristics of multicomponent systems, but also to carry out targeted development of effective composite materials with the desired properties.

## REFERENCES

1  Lu J.-X., Shen P., Asad H., Chi A., Poon S. Development of high performance, lightweight concrete using ultra high performance, cementitious composite and different lightweight aggregates. *Cement and Concrete Composites,* 2021, Vol. 124, No. 104277. doi:10.1016/j.cemconcomp.2021.104277

2  Mo K.H., Hussein M.N., Ling T.-C., et al. Development of lightweight aggregate mortar skin layer for an innovative sandwich concrete composite. *Journal of Building Engineering*, 2020, Vol. 27, No. 100941. doi:10.1016/j.jobe.2019.100941

3  Miryuk O. Porous composite material based on liquid glass. *Complex Use of Mineral Resources*, 2022, Vol. 323, No. 4, pp. 15 – 22. doi:10.31643/2022/6445.35

4  Korotkikh A.G. *Thermal conductivity of materials*, Tomsk, Publishing House of Tomsk Polytechnic University, 2011, 97 p. [in Russian]

5  Yesbaev A.N., Yessenbayeva G.A., Ramazanov M.I. Investigation of the model for the essentially loaded heat equation. *Eurasian Physical Technical Journal*. 2019, Vol. 16, No. 1(31), pp. 113-120. doi:10.31489/2019No1/113-120

6  Zhirov С.Г., Koptelov A.A., Milekhin Yu.M. Thermal conductivity of heterogeneous materials. Part II. Method for calculating thermal conductivity of heterogeneous materials with interpenetrating components. *Applied physics*, 2005, No. 4**.** pp. 39 – 43. [in Russian]

7  Merzadinova G.T., Sakipov K.E., Sharifov D.M., Mirzo A., Bekishev A.Z. Laser photoacoustic method for determining the coefficients of thermal conductivity and thermal conductivity of materials. *Eurasian Journal of Physics and Technology*, 2019, Vol. 16, No. 1, pp. 94 – 98. http://rep.ksu.kz//handle/data/9344

8  Sulaberidze V.Sh., Skorniakova E.A. Estimation of Thermal Conductivity Calculation Model Parameters for Composite Materials with a Polymer Binder Based on Experimental Data. *Vestnik of Nosov Magnitogorsk State Technical University,* 2020, Vol. 18, No. 4, pp. 57 – 64. [in Russian]

9    Remesar J.C., Simon F., Vera S., Lopez M. Improved balance between compressive strength and thermal conductivity of insulating and structural lightweight concretes for low rise construction. *Construction and Building Materials*, 2020, Vol. 247, No. 118448. doi:10.1016/j.conbuildmat.2020.118448

10    Malachanne E., Cassidy R., Garcia-Diaz E., Dubois F. Numerical model for mechanical behavior of lightweight concrete and for the prediction of local stress concentration. *Construction and Building Materials*, 2014, Vol. 59, pp. 180 – 187. doi:10.1016/j.conbuildmat.2014.01.067

11    He F., Wang Y., Zheng W., Wu J.-Y., Huang Y.-H. Effective thermal conductivity model of aerogel thermal insulation composite. *International Journal of Thermal Sciences*, 2022, Vol. 179, No. 107654. doi:10.1016/ j.ijthermalsci.2022.107654

12    Tian S.-Q., Yu S.-F., Wang X., Fan L.-W., Yu Z.-T., Xu X., Ge J. Experimental determination and fractal modeling of the effective thermal conductivity of autoclave aerated concrete (AAC) impregnated with paraffin for improved thermal storage performance. *Applied Thermal Engineering*, 2019, Vol. 163, No. 114387. doi:10.1016/j.applthermaleng.2019.114387

13    Wu X., Wang S., Yang J., Zhao J., Chang X. Damage characteristics and constitutive model of lightweight shale ceramsite concrete under static-dynamic loading. *Engineering Fracture Mechanics*, 2022, Vol. 259, No. 108137. doi:10.1016/j.engfracmech.2021.108137

14    Wang Y., Ma C., Liu Y., et al. A model for the effective thermal conductivity of moist porous building materials based on fractal theory. *International Journal of Heat and Mass Transfer*, 2018, Vol. 125, pp. 387 – 399. doi:10.1016/j.ijheatmasstransfer.2018.04.063

15    Song G., Wang L., Deng L., Yin H.M. Mechanical characterization and inclusion, based boundary element modeling of lightweight concrete containing foam particles. *Mechanics of Materials*, 2015, Vol. 91, pp. 208 – 225. doi:10.1016/j.mechmat.2015.07.014

16    Galkin A., Zheleznyak M., Zhirkov A. Increasing thermal stability of the roads in cryolithic zone. *Transportation Research Procedia*, 2022, Vol. 63, pp. 412– 419. doi:10.1016/j.trpro.2022.06.029

17    Xu J.Z., Gao B.Z., Kang F.Y A Reconstruction of Maxwell Model for Effective Thermal Conductivity of Composite Materials. *Applied Thermal Engineering*, 2016, Vol. 102. No. 6, pp. 972 – 979. doi:10.1016/j.applthermaleng.2016.03.155

18    Quan W.,Ma X.,Li X.,Dong Z. Efficient numerical model for effective thermal conductivity of concrete with aggregates of different morphologies and imperfect interfaces. *International Journal of Heat and Mass Transfer*, 2022, Vol. 185, No. 122358. doi:10.1016/j.ijheatmasstransfer.2021.122358

19    RenY., Yu Z., Huang Q., Ren Z. Constitutive model and failure criterions for lightweight aggregate concrete: A true triaxial experimental test. *Construction and Building Materials*, 2018, Vol. 171, pp. 759 – 769. doi:10.1016/j.conbuildmat.2018.03.219

20    Sadrmomtazi A., Sobhani J., Mirgozar M.A. Modeling compressive strength of EPS lightweight concrete using regression, neural network and ANFIS. *Construction and Building Materials*, 2013, Vol. 42, pp. 205 – 216. https://doi.org/10.1016/j.conbuildmat.2013.01.016

21    Sun X., Liao W., Kumar A., et al. Multi-level modeling of thermal behavior of phase change material incorporated lightweight aggregate and concrete. *Cement and Concrete Composites*, 2021, Vol. 122, No. 104131. doi:10.1016/j.cemconcomp.2021.104131

22    Elshahawi M., Hückler A., Schleich M. Constitutive relations and finite element modeling of Infra Lightweight Concrete (ILC). *Journal of Building Engineering*, 2022, Vol. 48, No. 103869. doi:10.1016/ j.jobe.2021.103869

23    Mishra R., Behera B.K., Muller M., Petru M. Finite element modeling based thermodynamic simulation of aerogel embedded nonwoven thermal insulation material. *International Journal of Thermal Sciences*, 2021, Vol. 164, No. 106898. doi:10.1016/j.ijthermalsci.2021.106898

24    Miryuk O., Fediuk R., Amran M. Foam Glass Crystalline Granular Material from a Polymineral Raw Mix. *Crystals,* 2021, Vol. 11, No. 1447. doi:10.3390/cryst11121447

25    Miryuk O. Liquid-glass concrete of variable density. *IOP Conference Series: Materials Science and Engineering*, 2020, Vol. 869, No. 032025. doi:10.1088/1757-899X/869/3/032025

26    Miryuk O., Fediuk R., Amran M. Porous Fly Ash /Aluminosilicate Microspheres-Based Composites Containing Lightweight Granules Using Liquid Glass as Binder. *Polymers,* 2022, Vol. 14(17), No. 3461. doi:10.3390/polym14173461

# ALGORITHM FOR FINDING MAXIMUM POWER POINT TRACKING WHEN SHADOWING OR FAILURE OF SOLAR PANEL PHOTO CELLS ON SATELLITES USING LOW ORBITS

Syzdykov A.B.[1], Baktybekov K.S.[2], Messerle V.E.[3], Komarov F. F.[4], Askaruly R.[1], Zilgarinov D.[1], Murat A.[1]

[1] JSC "National Company "Kazakhstan Gharysh Sapary", Astana, Kazakhstan, e-mail: a.syzdykov@gharysh.kz

[2] "Ghalam" LLP, Astana, Kazakhstan,

[3] Al-Farabi Kazakh National University, Almaty, Kazakhstan

[4] Belarusian State University, Minsk, Belarus

*Solar cell shading or the failure of several photocells changes the output current-voltage characteristic. This paper discusses an algorithm for approaching and searching the maximum power generated on board the spacecraft, which is all-important for fast charging of the secondary sources of electrical energy since the time spent on the sunny side in low orbits are limited by time. Currently, algorithms for finding maximum power work in ideal cases, and simple and effective algorithms are needed in cases of solar panel shading or failure of photocell/cells. In this paper, a simulation of a solar panel in various conditions is carried out. An algorithm for constructing the output volt ampere characteristics of a solar cell and a solar panel is implemented. Experiments of various algorithms on real devices have also been carried out.*

***Keywords:*** Maximum power point tracking, Python, current, voltage, failure, shadowing effect, power supply system

## Introduction

The number of satellites in low earth orbit is growing every year and will reach 100,000 satellites by 2030 [1]. The size of satellites is decreasing due to the development of technologies in the field of electronics, but the energy needs of the spacecraft are increasing due to the increase in the flight task. There is also a growing number of radar satellites that use an active payload and their consumption is much higher than that of optical spacecraft. Satellites in low orbits have a limited amount of time on the sunny side, so the challenge is to speed up the charge of the battery while passing through the consecrated part of the satellite's orbit [2]. The spacecraft power supply system uses two types of charge: direct energy transfer (DET-Direct Energy Transfer) [3]; maximum power point tracking (MPPT) method [4]. Direct Power Transfer - Without the usage of converters or regulators, power from the solar panel is sent directly to loads.

To select the optimal power from the solar panel, which depends on various parameters of the satellite, such as the angle of inclination of the solar panel relative to the sun, the temperature on the solar cells, efficiency, which is an integral parameter, service life and other criteria, the spacecraft power supply system uses the method of tracking the maximum power.

Solar cells often fail on spacecraft and for this purpose the MPPT search algorithm is needed. For shading cases, there are currently algorithms (MPPT algorithms for partial shading conditions) such as meta-heuristics, fuzzy logic based methods, numerical and mathematical application methods, hardware and modified conventional methods and etc. The onboard computer of the spacecraft is limited in computing power and the above algorithms require a lot of computing power. The developed algorithm reduces the load on the onboard computer.

## 1. Implementation of these algorithms on satellites KazEOSat - 1 and KazEOSat – 2

At the moment, JSC "National Company "Kazakhstan Gharysh Sapary" operates two optical remote sensing satellites KazEOSat - 1 - high resolution and KazEOSat - 2 - medium resolution, which is part of the space system of the Republic of Kazakhstan. The KazEOSat - 1 has a power supply system, which is

implemented using direct energy transfer technology (DET) and the electrical architecture of the spacecraft is shown in Figure 1. The PCDU is a power control and distribution unit that uses a direct energy transfer system. The solar array generates energy, which is sent to the PCDU to charge the battery and supplies subsystems of the spacecraft with power:
- Onboard computer;
- Communication system (S-band and X-band);
- Attitude and orbit control system (reaction wheels, star tracker, GPS module, magnitorque and etc.).
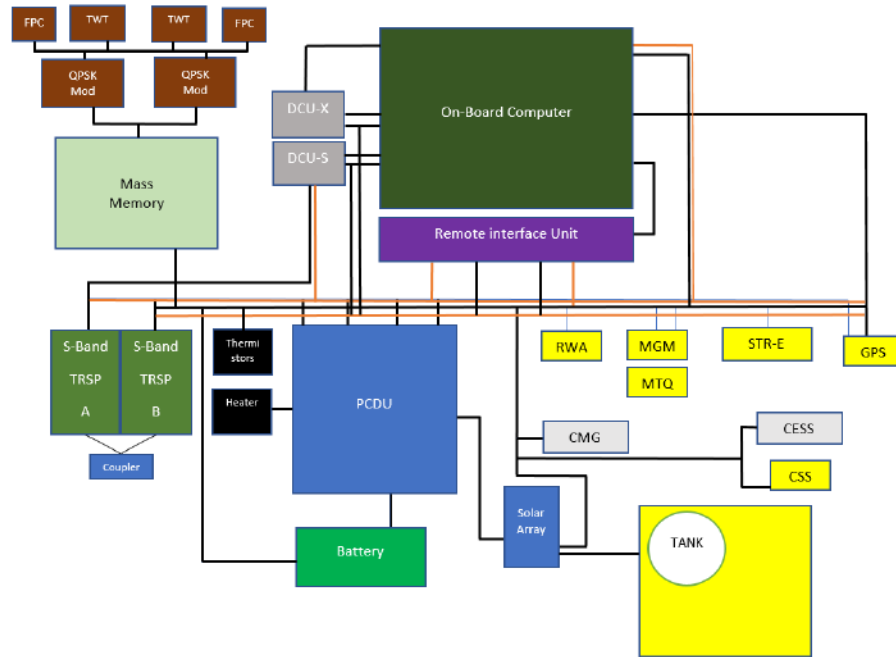


**Fig.1.** Electrical architecture of the KazEOSat -1.

The KazEOSat-2 satellite power supply system is shown in Figure 2, this spacecraft has an MPPT charge system [5].
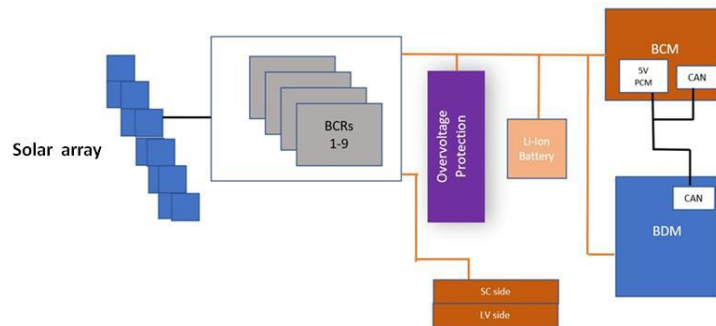


**Fig.2.** Electrical architecture of the KazEOSat – 2.

On the satellite KazEOSat - 2, the solar array generates an electric current, which is directed to the battery charge regulator (BCR), BCR has the MPPT algorithm installed. Further, the current with maximum power charges the battery and part of the energy is directed to the energy distribution module.

## 2. MPPT algorithms (methods)

There are numerous MPPT methods available at the moment for locating a spot with the greatest power. The most popular ones are:
- Perturb and observe method (P-&-O) [6];

- Incremental conductance method (IC) [7];
- Current sweep method (CS) [8];
- Constant voltage method (CV) [9];
- Temperature method [10].

Currently, satellites use the P-&-O method and the IC Method, since these algorithms are more stable in finding MPPT. These algorithms have been modeled in Python for a photocell and a solar panel. The photocell's electrical circuit is shown in Figure 3 [11 - 12].
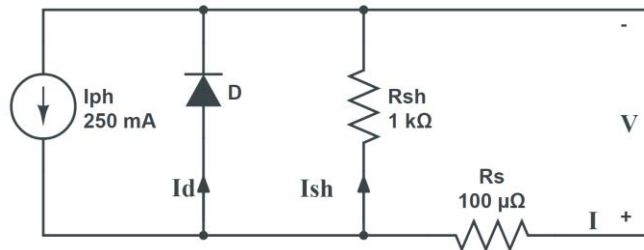


**Fig.3.** The electrical circuit of the photocell.

The code is implemented in Python [13] for simulating a solar cell at various incident light intensities and temperatures in the form of a diagram shown in Figure 4.
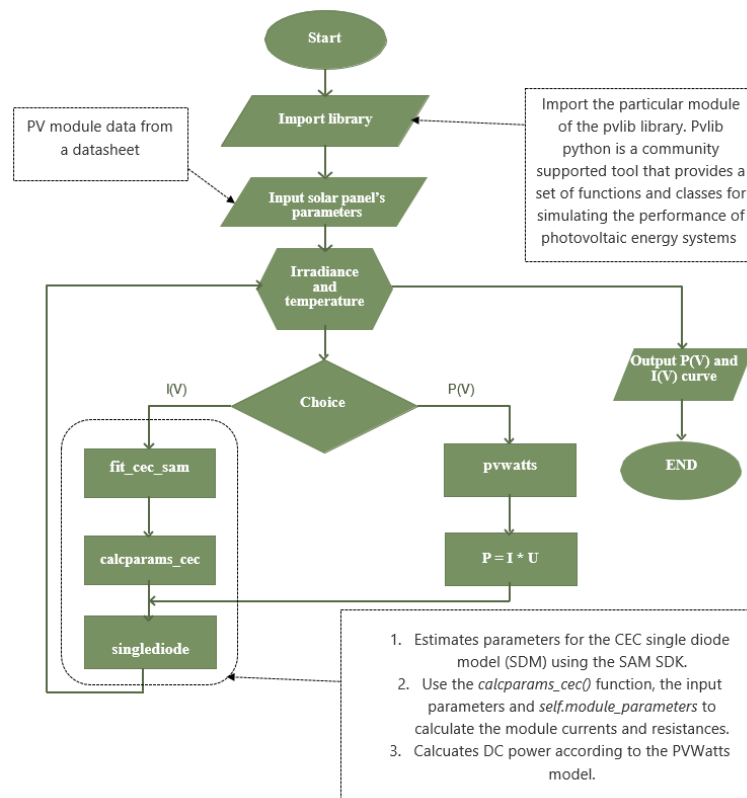


**Fig.4.** The python code algorithm for solar panels in the form of the diagram

The relationship between current and voltage in proportion to light intensity is seen in Figure 5. Figure 6 is showed the simulation results of the dependence between voltage and current at different temperatures on a photovoltaic cell. Figure 7 is showed the dependence of the maximum power and voltage on the different angles.

.
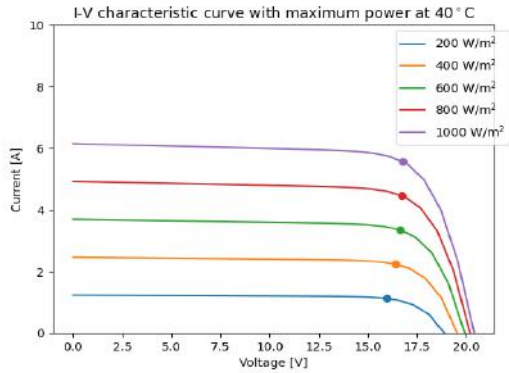
**Fig.5.** The relationship between current and voltage about light intensity.
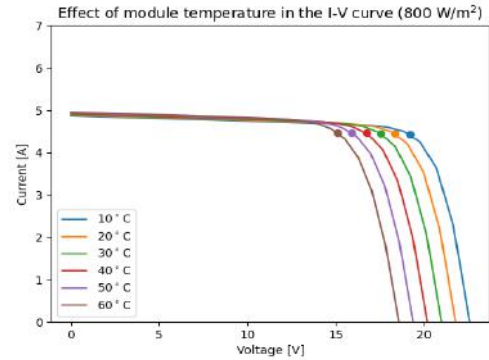


**Fig.6.** Simulation results of dependence between voltage and current at different temperatures
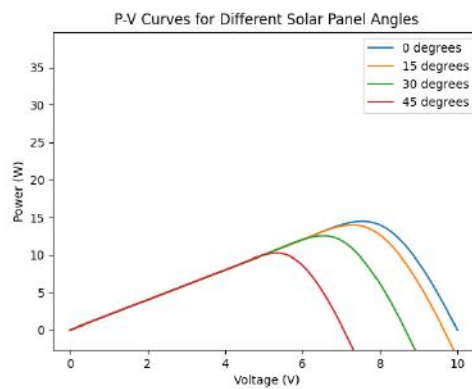


**Fig.7.** Simulation results of dependence of the maximum power and voltage on the different angles

Figure 8 presents the electrical circuit to simulate the solar panel [14 - 15].
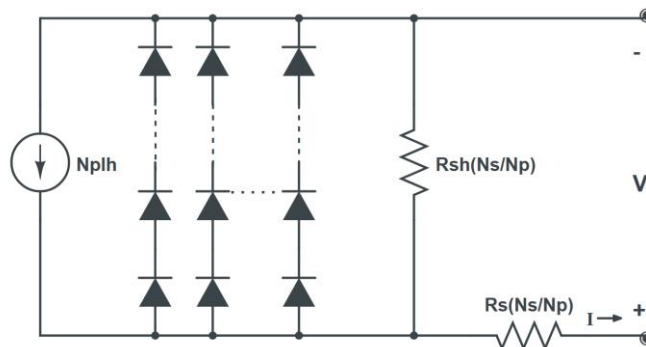


**Fig.8.** The electrical circuit of the solar panel.

Simulation outcomes are shown in Figure 9, which shows the dependence of current on voltage and power on voltage. These graphs are obtained by simulating the solar panel, under conditions when all photocells are working properly. The dependence of current on voltage is shown in Figure 9 a) and Figure 9 b) shows the curve of power on voltage.

Experiments were also carried out with real devices for the implementation of MPPT algorithms. A power board and a controller that is developed using the high-performance automotive grade microcontroller (TMS 470) make up the hardware and software complex for optimizing the search and selection of the greatest output power from the primary sources of satellites.
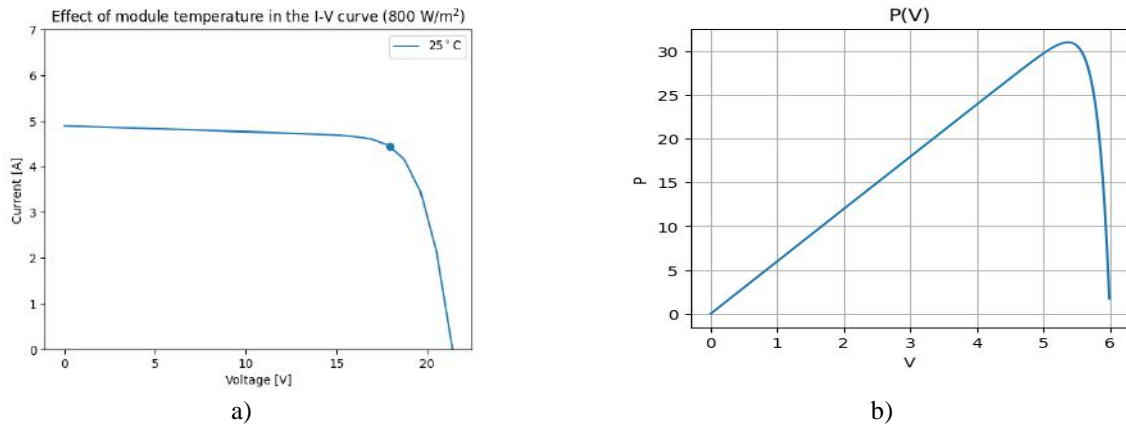
Fig.9. The results of the simulation of the solar panel.

Figure 10 depicts the power board which was made with the help of the CADSTAR software, which is used to design printed circuit boards. A Gerber file that comprises numerous topological elements was created for the fabrication of printed circuit boards. Figure 11 shows the TMS 470, which realizes algorithms to find MPPT.
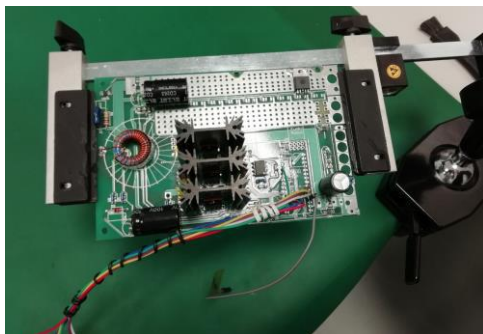


Fig.10. The power board.



Fig.11. The TMS 470.

The MPPT controller measures current, voltage, and battery voltage. The algorithm for determining the maximum power point then generates a PWM signal to create a duty cycle using the control of MOSFETs based on the input data.  The MPPT controller's operation is based on locating the solar panel's maximum power point. The following factors influence where the maximum power point is located: Environment temperature; Solar panel lighting.

The power board assembly, TMS 470, electronic load, and power source are all depicted in Figure 12. On this assembly, all electrical testing has been performed. The results of defining the maximum power of the assembled devices are shown in Figure 13.



Fig.12. The assembly of controller and power boards.
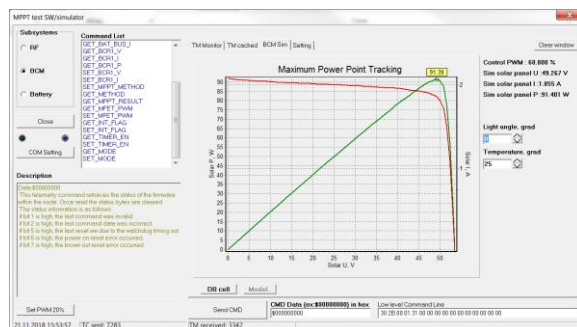


Fig.13. The results of the assembled devices.

Used algorithms search for maximum power and charge the spacecraft battery with the appropriate current and voltage, which is equal to the MPPT. The algorithms find the pick of power when the solar panel is not shaded or there is no photocell/cells failure.

## 3. MPPT algorithm for shading or failure of a photocell/cells

The satellite's solar panel may be obscured by the structure or the solar array elements may fail. Robust algorithms are needed that work in all cases, including the worst. This article shows a solution for finding the MPPT when a panel is shaded or a photocell or multiple elements fail. In these cases, the panel has different current-voltage characteristics, which are shown in Figures 14 and 15.
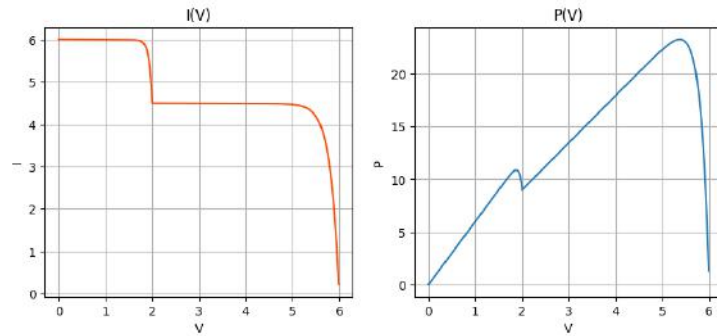


**Fig.14.** The results of shaded or a photocell or multiple elements fail.
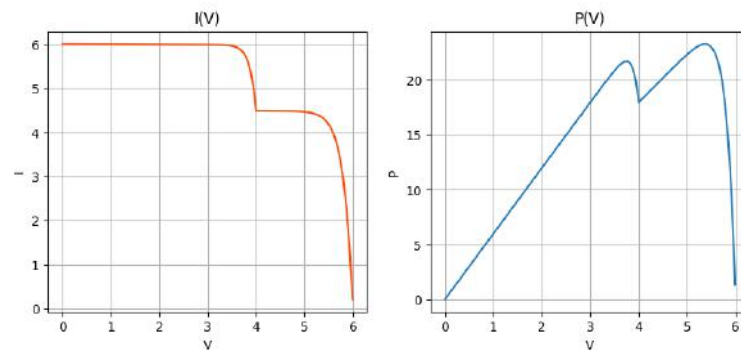


**Fig.15.** The results of shaded or failure of a photocell/cells.

Figure 16 a) corresponds to the results in figure 14. Figure 16 b) corresponds to the results in figure 15.



a)                                    b)
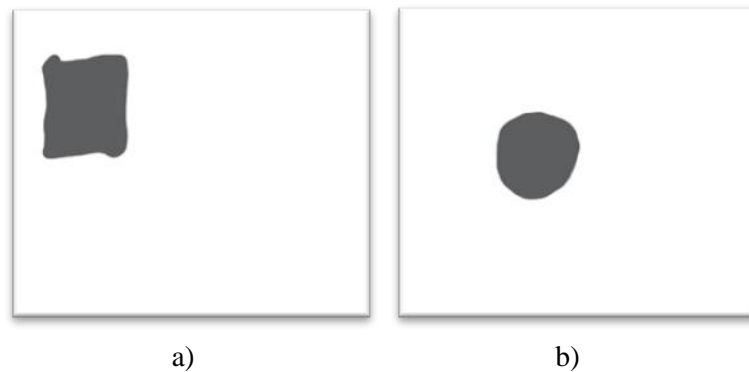
**Fig.16.** Shaded or failure sectors in the solar panel

The foregoing algorithms for discovering MPPT start to fail when shading or failure of the photocell/cells in Figure 14 and 15 occur because numerous maxima arise, and there is no longer a search for the global maximum that is required for quick secondary source of charging. Nowadays, there are algorithms for finding MPPT during shading and failure photocell/cells, but they are very difficult to implement and put a lot of load on the controller when searching [16 - 17]. Figure 17 shows the implementation of the methods for finding the maximum power in the event of darkening or loss of photocells.
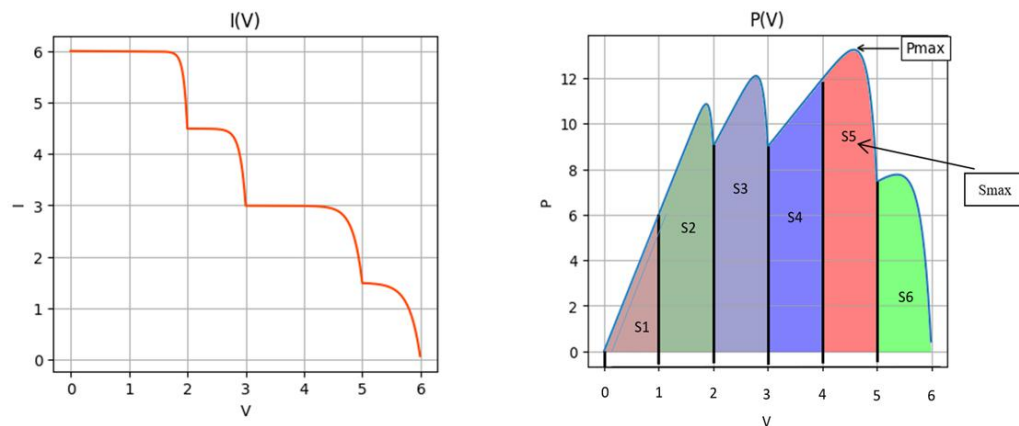


**Fig. 17.** MPPT algorithm in case of darkening or loss of an element/elements

The implementation of finding the MPPT in cases of shading or loss of photocells is shown in Figure 18. According to Figure 17, the voltage axis is divided into equal parts by steps that are multiples of the open circuit voltage of the solar cell or cells linked in series.
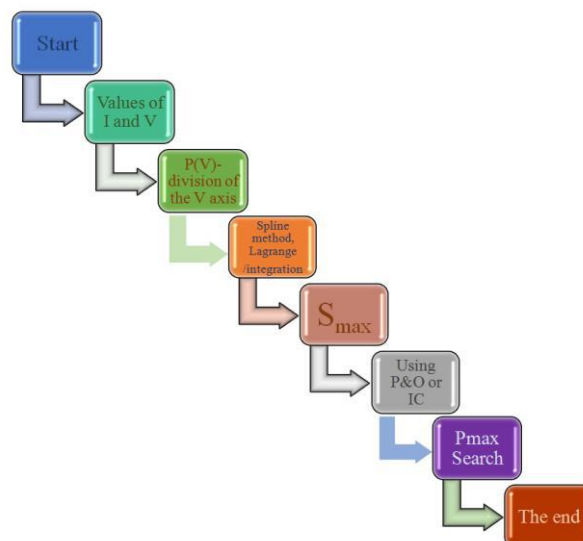


**Fig. 18.** Algorithm to find MPPT for worse case

The function will then be recovered using interpolation techniques (such as splines [18], Lagrange polynomials [19], etc.). The area of each graph segment will be calculated using integration. The largest area is determined by comparing the areas to one another. The MPPT is established in the region where the maximum area is established utilizing the P-&-O or IC methods.

## Conclusion

In the event of darkening or photoconverter failure, algorithms for determining the MPPT were examined. The proposed MPPT search algorithm uses minimal mathematical formulas that will not load the controller's work. And this algorithm can be used on board the spacecraft without taking into account temperature changes on the solar battery and also the period of active existence. As a result of the analysis of the literature, it can be concluded that the proposed solution is relevant, optimal and will be used in future missions on spacecraft, as well as on ground-based solar stations.

## REFERENCES

1    Venkatesan, A., Lowenthal, J., Prem, P. et al. The impact of satellite constellations on space as an ancestral global commons. *Nat Astron*. 2020, Vol.4, pp. 1043 – 1048. doi:10.1038/s41550-020-01238-3

2    Sulistya A.H., Hasbi W., Muhiba R. Design and implementation of effective electrical power system for Surya satellite -1. *IOP Conf. Series: Earth and Environmental Science*. 2018, Vol. 149, pp. 012059. doi:10.1088/1755-1315/149/1/012059

3    Juan J. Rojas, Yamauchi Takashi, Mengu Cho. A lean satellite electrical power system with direct energy transfer and bus voltage regulation based on a bi-directional buck converter. *Aerospace*. 2020, 7(7), pp. 94. doi:10.3390/aerospace7070094

4    Schirone L., Ferrara M., Granello P., Paris C., Pellitteri F. Power Bus Management Techniques for Space Missions in Low Earth Orbit. *Energies*. 2021, Vol. 14, pp. 7932. doi:10.3390/en14237932

5    Salman Salman, Xin AI, Zhouyang WU. Design of a P-&-O algorithm-based MPPT charge controller for a stand-alone 200 W PV system. *Protection and control of modern power systems*. 2018, 3, Article number 25.

6    Mahdi A.S., Mahamad A.K., Saon S., et al. Maximum power point tracking using perturb and observe, fuzzy logic and ANFIS *SN Applied Sciences*. 2020, *2,* Article number: 89.

7    Mishra P.K., Tiwari P. 2021. Incremental conductance MPPT in grid-connected PV system. International Journal of Engineering, *Science, and Technology*, Vol.13, No. 1, pp. 138-145. doi: 10.4314/ijest.v13i1.21S

8    Silva I. F., Toffoli F.L., Vicente P., Vicente E.M. Maximum power point tracking based on the curve sweep method. *Proceeding of the 14th IEEE Intern. Conf. on Industry Applications (INDUSCON)* doi:10.1109/INDUSCON51756.2021.9529667

9    Sevty Satria Bhatara, Reza Fauzi Iskandar, M. Ramdlan Kirom., Design and Simulation of Maximum Power Point Tracking (MPPT) System on Solar Module System Using Constant Voltage (CV) Method. *Proceeding of the AIP Conference*. 2016, 1712, 030012. doi:10.1063/1.4941877

10    Roberto F. Coelho, et al. MPPT Approach Based on Temperature Measurements Applied in PV Systems. *Proceeding of the 9th IEEE/IAS Intern.Conf.on Industry Applications* doi:10.1109/INDUSCON.2010.5740006

11    Syed, Irtaza M.; Yazdani, Amirnaser (2014). Simple mathematical model of photovoltaic module for simulation in Matlab/Simulink. *Proceeding of the 27th Canadian Conference on Electrical and Computer Engineering (CCECE) 2014*, pp. 1–6. doi:10.1109/CCECE.2014.6900977.

12    Boussada Z., Ben Hamed M., Sbita L., Photovoltaic Cell Mathematical Modelling. *International Journal of Engineering Research & Technology (IJERT)*. 2017, Vol. 6, Issue 06, pp. 884-887. doi:10.17577/IJERTV6IS060166

13    Alonso-Alvarez D., Wilson T., Pearce P., et al. Solcore: a multi-scale, Python-based library for modeling solar cells and semiconductor materials. *Journal of Computational Electronics*. 2018, Vol.17, pp. 1099–1123 doi:10.1007/s10825-018-1171-3

14    Xuan Hieu Nguyen, Minh Phuong Nguyen, Mathematical modeling of photovoltaic cell/module/arrays with tags in Matlab/Simulink. *Environ Syst Res*. 2015, Vol. 4, pp. 24. doi: 10.1186/s40068-015-0047-9

15    Kurmanbay A., Baktybekov K., Sakhanov K., Syzdykov A., Mukhamediyev A. Optimization of series-parallel connection of PV array to mitigate negative influence of partial shading conditions. *Proceeding of the 18th Intern. Conf. "Aviation and Cosmonautics". IOP Conf. Series: Materials Science and Engineering 868*. 2020, pp. 012001. doi:10.1088/1757-899X/868/1/012001

16    Veerapen, Sonia, Huiqing Wen. Shadowing effect on the power output of a photovoltaic panel. *Proceeding of the 8th IEEE Intern. Power Electronics and Motion Control Conf. (IPEMC 2016 - ECCE Asia) - Hefei, China. 2016, pp. 3508–3513*. doi:10.1109/IPEMC.2016.7512858

17    Baktybekov K., Kurmanbay A., Sakhanov K., Syzdykov A., Mukhamediyev A. Particle swarm optimization with individually biased particles for reliable and robust maximum power point tracking under partial shading conditions. *Eurasian phys. tech. j.* 2020, Vol.17, No.2(34), pp. 128-137. doi: 10.31489/2020No2/128-137.

18    William F. Holmgren, Clifford W. Hansen, and Mark A. Mikofski. Pvlib python: a python package for modeling solar energy systems. *Journal of Open Source Software*. 2018, 3(29), 884. doi:10.21105/joss.00884

19    Andrews R.W., Stein J.S., Hansen C., and Riley D. Introduction to the open source pvlib for python photovoltaic system modeling package. *Proceeding of the 40th IEEE Photovoltaic Specialist Conference*. 2014, pp. 0170-0174. doi:10.1109/PVSC.2014.6925501

# PROJECT FOR MODIFYING THE SETUP FOR ADRON-55 TO IMPROVE ITS BACKGROUND CHARACTERISTICS AND A REVIEW OF UNSOLVED PROBLEMS IN STUDIES OF EXTENSIVE AIR SHOWERS

Sadykov T.Kh.[1], Chechkin A.V.[2], Iskakov B.A.[1], Makhmet Kh.K.[3]*, Novolodskaya O.A.[1]

[1]Institute of Physics and Technology, Satbayev University, Almaty, Kazakhstan

[2]NRC "Kurchatov Institute", Gatchina, Leningrad region, Russian Federation

[3]Al-Farabi Kazakh National University, Almaty, Kazakhstan, hansh2210@gmail.com

*The article presents an overview of modern problems in studies of Extensive Air Showers and works devoted to their investigation. It is demonstrated that over the past decade convincing evidence of the presence of a neutron component has been demonstrated. When designing experimental facilities aimed at studying the nature of cosmic rays, this must be taken into account, since fast neutrons that arise outside the working volume can adversely affect the interpretation of the obtained data. In particular, if one tries to reveal the nature of penetrating component this effect is at most importance. Studies of biological shielding for the high flux research reactor PIK reactor at the Kurchatov Institute have shown that effective shielding from such neutrons can be provided by polyethylene in combination with borated rubber. At the same time, the use of boron-containing polyethylene does not lead to a significant improvement in protection, however, it significantly increases its cost. Based on foregoing, a modification of the hadron calorimeter protection is proposed to improve its protection it from the influence of the fast neutrons.*

**Keywords:** cosmic rays, extensive air showers, high-energy particles, ionization calorimeter, penetrating component

## Introduction

The study of the nature of cosmic rays has a long history, and it can be said that its origins are already almost one century away from our time. As early as the beginning of the twentieth century, Victor Hess discovered [1] that natural radioactivity on the Earth's surface is only partially due to radioactive decays of elements in the soil and surrounding objects. In the course of his experiments with the rise of ionizing radiation detectors on balloons, he showed that starting from altitudes of more than 1 km, the radiation background began to increase. Moreover, this background did not depend on the time of day and did not decrease even during a solar eclipse, and, as Hess correctly suggested, the source of this ionizing radiation was obviously outside the Earth's atmosphere and was of cosmic origin.

Nowadays, cosmic rays are detected using many different facilities from Cherenkov telescopes such as H.E.S.S., MAGIC, VERITAS, neutrino detectors of the "Kover-2" type of the Baksan Neutrino Observatory, and to detectors of high-energy charged particles, incl. hadrons. Despite the fact that studies of cosmic rays have been going on for more than a century, in this area there are still such unsolved problems as the nature of the appearance of particles with energies exceeding $10^{19 \div 20}$ eV [2], the origin of a break in the energy spectrum [3], and the presence of extensive air showers (EASs) of the penetrating component [5, 6].

To approach the solution of the problems listed above, for example, to clarify the nature of the EASs penetrating component, it is necessary to have data with high fidelity. All known systematic effects should be excluded or minimized, preferably before the analysis. Therefore, section 3 contains the result of the investigation at the Kurchatov Institute concerning the biological shielding at the PIK nuclear reactor. It also proposes modification project for hadron calorimeter in order to reduce the influence of thermal neutrons which can pose some problems to the data analysis if not excluded.

## 1. Review of unsolved problems and attempts of their modern interpretations

There are three problems that are marked as unsolved for today: the maximum energy of cosmic radiation particles, the energy spectral composition (namely, a sharper cutoff at high energies than the theory predicts), and the presence of a penetrating component. Let's start by looking at the first of them.

It would seem, as we know, that there are many places in the Universe where nature acts like a natural laboratory, for example, the magnetic field of magnetars reaches $10^{10 \div 11}$ T [7, 8] and charged particles in such fields can be accelerated to colossal energies. However, since the Universe is isotropically filled with cosmic microwave background at a temperature of ~3 K, then upon reaching a certain energy threshold, charged particles will interact, which will lead to their deceleration and, consequently, to energy loss. This limit was first calculated by G. T. Zatsepin, V. A. Kuzmin [9] and, independently, by Greisen [10]. The characteristic time of interaction of a proton with a kinetic energy of $10^{20}$ eV with cosmic microwave background radiation is estimated at $10^7$ years, which means that when moving at a near-light speed, the maximum distance that these protons would be able to overcome is 100 million light years or about 30 Megaparsecs, but the main problem is that we do not know the direct sources of such rays. Attempts to explain this effect are still ongoing [11,12], including with the use of recent observations showing both anisotropy in the distribution of ultra-high-energy cosmic rays and suggesting that perhaps the highest-energy component may not consist of protons, but of heavy nuclei for which the Greisen-Zatsepin-Kuzmin limit has a different meaning.

The second unsolved problem is the presence of a break in the EAS energy spectrum, which was discovered as early as the middle of the last century [3]. At present, there is no well-established hypothesis [4] that somehow explains its origin, since there are still discrepancies in the results of experiments, for example, in the dissertation [13] by O. B. Shchegolev on pages 13-14, it is shown that for an experiment with a calorimeter KASCADE the so-called "knee" is not observed. And in an article by researchers from the FIAN, it is analytically shown that if a "kink" is observed, then it must have precisely an astrophysical nature [14].

Finally, the presence of the EAS penetrating component also does not have a strong explanation today, and there are suggestions that increased ionization in the deep layers of the calorimeter can be caused both by high cross sections for the production of exotic particles containing heavier generations of quarks, such as charm and strange) [5, 6], and partially explained by the presence of high-energy neutrons in the hadronic component [16], which also made it possible to explain the presence of delayed signals in external detectors.

The point is that if the energy of the primary particle is sufficiently high, and the axis of the EAS (extensive atmospheric showers) passes near the detectors, then a large number of evaporation neutrons are produced, which require some time for thermalization. The penetrating power of fast neutrons through traditional lead shielding is quite high, and they led to additional delayed detector responses.

## 2. Scheme of the Hadron-55 facility and evaluation of the effect of fast neutrons produced in EASs.

The Hadron-55 installation consists of several key components:
1. Two-tier coordinate ionization calorimeter
2. Central shower installation of 30 scintillation detectors
3. Peripheral detectors at distances of 40 and 100 meters from the ionization calorimeter.

The ionization calorimeter is designed to detect charged particles from extensive atmospheric showers and makes it possible to determine the energy of the primary particle. The central shower facility makes it possible to determine the moment of arrival of the EAS front and generates a trigger signal to start recording all subsequent events in the calorimeter. Finally, peripheral detectors also register the EAS arrival moments and, from the time difference, make it possible to reconstruct the zenith angle, and, consequently, the direction of arrival of the primary particle. On Fig. 1 shows the design of an ionization calorimeter. More detailed information about the location of all components of the installation and the principles of operation can be found in the relevant works [16, 17].

It can be seen that a significant part of the calorimeter is occupied by sheets of lead and iron, which usually work well as a shield against ionizing radiation, if we are talking about charged particles or gamma rays. However, it is known that for neutrons, especially for fast neutrons, lead is an extremely poor shield for

two reasons. First, it is known that, in the general case, the cross section for the interaction of neutrons with matter decreases with increasing energy. For example, if we turn to the ENDF (Evaluated Nuclear Data File) database and build graphs for the total cross section for the interaction of fast neutrons with matter, then we will see the following picture presented in Fig. 2: namely, the interaction cross section for neutrons with energies on the order of tens of MeV are at the level of units, with a maximum of tens of barns. At the same time, their kinetic energy is almost millions of times greater than the thermal energy of the substance with which they interact. Though. we can assume that the neutron hits the target at rest.



**Fig.1.** Scheme of the Hadron-55 ionization calorimeter. Image on the left - vertical section of the calorimeter, on the right - location of scintillation detectors and rows of ionization chambers.

It can be seen that a significant part of the calorimeter is occupied by sheets of lead and iron, which usually work well as a shield against ionizing radiation, if we are talking about charged particles or gamma rays. However, it is known that for neutrons, especially for fast neutrons, lead is an extremely poor shield for two reasons. First, it is known that, in the general case, the cross section for the interaction of neutrons with matter decreases with increasing energy. For example, if we turn to the ENDF (Evaluated Nuclear Data File) database and build graphs for the total cross section for the interaction of fast neutrons with matter, then we will see the following picture presented in Fig. 2: namely, the interaction cross section for neutrons with energies on the order of tens of MeV are at the level of units, with a maximum of tens of barns. At the same time, their kinetic energy is almost millions of times greater than the thermal energy of the substance with which they interact. Though, we can assume that the neutron hits the target at rest.

If we neglect change in velocity in the act of one collision of a neutron with an atom, which is performed with good accuracy for heavy atoms such as lead or iron, then if the neutron's the velocity was equal to $v$, and during a unit time of flight it experienced m collisions, then, obviously, the free path $\lambda$ will be is equal to:

$$\lambda = v/m, \tag{1}$$

where $v$ - the neutron's velocity in collision with an atom;

m – number of collision per unit time.

In a unit time interval, a neutron will travel a path $v$ and "sweep" a volume equal to $\sigma v$ in its motion, and multiplying by the concentration of atoms per unit volume $n$, we get the number of collisions per unit time $m$:

$$m = \sigma v n \tag{2}$$

And the mean free path $\lambda$ is then equal to:

$$\lambda = \frac{1}{\sigma n} \tag{3}$$



a)                                                      b)
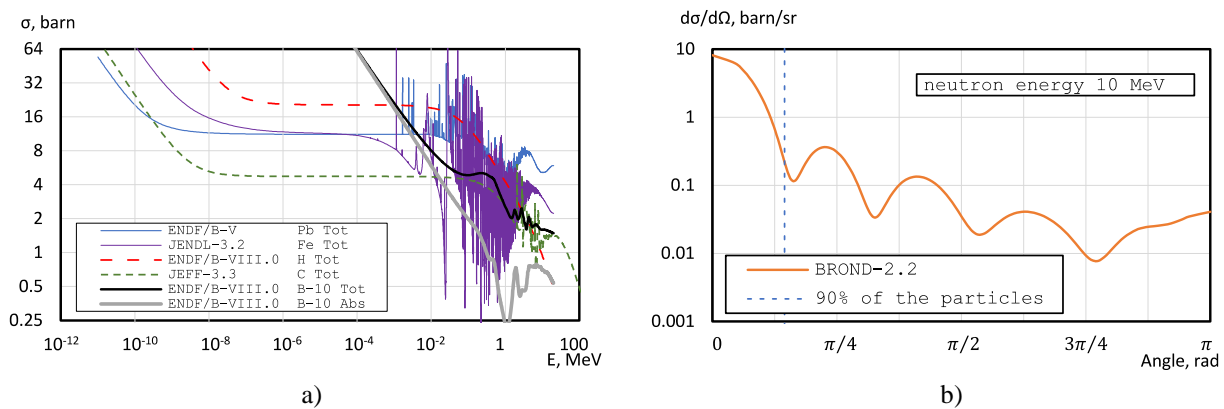
**Fig.2.** a) Dependence of the total interaction cross section for neutrons of different energies; b) differential Cross section for the interaction of neutrons with an energy of 10 MeV in collisions with lead nuclei

The score obtained by order of magnitude in this way is shown in Table 1. It can be seen that the path length of ~10 MeV neutrons in lead is on the order of several centimeters. But it must also be taken into account that this is only the average path length, and most of the neutrons (more than 90%) on average deviate from the initial direction by an angle of less than 26 degrees, which is shown in Fig. 2b.

**Table 1.**

| Substance | $\rho$, g/cm$^3$ | a.m.u | n, $(10^{22})$ | $\sigma$(10MeV) | $\lambda$, cm |
|---|---|---|---|---|---|
| Pb | 11.3 | 207.2 | 3.28 | 5.2 | 6 |
| Fe | 7.8 | 55.45 | 8.52 | 10.3 | 1 |
| $CH_2$ | 1.2 | 14 | 5.14 | 1.01 | 19 |
| $H_2O$ | 1 | 18 | 3.33 | 2.34 | 13 |

The solid curve is the dependence of the differential cross section on the angle. Even on the logarithmic plot, ninety percent of the area under the curve is contained within the 0.26° angle interval. That is, fast neutrons represent a significant difficulty in measurements. However, this is only the first of the problems. The second is that lead works extremely poorly as a neutron moderator. Indeed, in a frontal elastic collision of two bodies with equal mass, according to the law of conservation of momentum, the incident body must stop, and the body at rest must fully acquire its momentum and continue moving.

In the case when the masses of the bodies differ by a factor of 3 or more, and the collisions occur at arbitrary angles, there is an approximation $\xi$ that makes it possible to estimate the logarithm of the ratio of the initial energy $E_0$ to the energy after the collision E [18]:

$$\xi = \ln \frac{E_0}{E} \cong \frac{2}{A+2/3}$$

(4)

That is, for lead (A=207), $\xi \sim 0.01$, which means that about $207/0.01 \sim 20 \cdot 10^3$ collisions are needed before thermalization. Also, using the simplified formula [18] for the thermalization time $\tau_0$ for lead, you can get:

$$\tau_0 = \frac{2\lambda}{\xi v_\tau} \cong 5 \ ms$$

(5)

The situation can also be complicated by the fact that fast neutrons produced outside the calorimeter can be partially but more effectively slowed down by other materials containing lighter nuclides and give an additional excess background, which can complicate the interpretation of obtained data.

### 3. Proposal for modification of the protection of the ionization calorimeter

As described below, the neutron background can present a significant problem in measuring the energy of EAS particles, especially if we are interested in a time interval of ~1 ms. Articles devoted to the study of the EAS neutron component [19] also provide data indicating the existence of events where an anomalously high neutron multiplicity (M>1000) is observed. Thus, if the setup is not aimed at studying EAS by detecting the neutron component, the suppression of the background associated with it is highly desirable.

In 2020, in Nuclear Research Center of Kurchatov Institute research on the effectiveness of biological protection in the PIK high flux reactor hall from the neutron component has conducted, the results of which can be applied in this case as well.

**Table 2**. Comparison of the most effective types of protection against fast and thermal neutrons

| Detector Configuration | | Configuration source | Fast neutrons | Thermal neutrons | Thermal neutrons |
|---|---|---|---|---|---|
| | | | Source without protection | Source in polyethylene (5 cm). | Source in polyethylene (10 cm). |
| 1 | Polyethylene 5 cm. | | 257.3 ± 0.16 (1) | 269.94 ± 0.16 (1) | 183.8 ± 0.2 (1) |
| 2 | Borated polyethylene 5%, 5 cm. | | 19.85 ± 0.09 (12.96) | 18.3 ± 0.08 (14.75) | 11.24 ± 0.03 (16.35) |
| 3 | Borated rubber + Polyethylene (5 cm) | | 255.29 ± 0.16 (1.01) | 244.03 ± 0.16 (1.11) | 162 ± 0.34 (1.13) |
| 4 | Polyethylene (5 cm) + Boron rubber | | 4.61 ± 0.03 protection factor (55.81) | 4.19 ± 0.02 protection factor (64.42) | 2.36 ± 0.03 protection factor (77.88) |
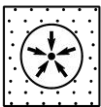
A plutonium-beryllium source with a characteristic neutron energy of ~10 MeV was used as a source of fast neutrons. In order to convert fast neutrons into thermal neutrons, a layer of polyethylene protection with a thickness of 5 and 10 cm was used. A scintillation detector based on a NaI crystal acted as a thermal neutron detector. Various materials have been used as protection, such as polyethylene, boron polyethylene with 5% or 8% boron content, and boron rubber with 20% boron content. The results of the most significant measurements are shown in Tables 2 and 3. The number without brackets means the count rate of the detector per second, and the protection factor is indicated in brackets. With an increase in the thickness of the source protection, the fraction of thermal neutrons increases, therefore, the protection factor against thermal neutrons increases.

To protect yourself from fast neutrons in the experiment, you must first thermalize them, for which polyethylene is used. A layer of 5 - 10 cm of polyethylene works quite effectively. It can be seen that borated rubber itself, despite the large absorption cross section of boron atoms, is unable to provide good protection not only from fast, but also from thermal neutrons.

**Table 3** Evaluation of the effectiveness of borated rubber as a shield against fast neutrons

| Detector Configuration | | Configuration source | Fast neutrons | Thermal neutrons | Thermal neutrons |
|---|---|---|---|---|---|
| | | | Source without protection | Source in polyethylene (5 cm). | Source in polyethylene (10 cm). |
| 1 | Without protection | | $22.15 \pm 0.05$ (1) | $83.52 \pm 0.13$ (1) | $107.7 \pm 0.2$ (1) |
| 2 | Borated rubber | | $1.81 \pm 0.03$ protection factor (12.24) | $3.81 \pm 0.02$ protection factor (21.92) | $2.73 \pm 0.03$ protection factor (39.45) |

However, when it is used together with ordinary polyethylene, it is possible to obtain good suppression of the neutron background. Moreover, the rubber should act precisely as an inner layer, and not an outer one.

## Conclusion

The study of EAS is an intensively developing branch of physics. In the light of new research, it becomes obvious that the hadronic component also includes a neutron component. Thus, data analysis becomes incomplete, so it must be considered when designing experimental setups.

Based on the foregoing, it would be highly desirable to improve the design of the hadron calorimeter by surrounding it with a neutron shield consisting of a layer of borated rubber and polyethylene, at least along the perimeter, so that neutrons produced in the immediate vicinity of the setup would not affect the interpretation of the data obtained. It is also possible to equip the entire complex with additional neutron detectors, whose design is described, for example, in [21].

# REFERENCES

1    Hess F. V. On the Observations of the Penetrating Radiation during Seven Balloon Flights. *History and Philosophy of Physics,* 2018, p. 15.

2    Dedenko L.G., Fedorova G.F., Fedunin E.Yu. The GZK Paradox and Estimation of Energy of the Primary Cosmic Rays. *Proceedings of the 28th Intern. Cosmic Ray Conference*. 2003, pp. 643-646.

3    Kulikov G.V., Khristiansen G.B. On the size distribution of extensive atmospheric showers. *JETP lett.* 1959, Vol. 35 (8), No. 3, pp. 635-640.

4    Stanev T. Cosmic Rays and Etensive Air Showers. *Elastic and Diffractive Scattering. Proceedings, 13th International Conference, Blois Workshop*, CERN, Geneva, Switzerland, 2009, p. 7.

5    Nikolsky S.I., Feinberg E.L., Pavluchenko V.P., Yakovlev V.I. HEW particles in superhigh energy cascades. *Preprint FIAN*, 1975,Vol. 69. [in Russian]

6    Dremin I.M., Yakovlev V.I. Topics on Cosmic Rays. *60th Anniversary of C.M.G. Lattes. Campinas*. 1984,Vol. 1, p. 122.

7    Zhang B.-B., Zhang Z.J., Zou J.-H. A hyper flare of a weeks-old magnetar born from a binary-neutron-star merger. *High Energy Astrophysical Phenomena,* Nanjing 210093, China, 2022, p. 17. doi: 10.48550/arXiv.2205.07670.

8    Pan Y.Y., Li Z.S., Zhang C.M., Zhong J.X.. Study on the magnetic field strength of NGC 300 ULX1 *Monthly Notices of the Royal Astronomical Society.* 2022, Vol.513, Issue 4, pp. 6219-6224.

9    Zatsepin G.T., Kuzmin V.A. About the upper limit of the spectrum of cosmic rays  *Letters to ZhETF*. 1966, Vol. 4, No. 3, pp. 114-117. [in Russian]

10    Greisen K. End to the Cosmic-Ray Spectrum? *Physical Review Letters*. 1966, Vol. 16, No. 17, pp. 748-750.

11    Arahonian F.A., Timokhin A.N.,  Plyasheshnikov A.V. On the origin of highest energy gamma-rays from Mkn 501. *A&A* 2002, Vol. 384, No. 3, pp. 834-847, doi: 10.1051/0004-6361:20020062.

12    Fargion D., De Sanctis Lucentini P.G., Khlopov M.Y. *How can we explain last UHERC anisotropies*? *arXiv:2210.14365*, 2022, 10, 25p. Available at: https://inspirehep.net/literature/2170955

13    Schegolev O.B.  Study of hadronic features of air showers by the method of registration of thermal neutrons. Available at : https://www.inr.ru/rus/referat/disser16.html, (June 2, 2016). [in Russian].

14    Erlykin A.D., Machavariani S.K. About origin of a break in the energy spectrum of cosmic rays. *KSF FIAN*. 2021, No. 2, 27p. [in Russian]. doi:10.1140/epjc/s10052-021-09700-w

15    Stenkin Yu.V., Dzhappuev D.D., Valdes-Galicia J.F. Neutrons in extensive air showers. *Nuclear physics*. 2007, Vol. 70. No. 6., pp. 1123–1135. [in Russian]

16    Sadykov T.Kh., Argynova A.Kh., Argynova K.A. The research of interactions of cosmic radiation particles by the hybrid ionization calorimeter method. *et al. NNC RK Bulletin*. 2019, No. 4.,pp. 28-33. [in Russian]

17    Sadykov T.Kh., Argynova A.Kh., Zhukov V.V. Modernization of peripheral detectors of the Tian-Shan ionization-neutron calorimeter "Adron-55". *Proceedings of NAS RK. Series of physico-mathematical,* Vol. 338, No. 4, 2021, pp. 65-74. [in Russian]

18    Dobrzynski L., Blinowski K. *Neutrons and Solid State Physics*. *London: Ellis Horwood Limited*, 1994, 306p.

19    Serge E. Experimental Nuclear Physics, Vol. II. *New York/London: Willey/Chapman and Hall*, 1953, 600p. Available at: https://www.amazon.co.uk/Experimental-Nuclear-Physics-Segre-Morrison/dp/B000M0XHZ8

20    Stenkin Yu.V., et al. Study of "neutron bursts" with Mexico City neutron monitor. *Astroparticle Physics*. 2001,Vol. 16. No. 2, pp. 157-168.

21    Gromushkin D.M., Bogdanov F.A., Lakhonin A.A. Low-background n-detector for studying the neutron component of EAS. *ECHAYA*. Vol. 49. No. 1, 2018. [in Russian]

**SUMMARIES**                    **ТҮСІНІКТЕМЕЛЕР**                    **АННОТАЦИИ**

*Козловский А.Л.*

**Xe22+ ауыр иондарының әрекеттесу кезіндегі радиациялық зақымданудың жинақталуының цирконий керамикасының жылуфизикалық параметрлерінің өзгеруінеәсерін зерттеу.**

Берілген мақаланың мақсаты нүктелік ақаулар, дислокациялар және бос орындар түріндегі радиациялық зақымданулардың пайда болу процестерінің, сондай-ақ олардың жинақталуының және ZrO$_2$ керамикасының беткі қабатында жергілікті реттелмеген аймақтардың пайда болуының энергиясы 230 МэВ болатын Xe$^{22+}$ ауыр иондарымен сәулелендіру кезінде керамиканың жылуфизикалық қасиеттерінің өзгеруіне әсерін бағалау болып табылады. Сәулелену үшін иондардың түрін таңдау ядролық отындағы ядролық реакциялар процесінде уран ядроларының бөліну фрагменттерінің әсерімен салыстырылатын радиациялық зақымдану процестерін модельдеу мүмкіндіктеріне байланысты. ZrO$_2$ керамика түріндегі сәулелендіруге арналған материалдарды таңдау оларды жаңа буын реакторлары үшін дисперсті ядролық отынның инертті матрицалары үшін негізгі материал ретінде пайдалану перспективаларымен шартталған. Бұл таңдау ZrO$_2$ керамикасының физикалық-химиялық, жылуофизикалық және беріктік қасиеттеріне байланысты, олар оксидті керамиканың басқа түрлерімен салыстырғанда төзімді болып табылады. Зерттеулер барысында сәулеленудің кіші флюенциясы кезінде оқшауланған жергілікті біртексіз аймақтардың пайда болуы зақымдалған керамикалық қабаттың жылуфизикалық қасиеттерінің айтарлықтай өзгеруіне әкелмейтіні анықталды. Алайда, 10$^{12}$ ион/см$^2$-ден жоғары сәулелену флюцияларында болатын t-ZrO$_2$ → c-ZrO$_2$ типті полиморфты түрлендірулер зақымдалған қабатта жылу өткізгіштіктің кемуіне және фонондық жылу алмасу механизмдерінің бұзылуына байланысты жылу жоғалтуларының пайда болуына әкеледі.

**Кілт сөздері:** ZrO$_2$ керамикасы, радиациялық ақаулар, жылуфизикалық қасиеттер, радиациялық зақымдану, ауыр иондар, дисперсті ядролық отын.

*Козловский А.Л.*

**Изучение влияния накопления радиационных повреждений при взаимодействии тяжелых ионов Xe22+ на изменение теплофизических параметров циркониевой керамики.**

Целью данной статьи является оценка влияния процессов формирования радиационно-индуцированных повреждений в виде точечных дефектов, дислокаций и вакансий, а также их накопления и образования локально-разупорядоченных областей в приповерхностном слое ZrO$_2$ керамиках при облучении тяжелыми ионами Xe$^{22+}$ с энергией 230 МэВ на изменение теплофизических свойств керамик. Выбор типа ионов для облучения обусловлен возможностями моделирования процессов радиационных повреждений сравнимых с воздействием осколков деления ядер урана в процессе ядерных реакций в ядерном топливе. Выбор материалов для облучения в виде ZrO$_2$ керамик обусловлен перспективами их применения в качестве основного материала для инертных матриц дисперсного ядерного топлива для реакторов нового поколения. Данный выбор обусловлен физико-химическими, теплофизическими и прочностными свойствами ZrO$_2$ керамик, которые обладают большей устойчивостью, чем другие типы оксидных керамик. В ходе исследований было установлено, что формирование изолированных локально-неоднородных областей при малых флюенсах облучения не приводит к существенным изменениям теплофизических свойств поврежденного слоя керамик. Однако, полиморфные превращения типа t-ZrO$_2$ → c-ZrO$_2$, возникающие при флюенсах облучения выше 10$^{12}$ ион/см$^2$, приводят к снижению теплопроводности и возникновению тепловых потерь, связанных с нарушением механизмов фононной передачи тепла в поврежденном слое.

**Ключевые слова:** ZrO$_2$ керамики, радиационные дефекты, теплофизические свойства, радиационные повреждения, тяжелые ионы, дисперсное ядерное топливо.

*Суржиков А.П., Лысенко Е.Н., Малышев А.В.*

**Радиациялық-термиялық және термиялық жағдайларда сұйық фазалы қақтау әдісімен алынған LiTiZnMn ферриттерінің бастапқы магниттік өтімділігін зерттеу.**

Бастапқы өтімділіктің температуралық тәуелділігін өлшеу литий-титан ферриттеріндегі фазалық және құрылымдық түрленулердің ерекшеліктерін, жылыту және салқындату жылдамдығына, сондай-ақ термиялық және радиациялық термиялық қыздыру кезіндегі сұйық фазалы қақтау температурасына байланысты зерттеу үшін пайдаланылған. Феррит ұнтақ қоспасынан қатты фазалық синтез әдісімен синтезделді. Сұйық фазалы қақтау әдісімен феррит керамикасын алу үшін жеңіл балқитын висмут диоксиді қоспасы қолданылды. КС–қақтау үлгілерді импульстік (1,5-2,0) МэВ электронды шоқпен қыздыру кезінде жүзеге асырылған. Радиациялық–термиялық агломерация үлгілерді импульстік электронды сәулемен (1.5-2.0) МэВ қыздыру арқылы жүзеге асырылды. Қоспа қақталған ферриттердің ақаулы күйіне әкелетіні анықталды, ал сәулеленудің әсері қақтаудың алғашқы кезеңдерінде бұл әсерді күшейтеді. Престелген үлгілердің қыздыру және салқындату

жылдамдығының қақталған ферриттердің бастапқы магниттік өтімділігінің өзгеруіне әсер ету заңдылықтары анықталған.

**Кілт сөздері:** литий ферриттері, сұйық фазалық қақтау, электронды шоқтар, жоғары температуралар, қыздыру және салқындату жылдамдығы, бастапқы магниттік өтімділік.

*Суржиков А.П., Лысенко Е.Н., Малышев А.В.*
**Исследование исходной магнитной проницаемости ферритов LiTiZnMn, полученных методом жидкофазного спекания, в радиационно-термических и термических условиях.**

Измерение температурной зависимости начальной проницаемости было использовано для изучения особенностей фазовых и структурных превращений в литий-титановых ферритах в зависимости от времени, скоростей нагрева и охлаждения, а также температуры жидкофазного спекания при термическом и радиационно-термическом нагреве. Феррит синтезировали из порошковой смеси методом твердофазного синтеза. Для получения ферритовой керамики методом жидкофазного спекания использовалась легкоплавкая добавка диоксид висмута. КС-спекание осуществлялось при нагреве образцов импульсным (1,5–2,0) МэВ электронным пучком. Радиационно-термическое спекание осуществляли путем нагрева образцов импульсным электронным пучком (1.5–2.0) МэВ. Было установлено, что добавка приводит к менее дефектному состоянию спеченных ферритов, в то время как действие излучения усиливает этот эффект на ранних стадиях спекания. Установлены закономерности влияния скоростей нагрева и охлаждения спрессованных образцов на изменение начальной магнитной проницаемости спеченных ферритов.

**Ключевые слова**: литиевые ферриты, жидкофазное спекание, электронные пучки, высокие температуры, скорость нагрева и охлаждения, начальная магнитная проницаемость.

*Аймуханов А.К., Сейсембекова Т.Е., Зейниденов А.К., Ильясов Б.Р., Алексеев А.М., Жаханова А.М.*
**Молибден дисульфиді нанобөлшектерінің органикалық күн ұяшығының мырыш оксидінің электронды тасымалдау қабатының қасиеттеріне әсері.**

Бұл жұмыста молибден дисульфиді нанобөлшектерінің полимерлі күн ұяшығына мырыш оксиді электронды тасымалдау қабатының электронды тасымалына әсерін зерттеу нәтижелері келтірілген. Молибден дисульфиді нанобөлшектері изопропил спиртінде лазерлік абляция әдісімен алынды. Композиттік қабыршақтарды алу үшін нанобөлшектерді мырыш оксиді негізгі құраушысының золь-гель ерітіндісіне әр түрлі концентрацияда қосу арқылы жүзеге асырылған. Сканерлеуші электрондық микроскоп мәліметтері бойынша, қабыршақтағы нанобөлшектердің концентрациясы жоғарылаған сайын мырыш оксиді бетіндегі молибден дисульфиді қабатының қалыңдығы өзгеретіні көрсетілген. Қабыршақ құрылымындағы молибден дисульфиді нанобөлшектері мырыш оксиді қабатының көлемді және беттік бос орындарды біртіндеп толтырады. Алайда, концентрация 1% - дан асқан кезде, қабыршақта тесіктер мен бос орындар пайда болады. Нанобөлшектердің концентрациясы жоғарылаған сайын композиттік қабыршақтың жұтылу спектрлерін өлшеу кезінде қабыршақтың жұтылуы жалпы қалыңдығының өзгеруіне байланысты екенін көруге болады. Бұл жағдайда оптикалық тыйым салынған аймақ енінің мәндері өзгермейді, яғни молибден дисульфиді нанобөлшектері мырыш оксиді электронды құрылымына әсер етпейді. Композитті электронды тасымалдаушы қабаты негізіндегі полимерлі күн ұяшығының вольт-амперлік сипаттамаларынан байқалған өзгерістер молибден дисульфиді нанобөлшектерінің органикалық күн ұяшықтарының электронды тасымалдауға байланысты екені көрсетілді. Органикалық күн ұяшықтарының импеданс спектрлерінің көрсеткіштеріне сәйкес, мырыш оксидіндегі сындық концентрация кезінде молибден дисульфиді нанобөлшектері композитті қабатта заряд тасымалдаушылардың өмір сүру уақытын және диффузия коэффициентін арттыруға ықпал ететіні анықталды.

**Кілт сөздері:** мырыш оксиді, молибден дисульфиді, композициялық қабыршақ, беткі морфология, оптикалық және импеданстық спектроскопия.

*Аймуханов А.К., Сейсембекова Т.Е., Зейниденов А.К., Ильясов Б.Р., Алексеев А.М., Жаханова А.М.*
**Влияние наночастиц дисульфида молибдена на свойства электронно-транспортного слоя оксида цинка органического солнечного элемента.**

В работе представлены результаты исследования влияние наночастиц дисульфид молибдена на электронный транспорт электронный транспортного слоя оксида цинка полимерного солнечного элемента. Наночастицы дисульфид молибдена были получены методом лазерной абляции мишени из дисульфид молибдена в изопропиловом спирте. Для получения композитных пленок наночастицы добавляли в золь–гель раствор предшественника оксида цинка при разных концентрациях. По данным сканирующий атомно-силовой микроскоп было показано, что по мере увеличения концентрации наночастиц в пленке меняется толщина слоя дисульфид молибдена на поверхности оксида цинка. Наночастицы дисульфид молибдена в структуре пленки таким образом постепенно заполняют объемные и поверхностные пустоты в оксиде цинка. Однако при превышении концентрации свыше 1% в пленке образуются дырки и пустоты. По измерениям спектров поглощения композитных пленок было показано, что по мере возрастания концентрации наночастиц в пленке

возрастает поглощение связаное с изменением общей толщины. При этом значения ширины оптической запрещенной зоны не меняется, что означает, что наночастицы дисульфид молибдена не влияет на электронную структуру оксида цинка. Было показано, что наблюдаемые изменения вольт-амперные характеристики полимерного солнечного элемента на основе электронный транспортный слой композитной пленки связано с влиянием наночастиц дисульфид молибдена на электронный транспорт в органических солнечных ячейках. По данным измерения спектров импеданса органической солнечной ячейки было установлено, что наночастицы дисульфид молибдена при критической концентрации в оксиде цинка способствуют увеличению времени жизни носителей заряда и коэффициента диффузии в композитной пленке.

**Ключевые слова:** оксид цинка, дисульфид молибдена, композитная пленка, морфология поверхности, оптическая и импедансная спектроскопия.

*Кубич В.И., Чернета О.Г.*
**Майлаудың динамикалық тұтқырлығы және оның болат материалдарын борлауына әсері.**

Жұмыста шағын өлшемді үлгілердің беттерінің ығысуын физикалық модельдеу және СМЦ-2 үйкеліс машинасының қосымша жабдығын қолдануымен олардың өзара әрекеттесу ортасының динамикалық тұтқырлығын өзгерту кезінде «12Х2Н4(45ХН2МФА) - 45+В болат», «12Х2Н4(45ХН2МФА) - 45+В болат» металл жүйелеріндегі $\tau_0$ адгезиялық байланыстың ығысу беріктігінің және $\beta$ пьезо коэффициентінің өзгеру заңдылықтары алынды. 45 болаттың бетін борлау және бороцементтеу 12х2н4 және 45ХН2МФА болаттарының беттерімен адгезияның белгілі бір қалыпты қысым диапазонында көрінбеуіне әкелетіні анықталды, бұл кезде және сұйық және консистентті майлаудың динамикалық тұтқырлығы кезінде $\tau_0 > 0$. Беттерді майлау кезінде $\tau_0$ параметрі «12х2н4 – болат 45» жүйесі үшін көбірек анықталатыны, ал борлау кезінде болат 45 және динамикалық тұтқырлықтың кіші мәндері $\mu=0{,}027$ Па·с кезінде ішінара анықталады көрсетілген. Сұйық майлау фазасының динамикалық тұтқырлығының жоғарылауымен «12х2н4-болат 45» жүйесінде $\tau_0$ мәнінің жоғарылау тенденциясы көрінеді. Модификацияның болмаған жағдайда 45 бор болат және бор карбиді болат пьезо коэффициентінің сұйық жағармайдың тұтқырлығы мен ығысу жылдамдығынан тәуелсіздігін алдын-ала анықтайды. Борлау және бороцементтеу 45 болат 10,16±0,8 ығысу жылдамдығымен динамикалық тұтқырлықтың 0,027 Па·с-тан 0,19 Па·с-қа дейін өсуімен пьезо коэффициентінің орта есеппен 1,6 есе өсуін алдын-ала анықтайды. Ығысу жылдамдығы =5,08 ±0,6 мм/с болған кезде зерттелетін жүйелерде пьезо коэффициенті салыстырмалы түрде тұрақты болады. Консистентті май материалы арқылы жанасуға ауысқанда, пьезо коэффициентінің өзгеру жылдамдығының көрінуінің бір мәнді емес сипатқа ие болады.

**Кілт сөздері**: пьезо коэффициенті, динамикалық тұтқырлық, майлау материалы, ығысу жылдамдығы, тангенциалды беріктік.

*Кубич В.И., Чернета О.Г.*
**Динамическая вязкость смазки и ее влияние по борированию стальных материалов.**

В работе получены закономерности изменения сдвиговой прочности адгезионной связи $\tau_0$ и пьезокоэффициента $\beta$ в системах металлов «12Х2Н4(45ХН2МФА) - сталь 45+В», «12Х2Н4(45ХН2МФА) - сталь 45+ВС» при физическом моделировании сдвига поверхностей малогабаритных образцов и изменения динамической вязкости среды их взаимодействия с использованием дополнительного оборудования машины трения СМЦ-2. Установлено, что борирование и бороцементация поверхности сталь 45 приводит к отсутствию проявления адгезии с поверхностями сталей 12Х2Н4 и 45ХН2МФА в определенных диапазонах нормальных давлений, при которых $\tau_0 > 0$ и динамической вязкости жидкой и консистентной смазки. Установлено, что параметр $\tau_0$ при смазывании поверхностей в большей мере определяется для системы «12Х2Н4 – сталь 45», и частично при борировании сталь 45 и малых значениях динамической вязкости $\mu=0{,}027$ Па·с. С увеличением динамической вязкости жидкой фазы смазки в системе «12Х2Н4 – сталь 45» просматривается тенденция к увеличению значения $\tau_0$. Установлено, что отсутствие модифицирования сталь 45 бором и карбидом бора предопределяет независимость пьезокоэффициента от вязкости жидкого смазочного материала и скорости сдвига. Борирование и бороцементация сталь 45 предопределяет увеличение пьезокоэффициента в среднем в 1,6 раза с ростом динамической вязкости от 0,027 Па·с до 0,19 Па·с при скорости сдвига 10,16±0,8. При скорости сдвига $\upsilon_1 = 5{,}08$ ±0,6мм/с в исследуемых системах пьезокоэффициент относительно постоянен. С переходом на контакт через консистентный смазочный материал имеет место неоднозначный характер проявления скорости изменения пьезокоэффициента.

**Ключевые слова**: пьезокоэффициент, динамическая вязкость, смазочный материал, скорость сдвига, тангенциальная прочность.

*Байжан Д.Р., Рахадилов Б.К., Алдабергенова Т.М., Баятанова Л.Б., Курбанбеков Ш.Р., Буйткенов Д.Б.*
**Титан бетінде плазмалы-электролиттік тотығу арқылы кальций-фосфат жабындыларын алу.**
ВТ1-0 маркалы титаннан плазмалық электролиттік тотығу (ПЭТ) арқылы субстраттарда кальций-фосфат жабындыларын алу бойынша эксперименттердің нәтижелері ұсынылған. Жабындылар электролитке титан оксиді нанобөлшектерінің әртүрлі мөлшерін қосу арқылы алынды. Кальций-фосфат жабындыларының микроқұрылымы мен трибологиялық қасиеттері зерттелген. Жүргізілген зерттеулер нәтижесінде кальций-фосфат жабындыларын алудың оңтайлы режимдері мен параметрлері анықталды. Электролитке титан оксидінің нанобөлшектерін қосу құрылымға, сондай-ақ алынған жабындылардың беріктігіне әсер етудің мүмкіндігі көрсетілген. Зерттеу нәтижелері титан қорытпаларынан ПЭТ-ны сүйек тінімен біріктіруді жақсарту үшін мұндай өңдеудің болашағы туралы қорытындыға келді.
**Кілт сөздері**: плазмалық-электролиттік тотығу (ПЭТ), нанобөлшектер, жабын, тозу, титан.

*Байжан Д.Р., Рахадилов Б.К., Алдабергенова Т.М., Баятанова Л.Б., Курбанбеков Ш.Р., Буйткенов Д.Б.*
**Получение кальций-фосфатных покрытий на поверхности титана плазменно-электролитическим оксидированием.**
Представлены результаты экспериментов по получению кальций-фосфатных покрытий на подложках из титана марки ВТ1-0 плазменным электролитическим оксидированием (ПЭО). Покрытия были получены с добавлением в электролит разного количества наночастиц оксида титана. Были исследованы микроструктура и трибологические свойства кальций-фосфатных покрытий. В результате проведенных исследований установлены и определены оптимальные режимы и параметры получения кальций-фосфатных покрытий. Показано, что добавление в электролит наночастиц оксида титана может воздействовать на структуру, а также на прочность получаемых покрытий. Результаты исследований привели к выводу о перспективности подобной обработки ПЭО из титановых сплавов, для улучшения их сращивания с костной тканью.
**Ключевые слова:** плазменно-электролитическое оксидирование (ПЭО), наночастицы, покрытие, износ, титан.

*Алкахдери Л.А., Юрченко А.В., Мохаммед Ж.А.-К., Мехтиев А.Д., Нешина Е.Г.*
**Ауа ағынының әртүрлі жылдамдықтарында көмекші жылу көзін пайдалануымен күн кептіргішінің тиімділігін арттыру.**
Ауылшаруашылық өнімдерін сақтаудың маңызды әдістерінің бірі - күн сәулесінде кептіру болып табылады. Берілген мақалада күн кептіру жүйелерінің тиімділігін арттыруға назар аударылған. Күн кептіргіштерінің жұмысына әсер етуі мүмкін жаңа әдістер мен факторларды әзірлеу олардың тиімділігін арттыруға көмектеседі. Бұл зерттеуде ауылшаруашылық өнімдерін кептіруге арналған жанама күн кептіргіш әзірленіп ұсынылған. Күн жалпақ ауа жинағышынан, оқшауланған кептіру камерасынан, қосалқы (электрлік) жылу көзінен және электр желдеткішінен тұратын кептіргіш оның өнімділігін арттыруға арналған. Кептіргіштің ең типтік функциясы -өнімді ыстық ауамен үрлеу, ондағы судың булануына әкеледі. Температура мен ауа жылдамдығының булану жылдамдығына әсері эксперименттік түрде зерттелген. Үш түрлі 0,042, 0,0735 және 0,105 м$^3$/с ауа шығындары кезінде сынақтар жүргізілді. Күн радиациясы аз немесе мүлдем болмаған кезде көмекші жылытқыш жеткілікті жылуды қамтамасыз ету үшін қолданылады. Ауа ағынының әртүрлі жылдамдықтары үшін күн режимі мен электр режимі әр режимде тек бір энергия көзімен эксперименттік түрде тексерілді. Нәтижелер Күн радиациясынан басқа жылу көзін пайдалану кептіру камерасындағы ауа температурасын 32-42 ºС аралығында ұстауға мүмкіндік беретінін көрсетті. Сондай-ақ, бүкіл кептіру процесінде жоғары ауа жылдамдығында температура кептіргіштің жұмысына аз әсер ететіні анықталды.
**Кілт сөздері:** Күн кептіргіш; көмекші жылу көзі, ылғалдың мөлшері, күн ауа коллекторы, ауа ағынының жылдамдығы, мөрлік тақша.

*Алкахдери Л.А., Юрченко А.В., Мохаммед Ж.А.-К., Мехтиев А.Д., Нешина Е.Г.*
**Повышение эффективности солнечной сушилки с использованием вспомогательного источника тепла при различных скоростях воздушного потока.**
Одним из важнейших методов сохранения сельскохозяйственной продукции является сушка на солнце. Основное внимание в этой статье уделяется повышению эффективности солнечных систем сушки. Разработка новых методов и факторов, которые могут повлиять на функциональность солнечных сушилок, помогает повысить их эффективность. В данном исследовании предложена и разработана солнечная сушилка непрямого типа для сушки сельскохозяйственной продукции. Сушилка, состоящая из солнечного плоского воздухосборника, изолированной сушильной камеры, вспомогательного (электрического) источника тепла и электрического вентилятора, предназначена для повышения производительности сушилки. Наиболее типичная функция сушилки — обдувать продукт горячим воздухом, заставляя воду в нем испаряться. Экспериментально изучено влияние температуры и скорости воздуха на скорость испарения. Проведены испытания с тремя различными расходами воздуха — 0,042, 0,0735 и 0,105 м$^3$/с. Когда солнечного излучения мало или совсем нет, для обеспечения достаточного тепла используется вспомогательный обогреватель. Для различных скоростей

воздушного потока солнечный режим и электрический режим были проверены экспериментально только с одним источником энергии в каждом режиме. Выводы показали, что использование другого источника тепла в дополнение к солнечному излучению позволит поддерживать температуру воздуха в сушильной камере в пределах 32-42 ºС. Также было установлено, что в течение всего процесса сушки при высоких скоростях воздуха температура оказывает меньшее влияние на производительность сушилки.

**Ключевые слова:** Солнечная сушилка; вспомогательный источник тепла; содержание влаги; солнечный коллектор воздуха; скорость воздушного потока, печатная плата.

*Сакипова С.Э., Шаймерденова К.М., Нусупбеков Б.Р., Оспанова Д.А., Кутум Б.Б.*
**Құбырлы жылу алмастырғыштағы импульстік соққыдан туындаған жылу және масса алмасу процестерінің динамикасын модельдеу.**
Жұмыста импульстік әсердегі жылу-массаалмасу процестерінің динамикасына сұйық ағынының біртекті емес дәрежесінің әсері кезіндегі эксперименттік зерттеулердің нәтижелері талқыланады. Импульстік әсер ретінде сұйық ортада жоғары вольтты электр разрядтары қолданылды, ол арқылы соққы толқындарының пайда болуымен бірге электргидравликалық әсер жүзеге асырылады. Жоғары гидравликалық қысымда болатын сызықтық емес, тез өзгеретін жылу-массаалмасу процестерінің динамикасын дифференциалдық теңдеулерді қолдану арқылы сипаттау мүмкін емес. Модельдеу аргументтерді топтастырып есептеу әдісі негізінде жүзеге асырылады, оның артықшылығы эксперименттік мәліметтердің аз мөлшерін қолдана отырып, полиномды тәуелділіктерді құру болып табылады. Полиномды тәуелділіктерді құру нәтижелері ағын параметрлерінің импульстік қысым амплитудасының динамикасына және жылу беру қарқындылығына әсерінің синергетикалық эффектісін анықтауға мүмкіндік берді.

**Кілт сөздері:** жылумассаалмасу, құбырлы жылуалмастырғыш, диффузор, аргументтерді топтастырып есептеу әдісі, импульстік әсер, электргидравликалық эффект, жылуберу қарқындылығы.

*Сакипова С.Э., Шаймерденова К.М., Нусупбеков Б.Р., Оспанова Д.А., Кутум Б.Б.*
**Моделирование динамики процессов тепломассобмена в трубчатом теплообменнике при импульсных воздействиях.**
В работе обсуждаются результаты экспериментальных исследований влияния степени неоднородности жидкостного потока на динамику тепло-массообменных процессов при импульсных воздействиях. В качестве импульсных воздействий использовались высоковольтные электрические разряды в жидкостной среде, посредством которых реализуется электрогидравлический эффект, сопровождающийся возникновением ударных волн. Динамику происходящих при этом нелинейных, быстроменяющихся процессов тепломассообмена при высоких гидравлических давлениях, невозможно описать с помощью дифференциальных уравнений. Моделирование проведено на основе метода группового учета аргументов, преимущество которого заключается в построении полиномиальных зависимостей с использованием небольшого количества экспериментальных данных. Результаты построения полиномиальных зависимостей позволили выявить синергетический эффект влияния параметров потока на динамику амплитуды импульсного давления и интенсивность теплоотдачи.

Ключевые слова: тепломассообмен, трубчатый теплообменник, диффузор, метод группового учета аргументов, импульсное воздействие, электрогидравлический эффект, интенсивность теплоотдачи.

*Мирюк О.А., Олейник А.И., Ахмедов К.М.*
**Кеуекті толтырғышпен композициялық материалдың қасиеттерін компьютерлік модельдеу.**
Мақала кеуекті толтырғыштар негізіндегі композициялық материалдардың жылудан қорғайтын және механикалық қасиеттерін болжауға арналған. Гомогенді және гетерогенді құрылымды материалдарының жылу өткізгіштік коэффициенттерін анықтаудың аналитикалық тәуелділіктері келтірілген. Шекті элементтер әдісі негізінде вариатропты құрылымды композициялық материалдарының жылу өткізгіштік коэффициентін сандық анықтау әдістемесі әзірленген. Компьютерлік зерттеулердің нәтижелері аналитикалық модельдерде алынған тәуелділіктермен салыстырылған. Кеуекті толтырғыштар негізіндегі көп қабатты композициялық материалдарды қабықты және пластиналы типті тірек және қоршау конструкцияларында қолданудың орындылығы көрсетілген.

**Кілт сөздері:** композициялық материал, кеуекті толтырғыш, жылу өткізгіштік, шекті элементтер әдісі, көп қабатты қабықша.

*Мирюк О.А., Олейник А.И., Ахмедов К.М.*
**Компьютерное моделирование свойств композиционного материала с пористым заполнителем**.
Статья посвящена прогнозированию теплозащитных и механических свойств композиционных материалов на основе пористых заполнителей. Приведены аналитические зависимости определения коэффициента

теплопроводности материалов гомогенной и гетерогенной структуры. На основе метода конечных элементов разработана методика численного определения коэффициента теплопроводности композиционных материалов вариатропного строения. Результаты компьютерных исследований сопоставлены с зависимостями, полученными на аналитических моделях. Показана целесообразность использования многослойных композиционных материалов на основе пористых заполнителей в несущих и ограждающих конструкциях оболочечного и пластинчатого типов.
**Ключевые слова:** композиционный материал, пористый заполнитель, теплопроводность, метод конечных элементов, многослойная оболочка.

*Сыздыков А.Б., Бақтыбеков Қ.С., Мессерле В.Е., Комаров Ф. Ф., Асқарұлы Р.,  Зилгаринов Д., Мурат А.*
**Төмен орбиталарды пайдаланатын спутниктердегі күн батареяларының фотоэлементтері көлеңкеленген немесе істен шыққан кезде максималды қуат нүктесін табу алгоритмі.**

Күн батареяларын көлеңкелеу немесе бірнеше фотоэлементтердің істен шығуы шығыс ток-кернеу сипаттамасын өзгертеді. Бұл жұмыс ғарыш кемесінің бортында өндірілетін максималды қуатты жақындату және іздеу алгоритмін қарастырады, бұл электр энергиясының қайталама көздерін жылдам зарядтау үшін өте маңызды, өйткені төмен орбиталарда күн жағында болу уақыты шектеулі. Қазіргі уақытта максималды қуат іздеу алгоритмдері тамаша жағдайларда жұмыс істейді, ал күн панельдері көлеңкеленген немесе фотоэлементтер/элементтер істен шыққан жағдайда қарапайым және тиімді алгоритмдер қажет. Бұл жұмыста күн панелін әртүрлі жағдайларда модельдеу жүргізілді. Күн батареясының және күн панелінің шығыс вольт-амперлік сипаттамаларын құру алгоритмі жүзеге асырылды. Сондай-ақ, нақты құрылғыларда әртүрлі алгоритмдерге эксперименттер жүргізілді.
**Кілт сөздері:** максималды қуат нүктесін бақылау, Python, тоқ, кернеу, істен шығу, көлеңкелеу әсері, электрмен жабдықтау жүйесі.

*Сыздыков А.Б., Бақтыбеков К.С., Мессерле В.Е., Комаров Ф. Ф., Асқарұлы Р.,  Зилгаринов Д., Мурат А.*
**Алгоритм поиска точки максимальной мощности при затенении или выходе из строя фотоэлементов солнечных батарей на спутниках, использующих низкие орбиты.**

Затенение солнечных батарей или выход из строя нескольких фотоэлементов изменяет характеристику выходного тока-напряжения. В данной работе рассматривается алгоритм приближения и поиска максимальной мощности, генерируемой на борту космического аппарата, что очень важно для быстрой зарядки вторичных источников электрической энергии, поскольку время пребывания на солнечной стороне на низких орбитах ограничено по времени. В настоящее время алгоритмы поиска максимальной мощности работают в идеальных случаях, а в случаях затенения солнечных панелей или выхода из строя фотоэлементов/элементов необходимы простые и эффективные алгоритмы. В данной работе проведено моделирование солнечной панели в различных условиях. Реализован алгоритм построения выходных вольт-амперных характеристик солнечного элемента и солнечной панели. Также были проведены эксперименты различных алгоритмов на реальных устройствах.
**Ключевые слова:** Отслеживание точки максимальной мощности, Python, ток, напряжение, отказ, эффект затенения, система электроснабжения.

*Садыков Т.Х., Чечкин А.В., Искаков Б.А., Махмет Х. Қ., Новолодская О.А.*
**Кең атмосферлік нөсерлерді зерттеуде шешілмеген мәселелерге шолу және «АДРОН-55»  үшін қондырғыны оның фондық сипаттамаларын жақсарту үшін модификациялау жобасы.**

Мақалада кең атмосферлік нөсерлердің зерттеу саласындағы заманауи мәселелерге шолу және оларды зерттеуге арналған жұмыстар келтірілген. Соңғы онжылдықта нейтрондық құраушысының бар екендігі туралы сенімді дәлелдер алынғаны және бұл құраушы ғарыштық сәулелердің табиғатын зерттеуге бағытталған тәжірибелік қондырғыларды жобалау кезінде ескерілуі керек екендігі көрсетілді. Сондай-ақ адрондық калориметрдің қорғанысын оның жұмыс көлемінен тыс пайда болатын жылдам нейтрондардың әсерінен қорғау үшін өзгерту ұсынылады, бұл алынған мәліметтерді түсіндіруге теріс әсер етеді. Атап айтқанда, егер енетін құраушының табиғатын ашуға тырысатын болсақ, онда бұл әсер ең маңызды болып саналады. Курчатов институтындағы ПИК жоғары ағынды ғылыми-зерттеу реакторының биологиялық қорғанысын зерттеу полиэтиленнің боры бар каучукпен бірге мұндай нейтрондардан тиімді қорғанысты қамтамасыз ете алатынын көрсетті. Сонымен қатар боры бар полиэтиленді пайдалану қорғанысты айтарлықтай жақсартуға әкелмейді, бірақ оның құнын айтарлықтай арттырады. Жоғарыда айтылғандарға сүйене отырып, адрондық калориметрді жылдам нейтрондардың әсерінен қорғауды арттыру үшін қорғаныстың модификациясы ұсынылады.
**Кілт сөздері:** ғарыштық сәулелер, кең атмосферлік нөсерлер, аса жоғары энергиялы бөлшектер, иондану калориметрі, енетін құкраушы.

*Садыков Т.Х., Чечкин А.В., Искаков Б.А., Махмет Х.К., Новолодская О.А.*

**Проект модификации установки для «АДРОН-55» для улучшения ее фоновых характеристик и обзор нерешённых задач при исследовании широких атмосферных ливней.**

В статье представлен обзор современных проблем в области изучения Широких Атмосферных Ливней и работ, посвящённых их исследованию. Демонстрируется, что за последнее десятилетие были получены убедительные свидетельства наличия нейтронной компоненты и что учёт этой компоненты необходим при проектировании экспериментальных установок, направленных на изучение природы космических лучей. Также предлагается вариант модификации защиты адронного калориметра чтобы защитить его от влияния быстрых нейтронов, возникающих вне его рабочего объёма, что может негативно влиять на интерпретацию получаемых данных. В частности, если попытаться выявить природу проникающей составляющей, то этот эффект имеет наибольшее значение. Исследования биологической защиты высоко поточного исследовательского реактора ПИК в Курчатовском институте показали, что эффективную защиту от таких нейтронов может обеспечить полиэтилен вместе с борсодержащим каучуком. В то же время использование борсодержащего полиэтилена не приводит к существенному улучшению защиты, однако значительно удорожает его стоимость. На основании изложенного предлагается модификация защиты адронного калориметра для повышения его защиты от воздействия быстрых нейтронов.

**Ключевые слова**: космические лучи, широкие атмосферные ливни, частицы сверхвысоких энергий, ионизационный калориметр, проникающая компонента

| INFORMATION ABOUT AUTHORS | АВТОРЛАР ТУРАЛЫ МӘЛІМЕТТЕР | СВЕДЕНИЯ ОБ АВТОРАХ |

**Aimukhanov, A.К.** – PhD, Associate Professor, Professor, Department of Radiophysics and Electronics, Leading Researcher of the Scientific Center for Nanotechnology and Functional Nanomaterials, E.A. Buketov Karaganda University, Karaganda, Kazakhstan; Scopus Author ID: 35321945000; ORCID ID: 0000-0002-4384-5164, a_k_aitbek@mail.ru

**Akhmedov, K.M.** - Candidate of techn. sciences, Senior Lecturer, Higher School of Economics and Construction, Rudny Industrial Institute, Rudny, Kostanay region, Kazakhstan; ORCID iD: 0000-0002-0565-4412; kamandar1960@mail.ru

**Aldabergenova, T.M.** – PhD, Senior Researcher of the Research center "Modification of the surface of materials", Shakarim University, Semey, Kazakhstan; Scopus Author ID: 6506076753, tamaraalga@mail.ru

**Alkahdery, L.A.R.** – Master (Eng.), Lecturer, Electromechanical Engineering Department, National Research Tomsk Polytechnic University, Tomsk, Russia, ORCID ID: 0000-0003-2785-0761, 50226@uotechnology.edu.iq

**Askaruly, R.** – Student, L.N. Gumilev Eurasian National University; Junior Researcher of the JSC "National Company "Kazakhstan Garysh Sapary", Astana, Kazakhstan; ORCID ID: 0000-0002-9202-6528; rustam_king.01@mail.ru

**Baizhan, D.R.** – Master, Senior Researcher of the Research center "Surface Engineering and Tribology", Sarsen Amanzholov East Kazakhstan University, Ust-Kamenogorsk, Kazakhstan, Scopus Author ID: 57214891142, daryn.baizhan@mail.ru

**Baktybekov, K.S.** – Doctor of phys.-math. science, Professor, Leading engineer-designer of space technology; Gulyam LLP; Astana, Kazakhstan; Scopus Author ID: 8926833000; k.baktybekov@ghalam.kz

**Bayatanova, L.B.** – PhD, Senior Researcher, "PlasmaScience" LLP, Ust-Kamenogorsk, Kazakhstan, Scopus ID 55540404900, leila_1809@mail.ru

**Buitkenov, D.B.** - PhD, Senior Researcher of the "Surface Engineering and Tribology" Research center, Sarsen Amanzholov East Kazakhstan university, Ust-Kamenogorsk, Kazakhstan, Scopus Author ID: 57214891142, buitkenovd@mail.ru

**Chechkin, A.V.** - Candidate of phys.-math. sciences, Senior Researcher, NRC "Kurchatov Institute", Gatchina, Leningrad region, Russian Federation; Scopus Author ID: 57196656438; ORCID ID: 0000-0003-2796-9471; a.4ech89@gmail.com

**Cherneta, O.G.** - Candidate of Technical Sciences, Associate Professor of the Department "Cars and Automotive Industry", Dniprovsk State Technical University, Kamenskoe, Ukraine, Scopus Author ID: 57203871112, ocherneta@gmail.com

**Ilyassov, B.R.** - PhD, Associate Professor, Astana IT University, Astana, Kazakhstan, Scopus Author ID: 56669724700, WoS Researcher ID: C-1411-2015, ORCID ID: 0000-0003-4563-2004.

**Iskakov, B.A.** - Master (Sci.), Junior Research Fellow, Institute of Physics and Technology, Almaty, Kazakhstan; Scopus Author ID: 57211885734; Researcher ID: AAS-2585-2020; ORCID ID: 0000-0002-0025-8381; leodel@mail.ru

**Komarov, F.F.** - Doctor of phys.-math. science, Professor, Head of the Laboratory of Elionics of the Institute of Applied Physical Problems of BSU, Belarusian State University, Minsk, Belarus; Scopus Author ID: 35425974200

**Kozlovskiy, A.L.** - PhD, Associate Professor, Head of the Laboratory of Solid State Physics, Astana branch of the Institute of Nuclear Physics of the Ministry of Energy of the Republic of Kazakhstan, Astana, Kazakhstan

**Kubich, V.I.** - Candidate of Technical Sciences, Associate Professor of the Department "Cars", National University "Zaporozhye Polytechnic", Zaporozhye, Ukraine, Scopus Author ID: 57203875007, schmirung@gmal.com

**Kurbanbekov, Sh.R.** - PhD, Associate Professor, Department of Physics; Khoja Ahmed Yasawi International Kazakh-Turkish University, Kazakhstan, Scopus Author ID: 55540216100, sherzod.kurbanbekov@ayu.edu.kz

**Kutum, B.B.** – Master (Phys.), Senior Lecturer, E.A. Buketov Karaganda University, Karaganda, Kazakhstan; Scopus Author ID: 57213520178; kuttykadam@mail.ru

**Lysenko, E.N.** - Doctor of techn. sciences, Professor, Head of the Research Laboratory, National Research Tomsk Polytechnic University, Tomsk, Russia, Scopus Author ID: 25027787100, lysenkoen@tpu.ru

**Makhmet, Kh.K.** – Master (Eng.), Engineer, Institute of Physics and Technology, Almaty, Kazakhstan; ORCID ID: 0000-0001-8700-7640; hansh2210@gmail.com

**Malyshev, A.V.** – Candidate of phys.-math. sciences, Senior Researcher, National Research Tomsk Polytechnic University, Tomsk, Scopus Author ID: 57200723126, malyshev@tpu.ru

**Mekhtiyev, A.D.** - Candidate of Technical Sciences, Professor, Department of Electrical Equipment Operation, S.Seifullin Kazakh Agrotechnical University, Astana, Kazakhstan, Scopus Author ID: 5729935782, ORCID ID: 0000-0002-2633-3976, barton.kz@mail.ru

**Messerle, V.E.** - Doctor of techn. sciences, Professor, Department of Thermophysics and Technical Physics; Al-Farabi Kazakh National University, Almaty, Kazakhstan; Scopus Author ID: 6602472315

**Miryuk, O.A.** – Doctor of techn. sciences, Professor, Head of Educational Programs, Higher School of Economics and Construction, Rudny Industrial Institute, Rudny, Kostanay region, Kazakhstan; ORCID iD: 0000-0001-6892-2763; psm58@mail.ru

**Mohammed, J.A.-K.** – PhD, Professor, Electromechanical Engineering Department, University of Technology, Baghdad, Iraq, Scopus Author ID: 57191737360; ORCID ID: 0000-0003-1456-6673, 50128@uotechnology.edu.iq

**Murat, A. -** Master, Engineer, JSC "National Company "Kazakhstan Garysh Sapary", Astana, Kazakhstan

**Neshina, Ye.G.** - Candidate of techn. sciences, Head of Department "Energy Systems", A. Saginov Karaganda Technical University, Karaganda, Kazakhstan, Scopus Author ID: 57191724446, ORCID ID: 0000-0002-8973-2958, 1_neg@mail.ru

**Novolodskaya, O.A.** - Candidate of phys.-math. sciences, Senior Researcher, Institute of Physics and Technology, Almaty, Kazakhstan; Scopus Author ID: 6504679234; ORCID iD: 0000-0002-1978-2781; novololga@yandex.ru

**Nussupbekov, B.R.** – Candidate of techn. sciences, Professor, E.A. Buketov Karaganda University, Karaganda, Kazakhstan; Scopus Author ID: 56289675900; ORCID ID: 0000-0003-2907-3900; bek_nr1963@mail.ru

**Oleinik, A.I. -** Doctor of techn. sciences, Associate Professor, Higher School of Economics and Construction, Rudny Industrial Institute, Rudny, Kostanay region, Kazakhstan, ORCID iD: 0000-0002-8252-1357; aoleinik@mail.ru

**Ospanova, D.A.** – PhD student, E.A. Buketov Karaganda University, Karaganda, Kazakhstan; Scopus Author ID: 56286193500; bota_didar@mail.ru

**Rakhadilov, B.K.** – PhD, Associate Professor, "PlasmaScience" LLP, Ust-Kamenogorsk, Kazakhstan, Scopus Author ID: 55539741700, rakhadilovb@mail.ru

**Sadykov, T.Kh. -** Doctor of phys.-math. sciences, Professor, Head of the Laboratory of Cosmic Ray Physics; Institute of Physics and Technology, Almaty, Kazakhstan; Scopus Author ID: 6701423748; ORCID ID: 0000-0002-4349-4616; ResearcherID: D-5899-2019, turlan43@mail.ru

**Sakipova, S.E. -** Candidate of phys.-math. sciences, Professor, E.A. Buketov Karaganda University, Karaganda, Kazakhstan; Scopus Author ID: 6504154211; ORCID ID: 0000-0002-7505-8413

**Seisembekova, T. -** 3rd year PhD student, Researcher of the Scientific Center for Nanotechnology and Functional Nanomaterials, E.A. Buketov Karaganda University, Karaganda, Kazakhstan; ORCID ID-0000-0002-1497-0759, tosh_0809@mail.ru

**Shaimerdenova, K.M. -** Candidate of techn. sciences, Professor, Head of Department of Engineering Thermophysics named after professor Zh.S. Akylbayev, E.A. Buketov Karaganda University, Karaganda, Kazakhstan; Scopus Author ID: 56604144400; gulzhan.0106@mail.ru

**Surzhikov, A.P. -** Doctor of phys.-math. sciences, Professor, Head of Department of Control and Diagnostics, National Research Tomsk Polytechnic University, Tomsk, Russia, Scopus Author ID:6603494148, surzhikov@tpu.ru

**Syzdykov, A.B.** – Master, Senior Lecturer, Project Office Engineer; JSC "National Company "Kazakhstan Garysh Sapary"; Astana, Kazakhstan; Scopus Author ID: 57205435715; arman1978@bk.ru

**Yurchenko, A.V.** - Doctor of techn. sciences, Professor, Tomsk State University, Tomsk, Russia; Scopus Author ID: 55308619600, niipp@inbox.ru

**Zeinidenov, A.K.** – PhD, Associate professor, Dean of the Physical-Technical Faculty, Leading Researcher of the Scientific Center for Nanotechnology and Functional Nanomaterials, E.A. Buketov Karaganda University, Karaganda, Kazakhstan; Scopus Author ID: 56386144000, ORCID ID: 0000-0001-9780-5072, asyl-zeinidenov@mail.ru

**Zhakhanova, A.M**. – Master, Junior Researcher, Scientific Center for Nanotechnology and Functional Nanomaterials, E.A. Buketov Karaganda University, Karaganda, Kazakhstan; ORCID ID - 0000-0002-3863-2682.

**Zilgarinov, D.** - Student, L.N. Gumilev Eurasian National University; Junior Researcher of the JSC "National Company "Kazakhstan Garysh Sapary", Astana, Kazakhstan; ORCID ID: 0009-0000-9025-5522;

**Alexeev, A.M.** - Candidate of phys.-math. sciences,  Kazan Federal University, Kazan, Russia, WoS Researcher ID: A-8526-2012, ORCID ID:0000-0002-2800-6047.

# GUIDELINES FOR AUTHORS

*Eurasian Physical Technical Journal* (Eurasian phys. tech. j.) is a peer-reviewed open access international scientific journal publishing original research results on actual problems of technical physics and other related fields. Since 2004 «Eurasian phys. tech. j.» is published in English.

*Acceptance of the manuscript* for publication in the Eurasian phys. tech. j. is carried out online through website - https://phtj.buketov.edu.kz/index.php/EPTJ. Authors should check that their submissions meet all of the following requirements, as submissions may be returned to authors that do not comply with these guidelines.

### *Scientific article topic and content*

A scientific article should contain the results of original scientific research previously unpublished and not intended for publication in other publications.

Manuscript of the article should contain at least 75% of the original text.

All articles are published **in English in 4 scientific areas of physics: Energy, Engineering, Materials Science, Physics and Astronomy.**

### *Publication Ethics and Malpractice Statement*

Submission of an article to the Eurasian phys. tech. j. implies that the paper described has not been published previously, that it is not under consideration for publication elsewhere, that its publication is approved by all authors and tacitly or explicitly by the responsible authorities where the paper was carried out, and that, if accepted, it will not be published elsewhere in the same form, in English or in any other language, including electronically without the written consent of the copyright holder.  In particular, translations into English of papers already published in another language are not accepted.

For information on Ethics in publishing and Ethical guidelines for journal publication see http://www.elsevier.com/publishingethics and http://www.elsevier.com/journal-authors/ethics.

The Eurasian phys.tech.j. strictly adheres the Code of Conduct of the Committee on Publication Ethics (COPE), and follows the COPE Flowcharts for Resolving Cases of Suspected Misconduct (http://publicationethics.org/files/u2/New_Code.pdf).

To verify originality, your article may be checked by the originality detection service Cross Check http://www.elsevier.com/editors/plagdetect.

### *Pre-publication process*

**Authors** are responsible for the content of their publications. No other forms of scientific misconduct are allowed, such as plagiarism, falsification, fraudu-lent data, incorrect interpretation of other works, incorrect citations, etc. Authors are obliged to participate in peer review process and be ready to provide corrections, clarifications, retractions and apologies when needed. All authors of a paper should have significantly contributed to the research.

**Reviewers** should provide objective judgments and should point out relevant published works which are not yet cited. Reviewed articles should be treated confidentially. The reviewers will be chosen in such a way that there is no conflict of interests with respect to the research, the authors and/or the research funders.

**Editors** have complete responsibility and authority to reject or accept a paper, and they will only accept a paper when reasonably certain. They will preserve anonymity of reviewers and promote publication of corrections, clarifications, retractions and apologies when needed.

The acceptance of a paper automatically implies the copyright transfer to the Eurasian phys. tech. j.

All submitted papers will the sent for reviewing to leading experts in the given area.

The Editorial Board of the Eurasian phys. tech. j. will monitor and safeguard publishing ethics.

The editors reserve the right to accept or reject manuscripts.

The article and all documentation must be identified by the name of the 1st author: Akhmetov AA_et al_paper; Akhmetov AA_et al_fig.1; Akhmetov AA_et al_Cover letter; …

The article text must be formatted according to the **Template**, font - Times New Roman, size -11 pt; line spacing-single; alignment-in width, see https://phtj.buketov.edu.kz/index.php/EPTJ/about/submissions#authorGuidelines

### *An article should consist:*

**Title**: includes a separate line on the left the **UDC** index, Title of the article, information about the authors-surname and initials, name of institution, city, country, e-mail of a corresponding author.  The author**\*** who submitted an article for publication will be considered as a corresponding author.

**Abstract** should consist of at least 5-6 sentences, not exceeding 200-250 words without formula, references, abbreviations. An abstract is a short and powerful summary that describes the focus and subject of a research paper. It could contain the information about why the research study was done, background, what the methodology was and something about the findings of the author(s).

**Keywords**: at least 3-10 basic terms or short phrases used in the article.

**The text should be divided on structural parts:** Introduction, Main part (Theoretical part, Methods and materials or Experimental technique), Results and Discussion, Conclusions.

**Conclusions**: formulating main results; a comparison of the results with the existing data on this topic; assessment of scientific novelty and practical value of the results.

**Acknowledgments or Funding** may be shown at the end of the article text, before References.

**References**: a bibliographic list is compiled according to the requirements:

- Books, abstracts, patents: Surname and initials of the authors (it is enough to indicate the first three or one surnames, et al), *Title of the book* in italics, publish house or city, year and total number of pages.

- Journals, collections of papers, conference proceedings - Surname and initials of the authors (the first three are enough), the title of the article, the *Title of the journal* in italics (you can use the abbreviated title), city and / or country, year, volume, issue number, pages of the "begining and end" (pp. … - … .).

- Internet links also must to indicated the authors, the title and URL

The authors should represent References according to the requirements of international journals on physics, but should to consult preliminarily for standard abbrevi¬ations of journal's names. More information on references guidelines for journal publication you can see in Harvard reference system - http://www.emeraldgrouppublishing.com/authors/guides/write/harvard.htm?part=2/

All references must be numbered in the text (for example, [1], [2-4]) and listed in numerical order.

**All abbreviations and acronyms**, with the exception of obviously well-known, should be deciphered at first use in the text.

**Equations** in your paper have to be written using the Microsoft Equation Editor or the MathType.

**Tables**, numbered and titled, should be inserted into the text (Times New Roman, size - 10 pt) or have been presented as an appendix at the end of the article.

**Figures** should be prepared in a digital form suitable for direct reproduction. Figures shall be submitted on the separate sheets or can be included into the text.

**The manuscript volume**, including text, formulas, figures, bibliography, should not exceed 12 pages including tables, figures (no more than 8-10) and references (no more than 30-35) of text typed on a computer using Microsoft Word editor. The review article should not exceed 20 pages with no more than 15 figures.

### *List of required documents*

***The following files must be uploaded to the journal's website***:

1. Text of the article, with pictures (*.doc);

2. Figure, Picture, Photo (fig1.jpg, fig2.pcx, …);

3. Figure captions (*.doc);

4. A Cover letter - from a university, research institute or an organization licensed to conduct research activities, must be issued on an official letterhead and / or certified by the organization seal. The management officially confirms by this letter that the article (the title of the article and the names of the authors are indicated in English) doesn't contain any information constituting state or commercial secrets, and the article can be published in the Open Press. Authors must upload a copy of the signed Cover Letter in PdF format to the Journal website.

*It's necessary to upload by separately 2 files in English (and in Russian for authors from Russia, and in Kazakh for authors from Kazakhstan):*

5. Article's data: Surname and initials of the authors, the article title, abstract, keywords.

6. Information about each co-author: full name, academic degree, academic title, place of work or study, title of organization, city, country, SCOPUS Author ID or ORCID iD; and contact details (e-mail, phone).

7. Receipt of payment. Authors should pay for the publication only after receiving notification about a positive decision of the reviewers.